8-2011

A priori Analysis of Subgrid-Scale Heat Flux Vectors in High Pressure H2/O2 Mixing and Reacting Shear Layers

Ayse Korucu
Clemson University, akorucu@clemson.edu

A priori Analysis of Subgrid-Scale Heat Flux Vectors in High Pressure H_2/O_2 Mixing and Reacting Shear Layers

---

A Masters Thesis
Presented to
the Graduate School of
Clemson University

In Partial Fulfillment
of the Requirements for the Degree
Master of Science
Mechanical Engineering

---

by
Ayse Korucu
August 2011

Accepted by:
Dr. Richard S. Miller, Committee Chair
Dr. Donald E. Beasley
Dr. Richard S. Figliola

Abstract

A Direct Numerical Simulation (DNS) database of supercritical, transitional H_2/O_2 mixing and reacting shear layers is analyzed in an *a priori* manner to obtain subgrid statistics relevant to Large Eddy Simulation (LES) engineering modeling. The DNS employs a real gas state equation, detailed chemistry, accurate property models, multicomponent, differential, and cross diffusion. The parallel simulations were conducted using eighth order central finite differencing in conjunction with a fourth order accurate Runge-Kutta time integration, on resolutions up to 135 million grid points, and used up to 2,016 processing cores. All simulations are for an ambient pressure of 100 atm and are relevant to rocket engine conditions. The particular focus of the study is on analyzing the subgrid heat flux vector which has thus far been nearly universally ignored in the literature. DNS provides a near "exact" description of all of the scales of the flow. For this study the DNS database is filtered over a range of filter widths to provide the exact LES governing equations; including those terms requiring modeling. The filtered heat flux vector is extensively compared with the heat flux vector calculated as a function of the filtered primitive variables (ie. the exact LES term is compared with its form available within an actual LES). The difference between these forms defines the subgrid heat flux vector. The subgrid heat flux vector is found to be insignificant for pure mixing cases, however, even for mixing cases the divergence of the subgrid heat flux vector is of the same order as

other subgrid terms in the LES energy equation. Both the subgrid heat flux vector and its divergence are found to be substantially larger in reacting flows due to the associated large temperature gradients. The analysis is done both globally across the entire flame, as well as by conditionally averaging over specific regions of the flame; including regions of large subgrid kinetic energy, subgrid scalar dissipation, subgrid temperature variance, flame temperature, etc. These results highlight specific regions of the flame where modeling errors may occur in an actual LES if the subgrid heat flux vector is neglected. The dynamic/similarity modeling approach is therefore derived and tested for use in modeling the subgrid heat flux vector. An analysis of the model performance indicates that although the model improves the prediction of the filtered heat flux vector in both mixing and reacting flows, it nevertheless requires improvement. In particular, the model performance deteriorates with increasing filter width, and retains substantial errors when the divergence of the heat flux vector is considered. However, the model shows improved results for the higher Reynolds number simulation.

Acknowledgments

First, I would like to express my gratitude towards Dr. Miller, who has helped and directed me to earn the Master's degree in the past two years. Without his endless patience and psychological assistance, I would not have finished.

I also thank Justin Foster and Zhiyuan Ma, who shared their knowledge with me on my research.

I would like to thank Dr. Beasley and Dr. Figliola for both being in my committee and giving such valuable suggestions.

Also, my special thanks go to the Turkish Government for being my financial supporter.

Finally, I would like to dedicate my thesis to my parents, Kadir and Zeliha Korucu, and brothers, Aydin, Mehmet and Metin Korucu, who have believed in me and supported me so that I could get My master's degree abroad.

Table of Contents

List of Tables

List of Figures

Chapter 1

Introduction

Accurately estimating turbulent flow properties is the ultimate goal for advanced engineering associated with reactive flows [13, 8, 44]. In the past, engineers had to rely on experiments [13]. However, by improving computational and numerical models, Computational Fluid Dynamics (CFD) codes can now predict turbulent flow properties, such as temperature, velocity, [13, 8, 44, 26, 17] etc. with reasonable levels of accuracy for relatively simple flows. There are three primary tecniques for calculating turbulent flows: Direct Numerical Simulation (DNS), Reynolds-Averaged Navier-Stokes (RANS), and Large-Eddy Simulation (LES) [13, 44, 26, 35, 29, 31, 49].

DNS seeks to solve the governing equations "exactly". The errors involved occur due to the numerical schemes used to the solve Navier-Stokes equations [31]. It aims to resolve every scale in the flow with the provided boundary and initial conditions [36]. DNS may have the ability to solve all the scales of a flow, but only if the mesh spacing is at most the same size as the smallest scale of the flow (i.e. the Kolmogorov scale). High order numerical schemes are typically employed to control numerical errors [31, 36]. Despite its capacity of giving remarkably good results, DNS has some disadvantages which limits its capabilities [31, 36]. DNS can only be

conducted at low, or moderate Reynolds numbers (unlike RANS, or LES), and it is not typically suitable for complex geometries [31, 36]. Additionally, it tends to require a massive amount of computational work which makes it costly [31, 36].

RANS is the most well-known, and commercially available method for turbulent flow modeling. The Navier-Stokes equations are typically decomposed into a time averaged mean $< f >$ and fluctuation $f^{'}$ [31]. Time averaging produces unclosed terms, which contain the effects of the fluctuations on the mean flow field [31]. In order to solve the closure problem many distinct RANS models have been developed under various levels of assumption [13].

RANS has many limitations; particularly for reacting flows. This has drawn the attention of researchers to LES [34, 39] for obtaining more accurate predictions of flow properties [34]. LES as a CFD method holds a place between RANS and DNS [31, 36, 4]. In LES, the large scale eddies, which contain most of the turbulence energy, are calculated directly by the "filtered" LES governing equations, and the effects of only the small scales are modeled [44, 31, 4, 47, 22, 25, 9, 33, 3]. The filtering operator is defined as: $\Phi = \overline{\Phi} + \Phi'$. Since, in contrast to the large scales, the small scales are less effected by the boundary conditions, their models may have a simpler form [22].

In turbulent flows energy is transferred from large scales to small scales (i.e. the energy cascade). However, the energy cascade is an average flow of kinetic energy from large scale to small scale. Locally the cascade may be in either direction [7]. As Piomelli *et. al* [30] pointed out, energy transfer can be either larger or smaller than the average value, and also can be from small scales to the large scales locally in the flow (i.e. back scatter) [7, 30, 51, 9, 46]. Most of the models that have been proposed in the literature only consider dissipative flow of energy from large to small scales [32]. However, subgrid modeling should include both direct (i.e. forward scatter)

and reverse (i.e. back scatter) energy transfer in order to make accurate turbulence predictions [2].

Various LES models can be found in the literature and most of them are based on "eddy-viscosity" models [46, 36], which relate the subgrid scale stresses, τ_{ij}, to the large scale (i.e. filtered) strain rate tensor, $\overline{S_{ij}} = \frac{1}{2}(\frac{\partial \overline{u_i}}{\partial x_j} + \frac{\partial \overline{u_j}}{\partial x_i})$, where the overbar denotes the filtering operator (see below) [31]. The most common model is the Smagorinsky model, which basically employs the eddy-viscosity concept with the assumption of equilibrium of the small scales [9, 31, 36, 7]. Although eddy-viscosity models are widely used in turbulence modeling, they have some primary weaknesses which can be listed as follows: 1) the flow dependent model coefficient (i.e. the Smagorinsky constant) is assumed to be a positive constant (no back scatter), and 2) the model is very poorly correlated with the actual subgrid stress [51].

In response to this, Germano *et. al* [9] developed a new approach to obtaining the model constant called the dynamic subgrid scale eddy-viscosity model (DSM). It is based on the Smagorinsky model but overcomes some of the aforementioned limitations [51]. The dynamic model is based on an algebraic identity between the subgrid scale stresses at two varied filter widths and the large scale turbulent stresses [9, 51]. In this way, the DSM dynamically calculates the model "constant" based on local information and therefore inherently considers the energy transmission between resolved and unresolved scales (i.e. back scatter) [9, 51]. However, since the DSM coefficient fluctuates extremely over the computational domain, it is often averaged over a homogeneous flow direction [52] or adhocly "clipped".

In another primary LES modeling approach, Bardina *et. al* [1], introduced a non-eddy-viscosity model called the scale similarity model (SSM). This approach assumes that the smallest resolved scales are statistically similar to the largest unresolved scales [31, 51, 46, 36]. The SSM requires double-filtering to capture the energy

interaction between the largest unresolved scales and the smallest resolved scales. Under this assumption the energy spectrum has three bands: 1) the largest resolved scales, 2) the test filter region (i.e. the smallest resolved scales) and 3) the unresolved scales (subgrid scales) [38]. A new model for the subgrid heat flux vector is developed in this thesis and is based on a dynamic version of the SSM.

For incompressible flows, the SSM subgrid stress is modeled as follows:

$$\tau_{ij} = C_{sim}(\overline{\overline{u}_i\overline{u}_j} - \bar{\bar{u}}_i\bar{\bar{u}}_j), \tag{1.1}$$

where u_i is the velocity vector, τ_{ij} is the subgrid stress tensor, the overbar represents the filtering operation, and the constant C_{sim} is typically taken to be unity. Note that all terms on the right hand side of Eq. (1.1) can be calculated within an actual LES. Even though the modeled subgrid-scale stress is well correlated with the actual stress, Eq. (1.1) is insufficiently diffusive to be used numerically [18, 23] . Therefore a "mixed" model was proposed by Bardina *et. al* [1] which simply superimposes the Smagorinsky and the scale similarity models [18, 23]. The mixed model is expressed as follows:

$$\tau_{ij}^{\Delta,mix} = C_{sim}(\overline{\bar{u}_i\bar{u}_j} - \bar{\bar{u}}_i\bar{\bar{u}}_j) - 2(c_s^{\Delta}\Delta)^2|\,\bar{S}\,|\,\bar{S_{ij}}, \tag{1.2}$$

where the first two terms represent the SSM and the last term is the Smagorinsky model [23, 31] with model constant C_s^{Δ}.

Zang *et. al* [51] later developed another model, the dynamic mixed model (DMM), which basically mixes Germano' s dynamic procedure and the mixed model for incompressible flows. This retains the viscous qualities of the mixed model but also retains the potential for back scatter (i.e. regions of $C_s^{\Delta} < 0$) [51]. The new

model was built on the mixed model proposed by Bardina *et. al* [1]:

$$\tau_{ij} - \frac{\delta_{ij}}{3}\tau_{kk} = -2C\overline{\Delta}^2|\overline{S}|\overline{S}_{ij} + L^m_{ij} - \frac{\delta_{ij}}{3}L^m_{kk}, \tag{1.3}$$

where L^m_{ij} is the combination of the Leonard stress, $L_{ij} = \overline{\overline{u}_i\overline{u}_j} - \overline{u}_i\overline{u}_j$, which is obtained from decomposition of the SGS stress, and the Bardina scale similarity term, $\beta = \overline{u}_i\overline{u}_j - \overline{\overline{u}}_i\overline{\overline{u}}_j$, where $\overline{\Delta} = (\Delta x_1 + \Delta x_2 + \Delta x_3)^{1/3}$ defines the grid spacing, and C is the dynamic model coefficient [51]. They reported that the modified DMM produced better results than the DSM, and unphysical fluctuations of the DSM coefficient were reduced notably [51].

Martin *et. al* [22] used the SSM to model the subgrid-scale (SGS) turbulent diffusion, viscous dissipation and viscous diffusion of a compressible turbulent flow and found that the adopted method was superior to the eddy-viscosity and eddy-diffusivity methods. For compresible flows a density weighted Favre filter is introduced in order to reduce the number of unclosed terms. The Favre filter is defined as $\langle\langle f\rangle\rangle = \overline{\rho f} \;/\; \overline{\rho}$. They concluded that the FDSM provided results which better matched the experimental data [52].

Liu *et. al* [19] used the dynamic subgrid scale model based on the eddy viscosity model as proposed by Yoshizawa [50]. The model includes the turbulent stress and heat flux models for stratified shear flow [19, 50]. They concluded that the model is effective for LES of stratified turbulent channel flows [19]. Vreman *et. al* [46] proposed subgrid-scale models for other terms that are usually neglected in the momentum and energy equation: 1) a SSM for the pressure dilatation, 2) SSM and **k**-dependent models (subgrid kinetic energy) for the turbulent dissipation rate, and 3) a DMM for the pressure-velocity subgrid terms. LES calculations for flows at low Mach number show that most of the subgrid terms in the energy equation are negligible. However,

the modeled turbulent dissipation rate was found to be significant in the filtered energy equation [46]. The study [46] concluded that the SSM was able to obtain satisfying results proportional to the standard dynamic model. Furthermore, the DMM was found to provide more reasonable results than either the SSM or the DSM were able to [46].

Willamson *et. al* [48] tested the DMM and dynamic reconstruction methods to identify if the model was eligible to be used to model transport of a passive scalar in an incompressible turbulent flow. Both methods enhanced not only the prediction the mean flow but also the turbulence statistics [48]. Jaberi *et. al* [15] adopted the dynamic/similarity method to model the filtered reaction rate of turbulent non-premixed flames, and showed the model was capable of predicting the local SGS values. Francois *et. al* [45] developed a scale dependent dynamic/similarity method for modeling the subgrid scale reactant covariance. They showed that the new developed model provided better results than its scale-invariant counterpart [45].

Although there are many unclosed terms in the filtered LES equations, the current work will focus on the subgrid heat flux vector that is almost universally neglected in the literature. Typically, the heat flux vector is considered in its Fourier form. For single species with constant properties, the filtered form of the Fourier heat flux vector is expressed as:

$$\overline{Q_j} = -\kappa \overline{\frac{\partial T}{\partial x_j}} = -\kappa \frac{\partial \bar{T}}{\partial x_j} \tag{1.4}$$

where κ is the constant thermal conductivity, T is temperature and $\bar{T}$ is the standard filtered temperature. For constant density flows $\overline{T}$ is a primitive variable in LES and Q_j can be calculated "exactly" without additional closure. However, for compressible flows, $\langle\langle T \rangle\rangle$ is the primitive variable that is produced in LES using the Favre filter.

Even in this case a subgrid heat flux vector is present (and may be significant) since $-\kappa\partial\overline{T}/\partial x_j \neq -\kappa\partial\langle\langle T\rangle\rangle/\partial x_j$. Therefore, $\kappa = \kappa(\Psi)$ is further considered:

$$\overline{Q_j} = \ -\kappa\overline{\frac{\partial T}{\partial x_j}} = -\kappa(\overline{\Psi})\frac{\partial\langle\langle T\rangle\rangle}{\partial x_j} + \ Q_{sgs,j}, \tag{1.5}$$

where Ψ is the set of LES primitive variables. Therefore, $Q_{sgs,j}$ exits even for single species compressible flows although it is nearly universally neglected without comment nor analysis. Furthermore, for turbulent reacting mixture flows with real properties, and real gas equations of state (EOS), under generalized diffusion including Dufour diffusion, the subgrid heat flux vector can be expected to be significantly more complex.

1.1 Objectives

Based on the above, the primary objectives of the following thesis are to: 1) test the hypothesis that the subgrid heat flux vector may require modeling in LES of realistic, variable density, multicomponent, turbulent flames, and 2) to test the hypothesis that the dynamic scale similarity procedure may be suitable for modeling the subgrid heat flux vector if it is found to be significant for LES.

This thesis begins with presenting the governing equations, chemical kinetics and numerical approach used to create a previously generated DNS database of high pressure mixing and reacting H_2/O_2 shear layers in Chapter 2. This database is then used as an example canonical flame for an a *priori* analysis of the subgrid heat flux vector and its potential significance in Chapter 3. Chapter 3 also develops and tests a new potential model for the subgrid heat flux vector based on the dynamic scale similarity approach. Conclusions are provided in Chapter 4.

Chapter 2

Formulation and Numerical Approach

2.1 Governing Equations

The following work provides a post processing analysis of a previously generated DNS database of high pressure H_2/O_2 mixing and reacting shear layers [4, 6]. The DNS governing equations employ a real gas state equation, real property models, multicomponent diffusion, and detailed chemistry. The current work only gives the summarized forms of the governing equations. For a more detailed formulation author typically refers to the following see: Palle [27], Palle and Miller [28], Vasudevan [42] and Foster [4]. The compressible form of the Navier-Stokes, energy, and species transport equations are:

$$\frac{\partial \rho}{\partial t} + \frac{\partial}{\partial x_j}[\rho u_j] = 0, \tag{2.1}$$

$$\frac{\partial}{\partial t}(\rho u_i) + \frac{\partial}{\partial x_j}[\rho u_i u_j + P\delta_{ij} - \tau_{ij}] = 0, \tag{2.2}$$

$$\frac{\partial}{\partial t}(\rho e_t) + \frac{\partial}{\partial x_j}[(\rho e_t + P)u_j - u_i\tau_{ij} + Q_j + \sum_{\alpha=1}^{N} H'_\alpha J'_{j,\alpha}] = S_e, \tag{2.3}$$

$$\frac{\partial}{\partial t}(\rho Y_\alpha) + \frac{\partial}{\partial x_j}[\rho Y_\alpha u_j + J'_{j,\alpha}] = S_{Y_\alpha}, \tag{2.4}$$

$$P = \frac{RT}{V' - B_m} - \frac{A_m}{V'^2 + 2V'B_m - B_m^2}, \tag{2.5}$$

where t is time, x_j is the spatial coordinate vector, ρ is the mixture density, u_j is the mixture velocity, P is the pressure, δ_{ij} is the Kronocker delta tensor, τ_{ij} is the (Newtonian) viscous stress tensor, e_t the total specific energy (internal plus kinetic), Q_j is the Bearman-Kirkwood form of the heat flux vector, $\sum_{\alpha=1}^{N} H'_\alpha J'_{j,\alpha}$ is the enthalpy flux (N is the total number of species) in which the partial molar enthalpy for species α is $H'_\alpha = \partial H'/\partial X_\alpha$ (X_α is the mole fraction of species α), and the molar mass flux vector for species α is $J_{j,\alpha}$. The relation $J'_{j,\alpha} = M_\alpha J'_{j,\alpha}$ (M_α stands for the molecular weight of species α) converts the molar flux vector to the mass flux vector, and S_e is the chemical reaction source term for the energy equation ($S_e = -\sum_{\alpha=1}^{N} \dot{\omega}_\alpha \, \Delta H^0_\alpha$), where $\dot{\omega}_\alpha$ is the reaction rate for species α and ΔH^0_α is the enthalpy of formation). For Eq. (2.4), Y_α represents the mass fraction of species α, and $S_{Y,\alpha}$ is the chemical reaction source term for species α. Finally, for the Peng Robinson state equation [Eq. (2.5)]. V ' is the molar volume, T is temperature, R is the universal gas constant, and A_m and B_m are appropriately defined mixture parameters.

The effects of multicomponent, differential, and cross diffusion effects have been included into the equations employed for the DNS calculations. Under high

pressures, these effects have the ability to be significant [27, 12, 11, 24, 5]. Harstad and Bellan derived the full form of the heat and mass flux vectors taking into account the aforementioned effects by using non-equilibrium thermodynamics and fluctuation theory (as kinetic theory is not applicable for high pressure dense fluids). The heat flux vector may be represented as a superposition of terms proportional to temperature, pressure, and mole fraction gradients:

$$Q_j = Q_j^T + Q_j^{X_1} + Q_j^{X_2} + ... + Q_j^{X_{\alpha=N-1}} + Q_j^P, \tag{2.6}$$

The superscripts indicate the variable gradient upon which the term is proportional to. The expanded form adopted in the DNS is:

$$\begin{aligned} Q_j = &- \left\{ \kappa + \sum_{k=1}^{N-1} \sum_{l>k}^{N} X_k X_l \alpha_{BK}^{kl} \alpha_{BK}^{kl} \frac{R\rho}{M_m} D_m^{kl} \right\} \frac{\partial T}{\partial x_j} \\ &- \sum_{k=1}^{N} \left\{ X_k \sum_{l \neq k}^{N} [\frac{M_l}{M_m^2} X_l \alpha_{BK}^{kl} \rho D_m^{kl}] V_{,k} \right\} \frac{\partial P}{\partial x_j} \\ &- \sum_{o=1}^{N-1} \sum_{k=1}^{N} \left\{ RT \sum_{l \neq k}^{N} [\frac{M_l}{M_m^2} X_l \alpha_{BK}^{kl} \rho D_m^{kl}] \alpha_D^{ko} \right\} \frac{\partial X_o}{\partial x_j}, \end{aligned} \tag{2.7}$$

where $M_m = \sum_{\alpha=1}^{N} X_\alpha M_\alpha$ is the mixture molecular weight. In the above, D_m^{kl} represents the binary mass diffusion factors, κ is the mixture thermal conductivity, and the thermal and mass diffusion factors are represented by α_{BK}^{kl} and α_D^{ko}, respectively. The first term represents the expanded Fourier component. The remaining terms are referred to as Dufour diffusion and represent heat flux due to both mole fraction and pressure gradients. Conversely, the mass flux vector (not shown) contains Fickian diffusion proportional to mole fraction gradients, and Soret diffusion proportional to both temperature and pressure gradients. The corresppponding form of the mass flux

vector including Soret diffusion is:

$$J'_{j,k} = -nD_m^{kl} \sum_{l \neq k}^{N} \left\{ X_k X_l \frac{M_l}{M_m} \alpha_{BK}^{kl} \right\} \frac{\partial lnT}{\partial x_j} \tag{2.8}$$
$$- \sum_{l \neq k}^{N} \frac{nD_m^{kl}}{R'T} \left\{ -\frac{M_k M_l}{M_m M_m} X_k X_l V'_{,l} + \frac{M_k M_k}{M_m M_m} X_k X_l V'_{,k} \right\} \frac{\partial P}{\partial x_j}$$
$$- \sum_{o=k}^{N-1} \left\{ \sum_{l \neq k}^{N} [\frac{M_k M_l}{M_m M_m} X_k n D_m^{kl} \alpha_D^{lo} + \frac{M_l M_L}{M_m M_m} X_l n D_m^{lk} \alpha_D^{ko}] \right\} \frac{\partial X_o}{\partial x_j},$$

Almost universally, when cross-diffusion is significant it is related to Soret diffusion with the Dufour effect being considered negligible [12, 11, 24, 5]. However, it is mathematically inconsistent to neglect the Dufour terms while retaining the Soret terms as violations of the second law are possible [10]. In addition, the non-linear nature of the Dufour terms may affect the resulting subgrid heat flux vector defined as $Q_{sgs,j} = \overline{Q_j(\Psi)} - Q_j(\overline{\Psi})$ (see below).

The DNS further employs realistic property models for all κ, D_m^{kl}, ν , C_p α_{BK}^{kl} and α_D^{kl} [4, 27, 42, 37]. The thermal conductivity, κ, is calculated by the Stiel Thodos method. The Fuller method is employed to calculate the low pressure binary diffusion coefficient [27, 37]. The Takahashi correlation is employed to calculate the high pressure departures [27, 37]. The Lucas method is adopted to calculate the mixture viscosity [27, 37]. The high pressure heat capacity is calculated from the Peng-Robinson EOS equation [27] low pressure values are provided by Reid *et. al* [37], or the NIST webbook. Lastly, the model developed by Vasudevan [42] and Vasudevan *et. al* [43] is employed for the thermal diffusion coefficients. Detailed information and explanation of all property models can be found in Refs. [4, 27, 42, 37].

2.2 Chemical Kinetics and Numerical Approach

The detailed chemistry which is the basis of the DNS calculation [4] includes a pressure dependent 19-step and 8-species (H_2, O_2, H_2O, OH, H, O, HO_2 and H_2O_2) mechanism developed by Sohn *et. al* [41]. The details of the mechanism are provided in Table 2.1. The high pressure H_2/O_2 flame is chosen as an example flame both due to the availability of a pre-existing DNS database, as well as for its application to rocket engines.

The DNS data used in this work is obtained from the code developed by Palle [27]. In the beginning, the DNS flame code was designed as 1D simulation [27], and it was extended to 3D analysis by Foster [4]. The DNS data used in this work was calculated by solving the governing equations for $3D$, temporally developing, non-premixed, mixing and reacting shear layers of O_2/H_2. Details of the computational domain, mesh and numerical scheme used can be found in Ref. [4]. Figure 2.1 depicts the computational domain with counter-flowing streams of fuel, H_2, and oxidizer, O_2. The mixing occurs at the center of the domain. The initial vorticity thickness, δ_0, is defined as the initial transition length from one free stream to the other. The "flame Reynolds number" is defined by $Re_F = U_0\delta_0\rho_0/\mu_0$; where U_0 is the velocity difference between the two streams, ρ_0 is the averaged density, and μ_0 is the averaged viscosity from each stream value. For the current work, two distinct reacting simulations are considered for Re_F numbers 850 and 2500. An additional purely mixing simulation is also considered at $Re = 2000$. For all cases the initial temperature is $T_0 = 700K$, and the initial pressure is $P_0 = 100atm$ throughout the domain. The convective Mach number is set to be 0.35.

Equally spaced grid points from $0 \leq x_1 \leq L_1$ and $0 \leq x_3 \leq L_3$ in x_1 and x_3 directions are used for the computational mesh. In the x_2 direction an analytical

No.	**Reaction**	**A [cm.mole.s]**	β	E_α **[kJ/mole]**
1.	$O_2 + H \rightleftharpoons OH + O$	2.00×10^{14}	0.00	70.30
1.	$O_2 + H \rightleftharpoons OH + O$	2.00×10^{14}	0.00	70.30
2.	$H_2 + O \rightleftharpoons OH + H$	5.06×10^{14}	2.67	26.30
3.	$H_2 + OH \rightleftharpoons H_2O + H$	1.00×10^{8}	1.60	13.80
4.	$OH + OH \rightleftharpoons H_2O + O$	1.50×10^{9}	1.14	0.42
5.	$H + H + M \rightleftharpoons H_2 + M$	1.80×10^{18}	-1.00	0.00
6.	$H + OH = M \rightleftharpoons H_2O + M$	2.20×10^{22}	-2.00	0.00
7.	$O + O + M \rightleftharpoons O_2 + M$	2.90×10^{17}	-1.00	0.00
8.	$H + O_2 + M \rightleftharpoons HO_2 + M$	2.30×10^{18}	-0.80	0.00
	k_α	4.52×10^{13}	0.00	0.00
9.	$HO_2 + H \rightleftharpoons OH + OH$	1.50×10^{14}	0.00	4.20
10.	$HO_2 + H \rightleftharpoons H_2 + O_2$	2.50×10^{13}	0.00	2.90
11.	$HO_2 + H \rightleftharpoons H_2O + O$	3.00×10^{13}	0.00	7.20
12.	$HO_2 + O \rightleftharpoons OH + O_2$	1.80×10^{13}	0.00	-1.70
13.	$HO_2 + OH \rightleftharpoons H_2O + O_2$	6.00×10^{13}	0.00	0.00
14.	$HO_2 + HO_2 \rightleftharpoons H_2O_2 + O_2$	2.50×10^{11}	0.00	-5.20
15.	$OH + OH + M \rightleftharpoons H_2O_2 + M$	3.25×10^{22}	-2.00	0.00
	k_α	7.45×10^{13}	-0.37	0.00
16.	$H_2O_2 + H \rightleftharpoons H_2 + HO_2$	1.70×10^{12}	0.00	15.70
17.	$H_2O_2 + H \rightleftharpoons H_2O + OH$	1.00×10^{13}	0.00	15.00
18.	$H_2O_2 + O \rightleftharpoons OH + HO_2$	2.80×10^{13}	0.00	26.80
19.	$H_2O_2 + OH \rightleftharpoons H_2O + HO_2$	5.40×10^{12}	0.00	4.20

Table 2.1: Detailed chemical kinetic mechanism for H_2/O_2 combustion [41] and corresponding forward reaction constants: $k_r = AT^\beta exp(-E_A/\overline{R}T)$. Third body efficiencies: $H_2 = 1.00$, $O_2 = 0.35$, $H_2O = 6.5$. Reaction rate coefficients dependent on pressure are calculated as $k_r = k_\infty k_0[M]/(k_\infty + k_0[M])$ where k_0, and k_∞ are the low and high pressure reaction rate coefficients, respectively.

mapping function proposed in [14] is employed to stretch the mesh in the cross-stream direction. In the vorticity thickness region a fine grid spacing ($\Delta x_2 \approx \Delta x_1$) is used, while the spacing stretches towards each of the free stream boundaries where $\Delta x_2 \approx 5\Delta x_1$ [4]. Assigning a coarser mesh in the free stream regions reduces the computational time significantly. Detail of the mapping the can be found in [4].

An eight order central explicit finite difference method and a forth order Runge-Kutta are employed to solve for the spatial and time derivatives, respectively. At each Runge-Kutta stage tenth order filtering is also applied to control spurious oscillations. The message passing interface (MPI) routines are used to parallize the code in all three directions. Further information about the numerical algorithms can be found in Ref. [16].

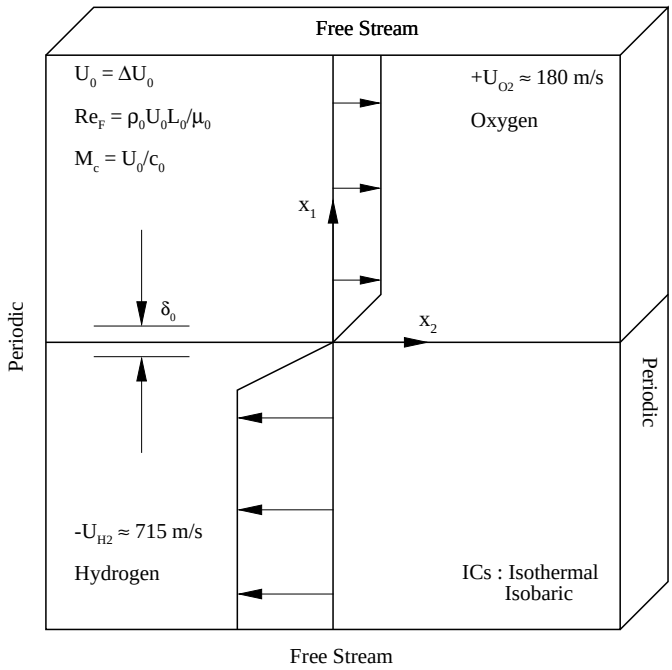

Figure 2.1: Computational domain for the reacting temporal mixing layer.

The database consists of three distinct simulations; two reacting ($Re_F =$

850, 2500) and one non-reacting ($Re = 2000$). The simulations were conducted on the Palmetto Cluster at Clemson University with resolutions up to 560 x 720 x 336 $\approx$ 135 million grid points and using as many as $2,016$ processing cores. Detailed information can be found in Table 2.2.

	Non-Reacting	Reacting	
	$Re = 2000$	$Re_F = 850$	$Re_F = 2500$
$Species1$	O_2	O_2	O_2
$Species2$	H_2	H_2	H_2
$T_0(K)$	700	700	700
$P_0(atm)$	100	100	100
M_c	0.35	0.35	0.35
$N_1 \times N_2 \times N_3$	3.42×10^7	3.42×10^7	1.35×10^8
N_1	384	384	560
N_2	384	384	720
N_3	232	232	336

Table 2.2: Simulation values for the DNS calculations.

Chapter 3

Results

This chapter presents the unique and novel work of the present thesis. First, the subgrid heat flux vector and its relative importance are *a priori* analyzed from the DNS database in Section 3.1. Then, upon determining that the subgrid heat flux is significant for reacting flows a dynamic scale similarity model is derived and tested in Section 3.2.

3.1 Subgrid Analysis

The idea of LES is to directly calculate only the large eddies while modeling the effects of the small scales. To be able to categorize the large and small scale eddies a filtering procedure is applied to the Navier-Stokes equations. The filtering procedure basically separates eddies into two parts, resolved eddies (which carry most of the turbulence energy) and unresolved eddies (whose effects need to be modeled). The LES equations include a filtered component which involves instantaneous, resolved variables (Φ), plus a subgrid fluctuating component, $\Phi = \overline{\Phi} + \Phi'$. A general filtered

variable, $\overline{\Phi}$, is defined by the convolution integral:

$$\overline{\Phi}(x) = \int_{\Omega} G(x_j - x'_j)\Phi(x'_j)dx'_j, \tag{3.1}$$

where $G(x_j)$ is the filter kernel defined over the domain Ω. The current work uses a spherical top-hat filter with diameters $\Delta/\Delta x_1 = 0$, 6, 10, 16, 20, and 25. Here, Δ is the filtering sphere diameter. As compressible flow is considered for this work, employing the Favre filtering concept is necessary. The Favre filter is a density-weighted filtering operation, and is equivalent to a standard filter for constant density flows. Favre filtering can be related to the standard filtering by the following expression, $\langle\langle\Phi\rangle\rangle = (\ \overline{\rho\Phi}\ ) \ / \ \overline{\rho}\ (\langle\langle . \rangle\rangle$ indicates the Favre filtering.). Decomposition of a Favre filtered instantaneous variable includes the Favre filtered component plus a fluctuating component, $\Phi = \langle\langle\Phi\rangle\rangle + \Phi''$.

The exact (unclosed) filtered LES governing equations can be expressed as follows:

$$\frac{\partial\ \overline{\rho}}{\partial t} + \frac{\partial}{\partial x_j}[\ \overline{\rho}\ \langle\langle u_j\rangle\rangle] = 0, \tag{3.2}$$

$$\frac{\partial}{\partial t}(\overline{\rho}\ \langle\langle u_i\rangle\rangle) + \frac{\partial}{\partial x_j}[\ \overline{\rho}\ \langle\langle u_i u_j\rangle\rangle + \overline{P}\delta_{ij} - \overline{\tau_{ij}}\ ] = 0, \tag{3.3}$$

$$\frac{\partial}{\partial t}\ (\overline{\rho}\ \langle\langle e_t\rangle\rangle) + \frac{\partial}{\partial x_j}\left[(\overline{\rho}\ \langle\langle e_t\rangle\rangle + \overline{Pu_j}\ - \overline{u_i\tau_{ij}} + \overline{Q_j} + \overline{\sum_{\alpha=1}^{N} H'_\alpha J'_{j,\alpha}}\ \right] = \overline{S_e}, \tag{3.4}$$

$$\frac{\partial}{\partial t}(\ \overline{\rho}\ \langle\langle Y_\alpha \rangle\rangle) + \frac{\partial}{\partial x_j}[\ \overline{\rho}\ \langle\langle Y_\alpha u_j \rangle\rangle + \langle\langle J'_{j,\alpha} \rangle\rangle] = \overline{S_{Y_\alpha}}. \tag{3.5}$$

$$\overline{P} = \overline{\frac{RT}{V' - B_m} - \frac{A_m}{V'^2 + 2V'B_m - B_m^2}}, \tag{3.6}$$

The set of LES primitive variables is $\overline{\Psi} = \overline{\rho}$, $\langle\langle u_j \rangle\rangle$, $\langle\langle e_t \rangle\rangle$, $\langle\langle Y_\alpha \rangle\rangle$. Any term which cannot be directly obtained from this set of variables is unclosed and therefore requires modeling. For example, the non-linear convective term in Eq. 3.3 is typically decomposed as:

$$\langle\langle u_i u_j \rangle\rangle = \langle\langle u_i \rangle\rangle \langle\langle u_j \rangle\rangle + \tau_{sgs,ij} \tag{3.7}$$

where $\tau_{sgs,ij} = [\langle\langle u_i u_j \rangle\rangle - \langle\langle u_i \rangle\rangle \langle\langle u_j \rangle\rangle]$ and is referred to as the subgrid stress tensor.

As DNS contains all the information about any instantaneous variable, the "exact" subgrid information may be accessed by filtering the DNS data. This is referred to the *a priori* approach to LES analysis (in contrast to the *a posteriori* approach in which an actual LES is performed).

Even though many unclosed terms exist in the LES filtered equations, this work focuses on the heat flux vector, Eq. (2.7). A detailed analysis and modeling for a canonical high pressure H_2/O_2 reacting shear layer is performed. The magnitude of the exact filtered heat flux, $|\overline{Q_j(\Psi)}|$, is compared with the magnitude of heat flux vector calculated using only filtered primitive variables, $|Q_j(\overline{\Psi})|$. Here, Ψ represents the set of primitive variables used in the DNS, $\Psi = [\rho, u_j, e_t, Y_\alpha]$. Other variables such as temperature and pressure are obtained from this base set; eg. $T(\Psi)$ and $P(\Psi)$. Similarly, Eq. (2.7) provides the heat flux vector, $Q_j(\Psi)$. For LES, variables other than the set $\overline{\Psi}$ can only be approximated as functions of $\overline{\Psi}$; eg. $T(\overline{\Psi})$, $P(\overline{\Psi})$,

and $Q_j(\overline{\Psi})$. Therefore, terms calculated in such a manner are not necessarily either equal to, nor even approximately equal to, the terms in the exact LES equations. For example, $\overline{P(\Psi)}$ appears in the exact LES momentum equation. However, only $P(\overline{\Psi})$ can be calculated. The difference, therefore, defines an unclosed "subgrid", or "subgrid scale" (SGS) pressure; $\overline{P(\Psi)} = P(\overline{\Psi}) + P_{sgs}$. Subgird terms such as this may, or may not, require modeling depending in part on their magnitude with respect to both the resolved term [eg. $P(\overline{\Psi})$] as well as with respect to other terms in the LES equations.

The subject of the current work is in testing whether or not the subgrid heat flux vector defined by $Q_{sgs,j} = \overline{Q_j(\Psi)} - Q_j(\overline{\Psi})$ is significant for reacting flows. *A priori* testing using the DNS data is chosen as all forms of the heat flux and subgrid heat flux vectors can be calculated "exactly". The "exact" filtered heat flux vector, which cannot be calculated within an actual LES, is expressed as follows:

$$\begin{aligned}\overline{Q_j(\Psi)} = &-\overline{\left\{\kappa + \sum_{k=1}^{N-1}\sum_{l>k}^{N} X_k X_l \alpha_{BK}^{kl}\alpha_{BK}^{kl}\frac{R\rho}{M_m}D_m^{kl}\right\}\frac{\partial T}{\partial x_j}} \\ &-\overline{\sum_{k=1}^{N}\left\{X_k\sum_{l\neq k}^{N}[\frac{M_l}{M_m^2}X_l\alpha_{BK}^{kl}\rho D_m^{kl}]V_{,k}\right\}\frac{\partial P}{\partial x_j}} \\ &-\overline{\sum_{o=1}^{N-1}\sum_{k=1}^{N}\left\{RT\sum_{l\neq k}^{N}[\frac{M_l}{M_m^2}X_l\alpha_{BK}^{kl}\rho D_m^{kl}]\alpha_D^{ko}\right\}\frac{\partial X_o}{\partial x_j}},\end{aligned} \tag{3.8}$$

In contrast, the "resolved" heat flux vector that can be calculated within an LES is:

$$Q_j(\overline{\Psi}) = -\left\{\kappa(\overline{\Psi}) + \sum_{k=1}^{N-1}\sum_{l>k}^{N} X_k(\overline{\Psi})X_l(\overline{\Psi})\alpha_{BK}^{kl}(\overline{\Psi})\alpha_{BK}^{kl}(\overline{\Psi})\frac{R\overline{\rho}}{M_m}D_m^{kl}(\overline{\Psi})\right\}\frac{\partial T(\overline{\Psi})}{\partial x_j} \quad (3.9)$$
$$-\sum_{k=1}^{N}\left\{X_k(\overline{\Psi})\sum_{l\neq k}^{N}[\frac{M_l}{M_m^2}X_l(\overline{\Psi})\alpha_{BK}^{kl}(\overline{\Psi})\overline{\rho}D_m^{kl}(\overline{\Psi})]V_{,k}(\overline{\Psi})\right\}\frac{\partial P(\overline{\Psi})}{\partial x_j}$$
$$-\sum_{o=1}^{N-1}\sum_{k=1}^{N}\left\{RT(\overline{\Psi})\sum_{l\neq k}^{N}[\frac{M_l}{M_m^2}X_l(\overline{\Psi})\alpha_{BK}^{kl}(\overline{\Psi})\overline{\rho}D_m^{kl}(\overline{\Psi})]\alpha_D^{ko}(\overline{\Psi})\right\}\frac{\partial X_o(\overline{\Psi})}{\partial x_j},$$

where all the terms, $f(\overline{\Psi})$ depend on the variable set $\overline{\Psi}$ and can be calculated in LES environment. The difference between the Eqs. (3.8)-(3.9) gives the subgrid heat flux vector which might require modeling and is the focus of the current work. The subgrid analysis aims to analyze the possible necessity of modeling the subgrid heat flux vector by calculating the correlation coefficients and ratio distributions of $|\overline{Q_j(\Psi)}|$ to $|Q_j(\overline{\Psi})|$. Ratios relative to other subgrid terms in the filtered energy equation [Eq. (3.4)] are also considered. Note that there are a number of ways in which to interpret the proper caclulation of $Q_j(\overline{\Psi})$ within an actual LES. Equation (3.9) above can certainly be used directly. However, for current research in our research group has already shown that the subgrid pressure and temperature can be significant. Models for these terms have been proposed and under further development [20, 21]. In such a case an LES would actually have more accurate estimates of the filtered temperature and pressure available:

$$\langle\langle T(\Psi)\rangle\rangle \approx T(\overline{\Psi}) + T_{sgs,model}, \quad (3.10)$$

$$\overline{P(\Psi)} \approx P(\overline{\Psi}) + P(\overline{\Psi}) + P_{sgs,model}, \quad (3.11)$$

($\langle\langle T(\Psi)\rangle\rangle$ is typically used in LES for compressible flows). Given such models, it would make sense to consider them in calculating $Q_j(\overline{\Psi})$. Therefore, for the purposes of this work, we assume "perfect" models for the SGS temperature and pressure area available as a best case scenario (i.e. replacing $T(\overline{\Psi})$ and $P(\overline{\Psi})$ with $\overline{T(\Psi)}]$ and $\overline{P(\Psi)}$ above). As such, the heat flux is calculated as:

$$
\begin{aligned}
Q_j(\overline{\Psi}) = &-\left\{\kappa(\overline{\Psi}) + \sum_{k=1}^{N-1}\sum_{l>k}^{N} X_k(\overline{\Psi})X_l(\overline{\Psi})\alpha_{BK}^{kl}(\overline{\Psi})\alpha_{BK}^{kl}(\overline{\Psi})\frac{R\overline{\rho}}{M_m}D_m^{kl}(\overline{\Psi})\right\}\frac{\partial\overline{T(\Psi)}}{\partial x_j} \\
&-\sum_{k=1}^{N}\left\{X_k(\overline{\Psi})\sum_{l\neq k}^{N}[\frac{M_l}{M_m^2}X_l(\overline{\Psi})\alpha_{BK}^{kl}(\overline{\Psi})\overline{\rho}D_m^{kl}(\overline{\Psi})]V_{,k}(\overline{\Psi})\right\}\frac{\partial P\overline{(\Psi)}}{\partial x_j} \\
&-\sum_{o=1}^{N-1}\sum_{k=1}^{N}\left\{RT(\overline{\Psi})\sum_{l\neq k}^{N}[\frac{M_l}{M_m^2}X_l(\overline{\Psi})\alpha_{BK}^{kl}(\overline{\Psi})\overline{\rho}D_m^{kl}(\overline{\Psi})]\alpha_D^{ko}(\overline{\Psi})\right\}\frac{\partial X_o(\overline{\Psi})}{\partial x_j},
\end{aligned}
\tag{3.12}
$$

The analysis is done in a both "global" flame manner (for the current work conditioned on $0.01 \leq \phi \leq 0.99$; see below), as well as for local regions which are defined by conditionally filtering on:

* The stoichiometric condition, $0.1 \leq \phi \leq 0.2$,
* Large filtered temperature variance, $\langle\langle T''^2\rangle\rangle/E(\langle\langle T''^2\rangle\rangle) \geq 2$,
* Large subgrid kinetic energy, $\langle\langle k_{sgs}\rangle\rangle/E(\langle\langle k_{sgs}\rangle\rangle) \geq 2$,
* Large filtered mixture fraction variance, $\langle\langle \phi''^2\rangle\rangle/E(\langle\langle \phi''^2\rangle\rangle) \geq 2$,
* High reaction rate regions, $\omega^\alpha/E(\omega^\alpha \geq 2)$,
* High filtered scalar dissipation, $\overline{\chi^\phi}/E(\overline{\chi^\phi}) \geq 2$,
* Elevated temperature regions, $T/T_0 \geq 2$,

where $E(\Phi)$ indicates the expected value (average) over the global flame region ($0.01 \leq \phi \leq 0.99$). In the above, ϕ is the mixture fraction which is defined as follows:

$$\phi = \frac{sY^{H_2} - Y^{O_2} + Y_0^{O_2}}{sY_0^{H_2} + Y_0^{O_2}}, \tag{3.13}$$

where $0 \leq \phi \leq 1$, s is the stoichiometric constant, Y^{H_2} and Y^{O_2} are the local mass fraction for H_2 and O_2, respectively, and $Y_0^{H_2}$ and $Y_0^{O_2}$ are the corresponding free stream values. In the pure fuel region $\phi = 1$, and in the pure oxidizer region $\phi = 0$. Intermediate values indicate varying degrees of mixedness. The mixture fraction and its dissipation are important quantities in many turbulent combustion models. The reason for considering each of these regions seperately is that flame dynamics such as ignition, extinction and reignition are known to be highly localized. Therefore, if a model were deemed to perform well when only globally averaged it may not necessarily perform well locally in important flame regions.

To be able to neglect the subgrid heat flux vector, the condition of $\overline{Q_j(\Psi)} \approx Q_j(\overline{\Psi})$ should at least be satisfied. This would be indicated by the correlation coefficients between these two terms near to unity for all regions above (defined below). However, if the correlation coefficients have low values, modeling may be required for the subgrid heat flux vector. Vector magnitudes, and possibly directions, also need to be considered as correlation coefficients only indicate a statistical relationship, but not necessarily an equal amplitude (e.g. $sin(x)$ and $100sin(x)$ have a unity correlation coefficient).

3.1.1 Correlation Coefficients

In Fig. 3.2 (a), correlation coefficients are depicted for the reacting flow at $Re_F = 850$, $C(|\overline{Q_j(\Psi)}|, |Q_j(\overline{\Psi})|)$, for the actual heat flux vector magnitude and the heat flux vector magnitude calculated using filtered primitive variables. For random variables A and B the correlation coefficient is expressed as follows:

$$C(A,B) = \frac{E[(A - E(A))((B) - E(B))]}{\sqrt{E[(A - E(A))]^2 E[((B) - E(B))]^2}}, \tag{3.14}$$

Correlation coefficient may vary over the range:

$$-1 \leq C(A,B) \leq 1. \tag{3.15}$$

Zero correlation coefficient implies no statistical relationship between A and B, 1 indicates *perfect* correlation, and -1 indicates *perfect negative* correlation.

Correlation coefficients are calculated using various filter widths ($\Delta/\Delta x_1 = 0, 6, 10, 16, 20$), and results are conditioned on both global and the aforementioned conditioned flow regions [i.e. the expectation operator is conditioned exclusively to points in these particular regions Eq. (3.14)]. For the case of $\Delta/\Delta x_1 = 0$ all of the correlation coefficients of $\overline{Q_j(\Psi)}$ and $Q_j(\overline{\Psi})$ are unity both globally and for localized regions of the flow as a zero filter width yields the original DNS data. It is worth mentioning that the filter width is non-dimensionalized by the initial mixing layer vorticity thickness, $\delta_{\omega 0}$, in most of what follows. Figure 3.1.1 shows relative filter widths to scale for the Re_F =2500 flame at a time of t^*= 115 [20]. Hereinafter, only the "long time" results are analyzed for each simulation. These correspond to non-dimensional times of t^* =80, 115, for the $Re_F = 850$ and 2500 cases, respectively. A time of t^* =80 is used for the mixing case.

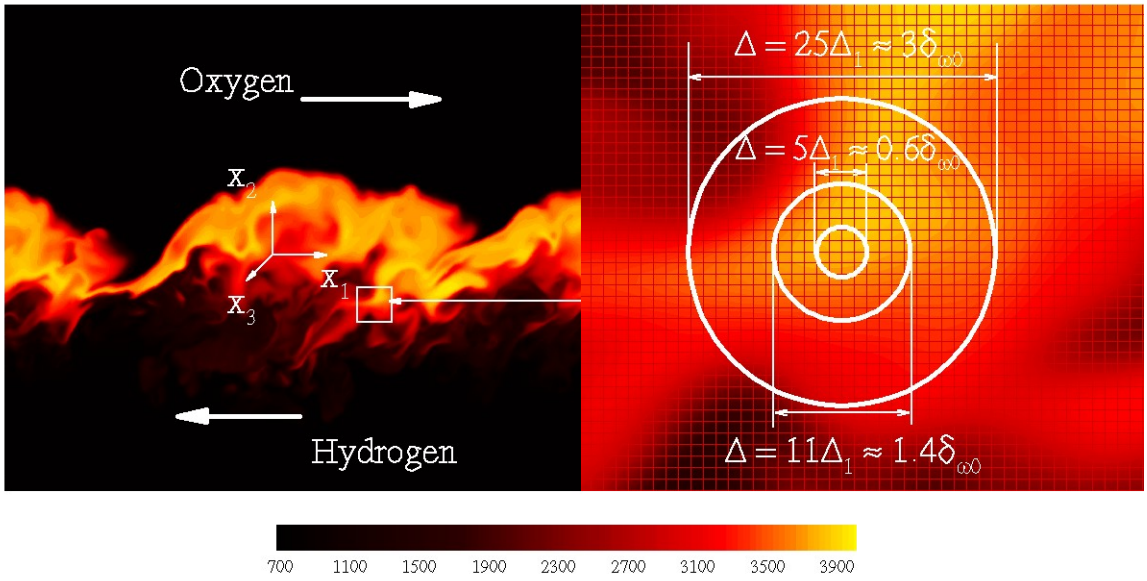

Figure 3.1: Relative filter widths. The contours are for temperature for the $Re_F = 2500$ flame at $t^* = 115$ [20].

Figure 3.2 presents all correlation coefficients for $\overline{Q_j(\Psi)}$ and $Q_j(\overline{\Psi})$ as functions of the filter width for both the $Re_F = 850$ and 2500 flames. As the filter width is increased, the general tendency of the globally conditioned correlation coefficient is to decline and to remain around 0.7. In Fig. 3.2 (a) ($Re_F = 850$), the regions, III- $\langle\langle T''^2\rangle\rangle/E(\langle\langle T''^2\rangle\rangle) \geq 2$, IV- $\langle\langle k_{sgs}\rangle\rangle/E(\langle\langle k_{sgs}\rangle\rangle) \geq 2$, V- $\langle\langle \phi''^2\rangle\rangle/E(\langle\langle \phi''^2\rangle\rangle) \geq 2$, correlation coefficients are ≤ 0.5 which indicates that some regions are poorly correlated. For large filtered temperature variance, $\langle\langle T''^2\rangle\rangle/E(\langle\langle T''^2\rangle\rangle) \geq 2$, the correlation coefficient increases from ≈ 0.3 to ≈ 0.5 with increasing filter widths. Even though the correlation coefficient increases, the values still remains poor. Another poorly correlated region is the large subgrid kinetic energy, $\langle k_{sgs}\rangle/E(\langle k_{sgs}\rangle) \geq 2$, remains below 0.4 for all the filter widths. For the region corresponding to the large filtered mixture fraction variance, $\langle\langle \phi''^2\rangle\rangle/E(\langle\langle \phi''^2\rangle\rangle) \geq 2$, however, the correlation coefficient has the tendency to increase again, though it only reaches values ≈ 0.5.

In Fig. 3.2 (b), correlation coefficients for, $C(|\overline{Q_j(\Psi)}|, |Q_j(\overline{\Psi})|)$, are depicted for $Re_F = 2500$; again for the same filter widths and regions which are considered in Fig. 3.2 (a). At higher Reynolds number, however, the correlation coefficients possess better values for all the filter widths in all the regions concerned; though the regions of elevated temperature, $\langle\langle T''^2\rangle\rangle/E(\langle\langle T''^2\rangle\rangle) \geq 2$, and large reaction rate, $\dot{\omega}^{OH}/E(\dot{\omega}^{OH} \geq 2)$, in particular are still very poor. Regions of large subgrid temperature variance are indicative of large local temperature gradients (and therefore large local heat flux). The detailed correlation coefficients are provided in Tables 3.1 - 3.4 at $Re_F = 850$ and 2500 for $\Delta/\delta_{\omega,0} \approx 0.71$ - 2.4. All of the raw data used to generate the correlation coefficients are provided in the form of scatter plots in Figs. 3.3 and 3.4 for $Re_F = 850$ and 2500, respectively.

Figure 3.5 shows the correlation coefficients for the pure mixing case at $Re = 2000$ for varying filter widths, $\Delta/\delta_{w0} \approx 0.71/2.4$, and detailed information can be

seen in Tables 3.1 - 3.4 for $\Delta/\delta_{\omega,0} \approx 0.71/2.4$. The correlation coefficients show that the subgrid heat flux vector may be important for the pure mixing case as well. However, subgrid vector magnitudes relative to both the filtered variables and other subgrid terms in the LES energy equation need to be examined before more definitive conclusions can be made.

Table 3.5 includes the correlation coefficients for, $C(|\partial Q_j(\overline{\Psi})/\partial x_j|, |\partial \overline{Q}_j(\Psi)/\partial x_j|)$, for both reacting cases at filter width, $\Delta/\delta_{\omega,0} \approx 1.92$. The values indicate that correlation significantly deteriorated when considering the divergence. This is common for LES SGS models since differentiation enhances small scale effectas, and SGS terms are inherently small scale.

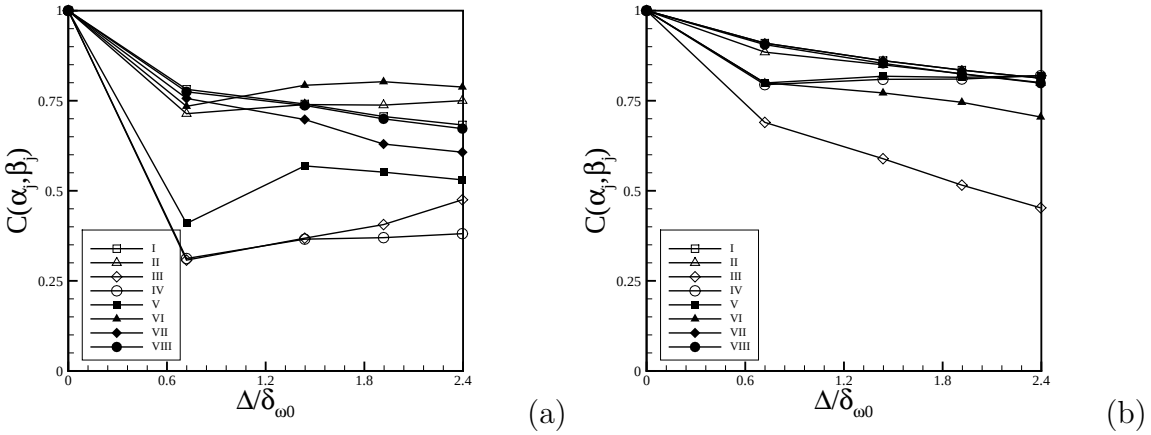

Figure 3.2: Correlation coefficients between the actual heat flux vector magnitude, $|\alpha_j| = |\overline{Q_j(\Psi)}|$, and the heat flux vector magnitude calculated using filtered primitive variables, $|\beta_j| = |Q_j(\overline{\Psi})|$. (a) Re_F=850, (b) Re_F=2500, in regions described by: I- $0.01 \leq \phi \leq 0.99$, II- $0.1 \leq \phi \leq 0.2$, III- $\langle\langle T''^2\rangle\rangle/E(\langle\langle T''^2\rangle\rangle) \geq 2$, IV- $\langle\langle k_{sgs}\rangle\rangle/E(\langle\langle k_{sgs}\rangle\rangle) \geq 2$, V- $\langle\langle \phi''^2\rangle\rangle/E(\langle\langle \phi''^2\rangle\rangle) \geq 2$, VI- $\dot{\omega}^{OH}/E(\dot{\omega}^{OH} \geq 2)$, VII- $\overline{\chi^\phi}/E(\overline{\chi^\phi}) \geq 2$ and VIII- $T/T_0 \geq 2$.

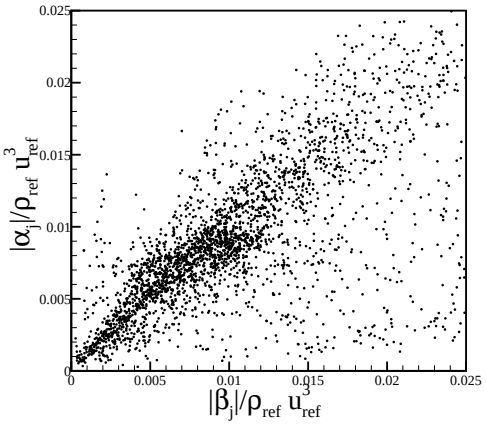
$|\alpha_j|/\rho_{ref}\, u^3_{ref}$
$|\beta_j|/\rho_{ref}\, u^3_{ref}$
0
0.005
0.01
0.015
0.02
0.025

(a)

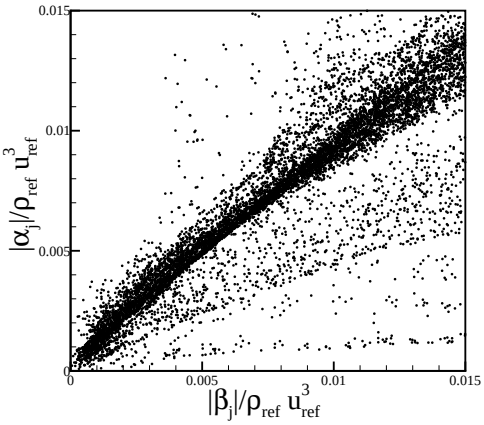
$|\alpha_j|/\rho_{ref}\, u^3_{ref}$
$|\beta_j|/\rho_{ref}\, u^3_{ref}$
0
0.005
0.01
0.015

(b)

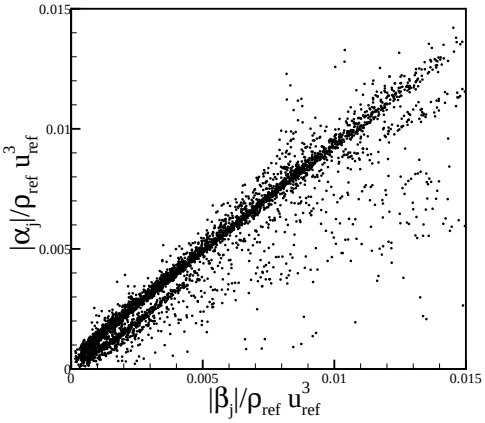
$|\alpha_j|/\rho_{ref}\, u^3_{ref}$
$|\beta_j|/\rho_{ref}\, u^3_{ref}$
0
0.005
0.01
0.015

(c)

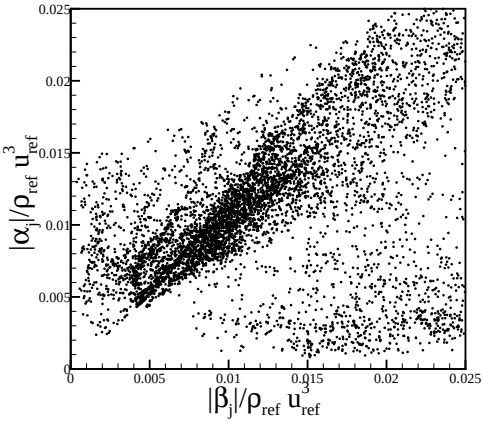
$|\alpha_j|/\rho_{ref}\, u^3_{ref}$
$|\beta_j|/\rho_{ref}\, u^3_{ref}$
0
0.005
0.01
0.015
0.02
0.025

(d)

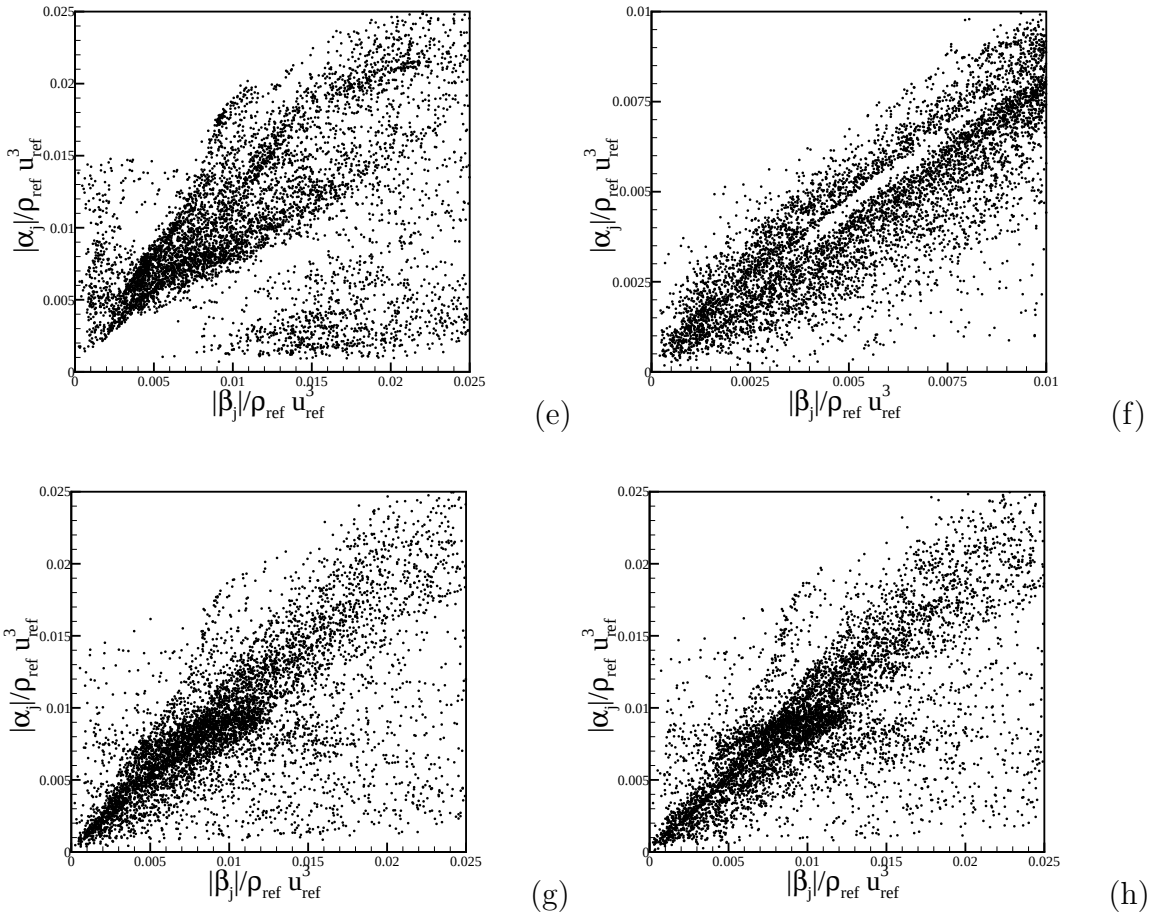

Figure 3.3: Scatter plots of $|\alpha_j|$ vs. $|\beta_j|$, where $|\alpha_j| = |\overline{Q_j(\Psi)}|$, and $|\beta_j| = |Q_j(\overline{\Psi})|$, at Re_F =850 in regions described by: (a) $0.01 \leq \phi \leq 0.99$, (b) $0.1 \leq \phi \leq 0.2$, (c) $\langle\langle T''^2\rangle\rangle / E(\langle\langle T''^2\rangle\rangle) \geq 2$, (d) $\langle\langle k_{sgs}\rangle\rangle / E(\langle\langle k_{sgs}\rangle\rangle) \geq 2$, (e) $\langle\langle \phi''^2\rangle\rangle / E(\langle\langle \phi''^2\rangle\rangle) \geq 2$, (f) $\overset{\bullet}{\omega}{}^{OH} / E(\overset{\bullet}{\omega}{}^{OH} \geq 2)$, (g) $\overline{\chi^\phi} / E(\overline{\chi^\phi}) \geq 2$ and (h) $T/T_0 \geq 2$.

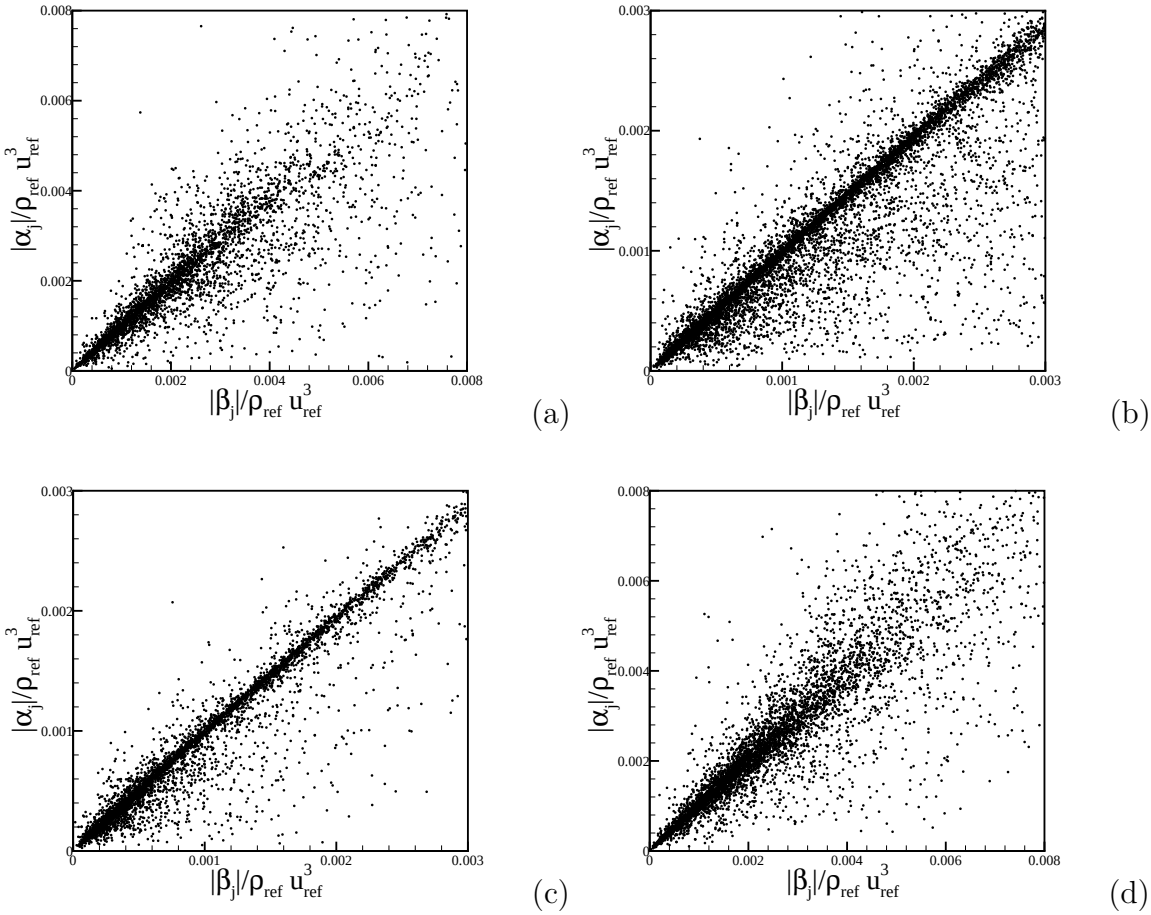

3.1.2 Vector Magnitude Ratio Distributions

An analysis of the relative magnitudes of the various heat flux vector forms is done for both high pressure reacting flows at Re_F =850 and 2500 and for the non-reacting flow at Re =2000. The probability density function (PDF) of the ratios of $|\overline{Q_j(\Psi)}|$ and $|Q_j(\overline{\Psi})|$ are calculated to more deeply examine the role of the subgrid heat flux vector, $|Q_{sgs,_j}|$. Additionally, the ratios of $|\partial\overline{Q_j(\Psi)}/\partial x_j|$ and $|\partial Q_j(\overline{\Psi})/\partial x_j|$, are also tested, as it is the divergences that appear in the LES energy equation. Figures 3.6 and 3.7 include both the PDFs of the ratios of $|\overline{Q_j(\Psi)}|$, $|Q_j(\overline{\Psi})|$ and their

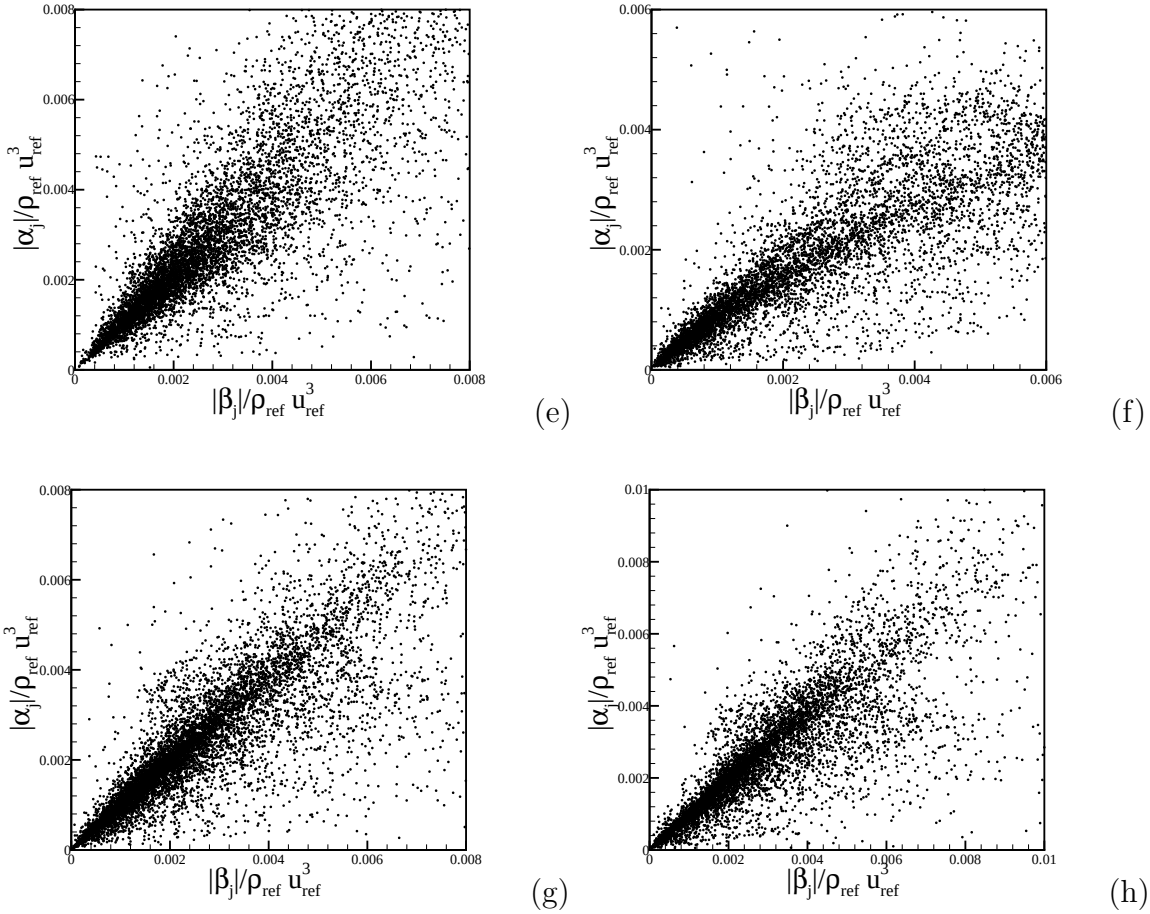

Figure 3.4: Scatter plots of $|\alpha_j|$ vs. $|\beta_j|$, where $|\alpha_j| = |\overline{Q_j(\Psi)}|$, and $|\beta_j| = |Q_j(\overline{\Psi})|$, at Re_F=2500 in regions described by: (a) $0.01 \leq \phi \leq 0.99$, (b) $0.1 \leq \phi \leq 0.2$, (c) $\langle\langle T''^2\rangle\rangle / E(\langle\langle T''^2\rangle\rangle) \geq 2$, (d) $\langle\langle k_{sgs}\rangle\rangle / E(\langle\langle k_{sgs}\rangle\rangle) \geq 2$, (e) $\langle\langle \phi''^2\rangle\rangle / E(\langle\langle \phi''^2\rangle\rangle) \geq 2$, (f) $\overset{\bullet}{\omega}{}^{OH} / E(\overset{\bullet}{\omega}{}^{OH} \geq 2)$, (g) $\overline{\chi^\phi} / E(\overline{\chi^\phi}) \geq 2$ and (h) $T/T_0 \geq 2$.

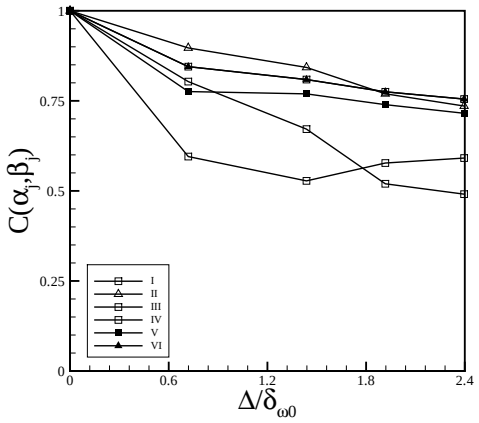

Figure 3.5: Correlation coefficients between the actual heat flux vector magnitude, $|\alpha_j| = |\overline{Q_j(\Psi)}|$, and the heat flux vector magnitude calculated using filtered primitive variables, $|\beta_j| = |Q_j(\overline{\Psi})|$. Re=2000, in regions described by: I- $0.01 \leq \phi \leq 0.99$, II- $0.1 \leq \phi \leq 0.2$, III- $\langle\langle T''^2\rangle\rangle / E(\langle\langle T''^2\rangle\rangle) \geq 2$, IV- $\langle\langle k_{sgs}\rangle\rangle / E(\langle\langle k_{sgs}\rangle\rangle) \geq 2$, V- $\langle\langle \phi''^2\rangle\rangle / E(\langle\langle \phi''^2\rangle\rangle) \geq 2$, VI- $\overline{\chi^\phi} / E(\overline{\chi^\phi}) \geq 2$.

Regions	Re_F Numbers		
	850	2500	2000
$0.01 \leq \phi \leq 0.99$	0.78	0.91	0.85
$0.1 \leq \phi \leq 0.2$	0.71	0.88	0.90
$\langle\langle T''^2\rangle\rangle / E(\langle\langle T''^2\rangle\rangle) \geq 2$	0.30	0.69	80
$\langle\langle k_{sgs}\rangle\rangle / E(\langle\langle k_{sgs}\rangle\rangle) \geq 2$	0.31	0.80	0.60
$\langle\langle \phi''^2\rangle\rangle / E(\langle\langle \phi''^2\rangle\rangle) \geq 2$	0.41	0.80	0.78
$\overset{\bullet}{\omega}^{OH} / E(\overset{\bullet}{\omega}^{OH} \geq 2)$	0.73	0.80	N/A
$\overline{\chi^\phi} / E(\overline{\chi^\phi}) \geq 2$	0.78	0.91	0.85
$T/T_0 \geq 2$	0.77	0.91	N/A

Table 3.1: Correlation coefficients without model between the actual heat flux vector magnitude $|\overline{Q_j(\Psi)}|$, and the heat flux vector magnitude calculated using filtered primitive variables, $|Q_j(\overline{\Psi})|$, at filter width, $\Delta/\delta_{\omega 0} \approx 0.71$.

Regions	Re_F Numbers		
	850	2500	2000
$0.01 \leq \phi \leq 0.99$	0.74	0.86	0.81
$0.1 \leq \phi \leq 0.2$	0.73	0.85	0.85
$\langle\langle T''^2\rangle\rangle / E(\langle\langle T''^2\rangle\rangle) \geq 2$	0.36	0.59	0.68
$\langle\langle k_{sgs}\rangle\rangle / E(\langle\langle k_{sgs}\rangle\rangle) \geq 2$	0.36	0.81	0.53
$\langle\langle \phi''^2\rangle\rangle / E(\langle\langle \phi''^2\rangle\rangle) \geq 2$	0.57	0.82	0.77
$\overset{\bullet}{\omega}^{OH} / E(\overset{\bullet}{\omega}^{OH} \geq 2)$	0.79	0.77	N/A
$\overline{\chi^\phi} / E(\overline{\chi^\phi}) \geq 2$	0.70	0.86	0.81
$T/T_0 \geq 2$	0.74	0.86	N/A

Table 3.2: Correlation coefficients without model between the actual heat flux vector magnitude $|\overline{Q_j(\Psi)}|$, and the heat flux vector magnitude calculated using filtered primitive variables, $|Q_j(\overline{\Psi})|$, at filter width, $\Delta/\delta_{\omega 0} \approx 1.44$.

Regions	Re_F Numbers		
	850	2500	2000
$0.01 \leq \phi \leq 0.99$	0.70	0.84	0.78
$0.1 \leq \phi \leq 0.2$	0.73	0.83	0.77
$\langle\langle T''^2\rangle\rangle / E(\langle\langle T''^2\rangle\rangle) \geq 2$	0.40	0.52	0.52
$\langle\langle k_{sgs}\rangle\rangle / E(\langle\langle k_{sgs}\rangle\rangle) \geq 2$	0.36	0.81	0.58
$\langle\langle \phi''^2\rangle\rangle / E(\langle\langle \phi''^2\rangle\rangle) \geq 2$	0.55	0.81	0.74
$\overset{\bullet}{\omega}^{OH} / E(\overset{\bullet}{\omega}^{OH} \geq 2)$	0.80	0.75	N/A
$\overline{\chi^\phi} / E(\overline{\chi^\phi}) \geq 2$	0.63	0.83	0.78
$T/T_0 \geq 2$	0.70	0.82	N/A

Table 3.3: Correlation coefficients without model between the actual heat flux vector magnitude $|\overline{Q_j(\Psi)}|$, and the heat flux vector magnitude calculated using filtered primitive variables, $|Q_j(\overline{\Psi})|$, at filter width, $\Delta/\delta_{\omega 0} \approx 1.92$.

Regions	Re_F Numbers		
	850	2500	2000
$0.01 \leq \phi \leq 0.99$	0.68	0.81	0.76
$0.1 \leq \phi \leq 0.2$	0.75	0.80	0.74
$\langle\langle T''^2\rangle\rangle / E(\langle\langle T''^2\rangle\rangle) \geq 2$	0.47	0.45	0.50
$\langle\langle k_{sgs}\rangle\rangle / E(\langle\langle k_{sgs}\rangle\rangle) \geq 2$	0.38	0.82	0.60
$\langle\langle \phi''^2\rangle\rangle / E(\langle\langle \phi''^2\rangle\rangle) \geq 2$	0.53	0.82	0.71
$\overset{\bullet}{\omega}^{OH} / E(\overset{\bullet}{\omega}^{OH} \geq 2)$	0.79	0.70	N/A
$\overline{\chi^\phi} / E(\overline{\chi^\phi}) \geq 2$	0.61	0.85	0.76
$T/T_0 \geq 2$	0.67	0.80	N/A

Table 3.4: Correlation coefficients without model between the actual heat flux vector magnitude $|\overline{Q_j(\Psi)}|$, and the heat flux vector magnitude calculated using filtered primitive variables, $|Q_j(\overline{\Psi})|$, at filter width, $\Delta/\delta_{\omega 0} \approx 2.4$.

Regions	Re_F Numbers	
	850	2500
$0.01 \leq \phi \leq 0.99$	0.22	0.46
$0.1 \leq \phi \leq 0.2$	0.22	0.51
$\langle\langle T''^2\rangle\rangle / E(\langle\langle T''^2\rangle\rangle) \geq 2$	0.19	0.56
$\langle\langle k_{sgs}\rangle\rangle / E(\langle\langle k_{sgs}\rangle\rangle) \geq 2$	0.25	0.50
$\langle\langle \phi''^2\rangle\rangle / E(\langle\langle \phi''^2\rangle\rangle) \geq 2$	0.14	0.47
$\overset{\bullet}{\omega}^{OH} / E(\overset{\bullet}{\omega}^{OH} \geq 2)$	0.19	0.41
$\overline{\chi^\phi} / E(\overline{\chi^\phi}) \geq 2$	0.22	0.46
$T/T_0 \geq 2$	0.22	0.45

Table 3.5: Correlation coefficients without model between the divergence of actual heat flux vector magnitude, $|\partial\overline{Q_j(\Psi)}/\partial x_j|$ and the divergence of heat flux vector magnitude calculated using filtered primitive variables, $|\partial Q_j(\overline{\Psi})/\partial x_j|$, at filter width, $\Delta/\delta_{\omega 0} \approx 1.92$.

divergences at Re_F=850, and 2500 respectively. Figures 3.6 and 3.7 validate the previous results for correlation coefficients. The figures present PDFs depicted for ratios of both $|\overline{Q_j(\Psi)}|$, $|Q_j(\overline{\Psi})|$ and their divergences. If $Q_j(\overline{\Psi}) = \overline{Q_j(\Psi)}$ exactly then the PDFs would be delta functions centered at unity, $\delta(1)$. With this in mind, the figures clearly show that both the vector and divergence magnitudes PDFs can be substantially different than unity; i.e. the SGS heat flux is substantial. In Figs. 3.6 and 3.7 the PDFs of the ratios of $|\partial\overline{Q_j(\Psi)}/\partial x_j|$ and $|\partial Q_j(\overline{\Psi})/\partial x_j|$ are more flattened than the PDFs of the ratios of the $|\overline{Q_j(\Psi)}|$ and $|Q_j(\overline{\Psi})|$, which indicates statistically the divergences are not similar. Once the existence of the subgrid heat flux vector is validated, the ratio of the magnitude of the exact heat flux vector, $|\overline{Q_j(\Psi)}|$ and the ratio of the magnitude of the subgrid heat flux vector,$|Q_{sgs,_j}|$ to the magnitude of subgrid of other terms, $|(Pu_j)_{sgs}|$ and $|(\rho e_t u_j)_{sgs}|$, in the LES energy equation is considered. The ratio of the terms and the ratios of their gradients that are calculated are:

* $|\overline{Q_j(\Psi)}|/|(\rho e_t u_j)_{sgs}|$
* $|\overline{Q_j(\Psi)}|/|(Pu_j)_{sgs}|$
* $|Q_{sgs,_j}|/|(\rho e_t u_j)_{sgs}|$
* $|Q_{sgs,_j}|/|(Pu_j)_{sgs}|$
* $|\partial\overline{Q_j(\Psi)}/\partial x_j|/|\partial(\rho e_t u_j)_{sgs}/\partial x_j|$
* $|\partial\overline{Q_j(\Psi)}/\partial x_j|/|\partial(Pu_j)_{sgs}/\partial x_j|$
* $|\partial Q_{sgs,_j}/|\partial x_j|/|\partial(\rho e_t u_j)_{sgs}/\partial x_j|$
* $|\partial Q_{sgs,_j}/|\partial x_j|/|\partial(Pu_j)_{sgs}/\partial x_j|$.

Figures 3.8 - 3.11 include the PDFs of the ratios of magnitude of the subgrid terms themselves, Figures 3.12 - 3.15 present the PDFs of ratios of the divergences. Except the high reaction rate and elevated temperature regions, all the following figures include both reacting and non-reacting simulations (these regions being inapplicable to the mixing case).

In Figs. 3.8 3.9, while the subgrid pressure work term, $|(Pu_j)_{sgs}|$, is smaller than the exact heat flux vector, $|\overline{Q_j(\Psi)}|$, the subgrid convective total energy term, $|(\rho e_t u_j)_{sgs}|$ is larger than $|\overline{Q_j(\Psi)}|$. Additionally, $|(Pu_j)_{sgs}|$ and $|(\rho e_t u_j)_{sgs}|$ are bigger than the exact heat flux vector in the flow at Re_F =2500. In Fig. 3.10, it can be seen that the subgrid convective total energy term is significantly larger than the subgrid heat flux vector, $|Q_{sgs_j}|$. However, the subgrid heat flux vector seems is generally smaller than the subgrid pressure work term. Figure 3.11 shows that $|Q_{sgs_j}|$ is of the same order as $|\overline{Q_j(\Psi)}|$, which indicates that the subgrid heat flux vector is as important as the exact heat flux vector. Figures 3.12 and 3.13 indicate that the divergences of $|(Pu_j)_{sgs}|$ and $|(\rho e_t u_j)_{sgs}|$ are still larger than the divergence $|\overline{Q_j(\Psi)}|$. Figure 3.14 presents the PDFs of the ratio of $|\partial Q_{sgs_j}/\partial x_j|$ to $|\partial(\rho e_t u_j)_{sgs}/\partial x_j|$. The ratios show that the term $|\partial Q_{sgs_j}/\partial x_j|$ is larger than $|\partial(\rho e_t u_j)_{sgs}/\partial x_j|$ both globally and locally. However, the divergence of subgrid pressure work magnitude is significantly bigger than the divergences of subgrid heat flux vector for both reacting and non-reacting flows.

The results presented above contain a large wealth of information relevant to LES of reacting flows. However, for the purposes odf the present thesis, the primary conclusion is that the SGS heat flux vector can be a substantial term in the LES energy equation and therefore, may require modeling.

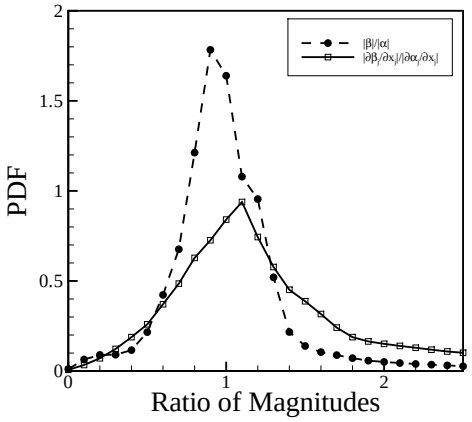
|β_i/|α|
|∂β_j/∂x_j|/|∂α_j/∂x_j|
PDF
Ratio of Magnitudes

(a)

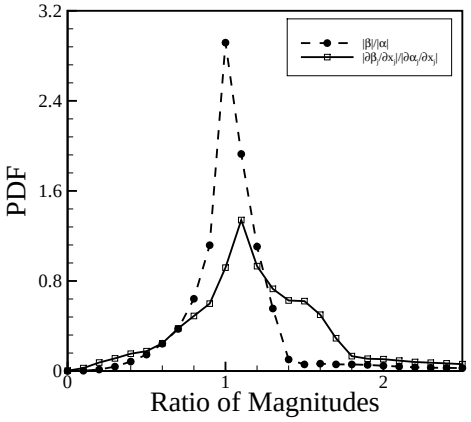
|β_i/|α|
|∂β_j/∂x_j|/|∂α_j/∂x_j|
PDF
Ratio of Magnitudes

(b)

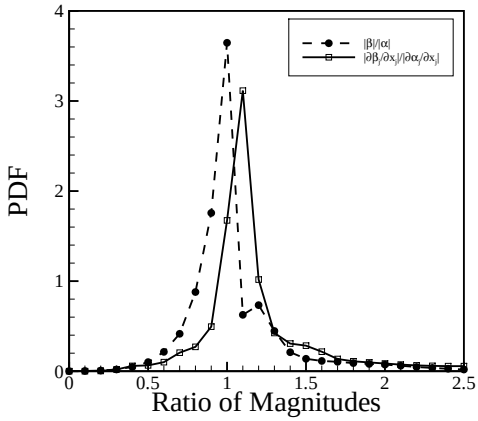
|β_i/|α|
|∂β_j/∂x_j|/|∂α_j/∂x_j|
PDF
Ratio of Magnitudes

(c)

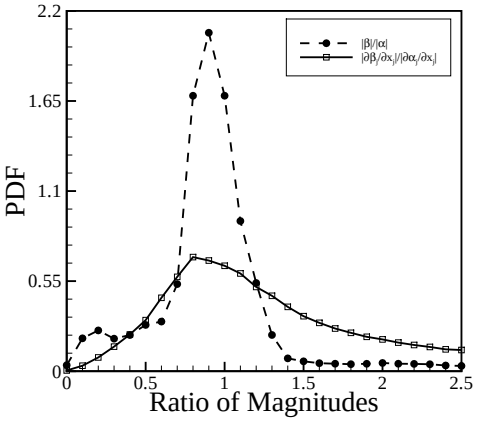
|β_i/|α|
|∂β_j/∂x_j|/|∂α_j/∂x_j|
PDF
Ratio of Magnitudes

(d)

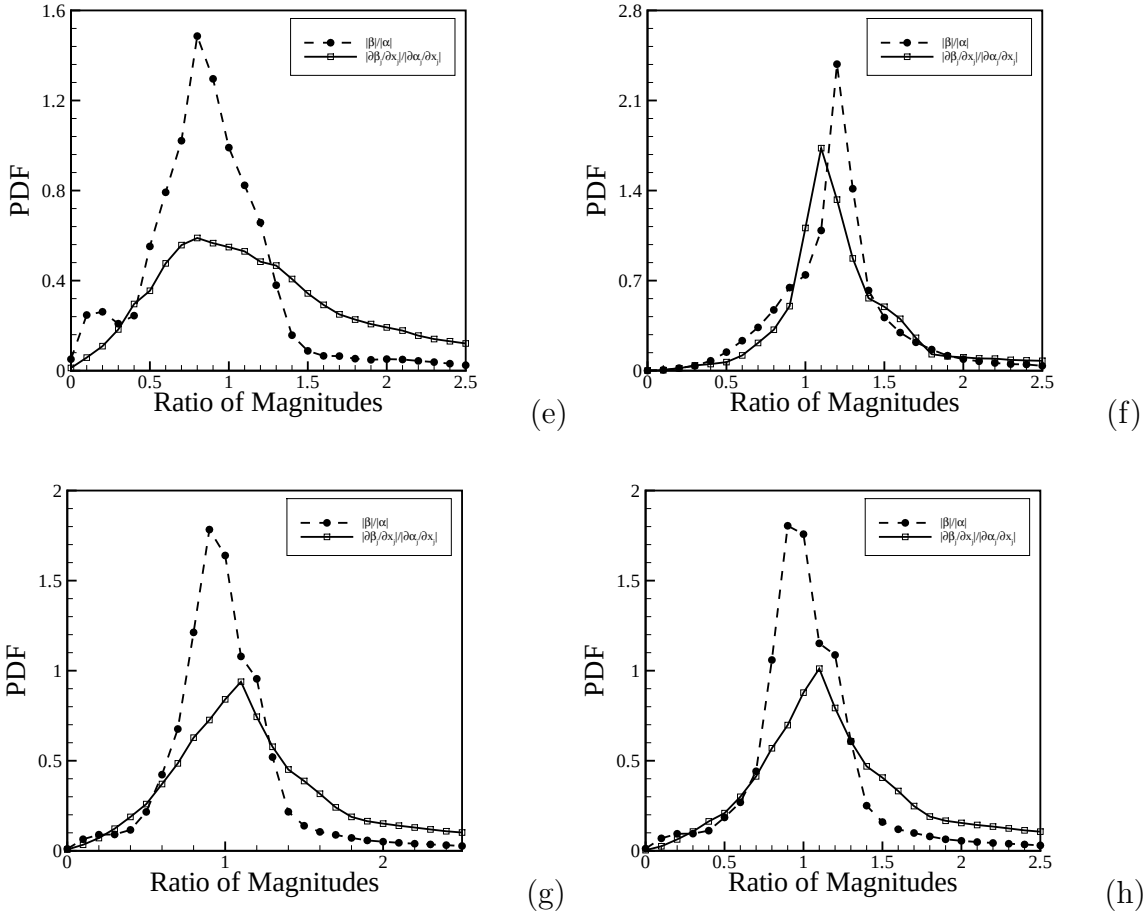

Figure 3.6: PDFs containing the ratios of $|\alpha_j|/|\beta_j|$, where $|\alpha_j| = |\overline{Q_j(\Psi)}|$, $|\beta_j| = |Q_j(\overline{\Psi})|$, and $|\partial\alpha_j/\partial x_j|/|\partial\beta_j/\partial x_j| = |\partial\overline{Q_j(\Psi)}/\partial x_j|/|\partial Q_j(\overline{\Psi})/\partial x_j|$ at Re_F =850 in regions described by: (a) $0.01 \leq \phi \leq 0.99$, (b) $0.1 \leq \phi \leq 0.2$, (c) $\langle\langle T''^2\rangle\rangle/E(\langle\langle T''^2\rangle\rangle) \geq 2$, (d) $\langle\langle k_{sgs}\rangle\rangle/E(\langle\langle k_{sgs}\rangle\rangle) \geq 2$, (e) $\langle\langle \phi''^2\rangle\rangle/E(\langle\langle \phi''^2\rangle\rangle) \geq 2$, (f) $\overset{\bullet}{\omega}{}^{OH}/E(\overset{\bullet}{\omega}{}^{OH} \geq 2)$, (g) $\overline{\chi^\phi}/E(\overline{\chi^\phi}) \geq 2$ and (h) $T/T_0 \geq 2$.

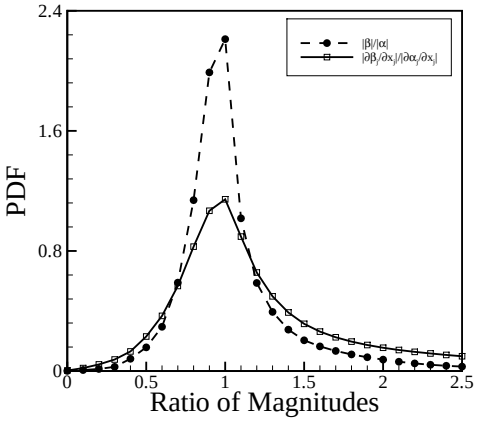
PDF
Ratio of Magnitudes
|β_j/|α|
|∂β_j/∂x_j|/|∂α_j/∂x_j|

(a)

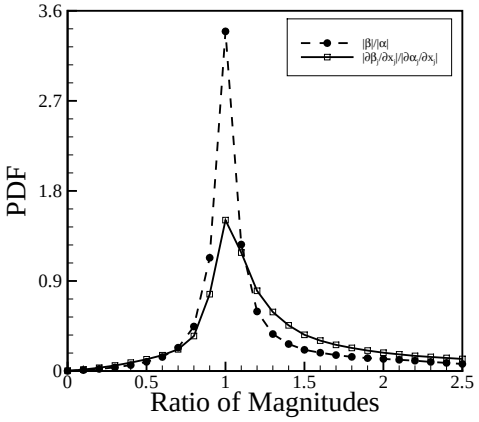
PDF
Ratio of Magnitudes
|β_j/|α|
|∂β_j/∂x_j|/|∂α_j/∂x_j|

(b)

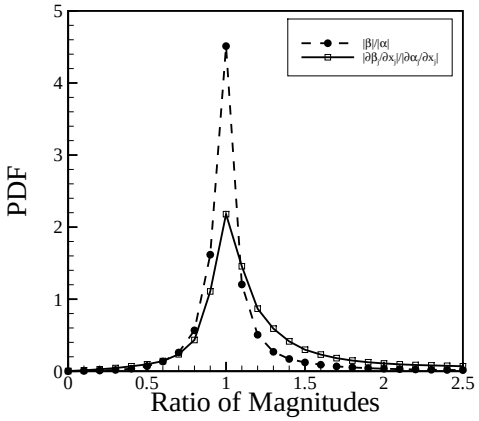
PDF
Ratio of Magnitudes
|β_j/|α|
|∂β_j/∂x_j|/|∂α_j/∂x_j|

(c)

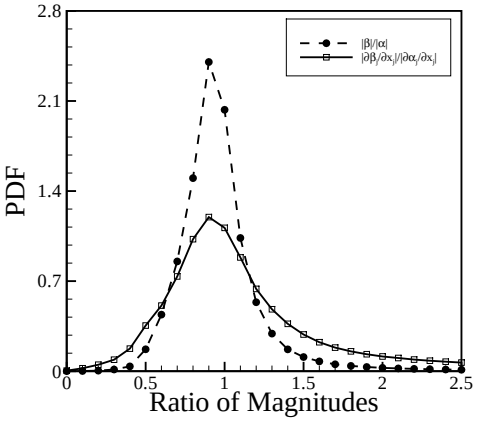
PDF
Ratio of Magnitudes
|β_j/|α|
|∂β_j/∂x_j|/|∂α_j/∂x_j|

(d)

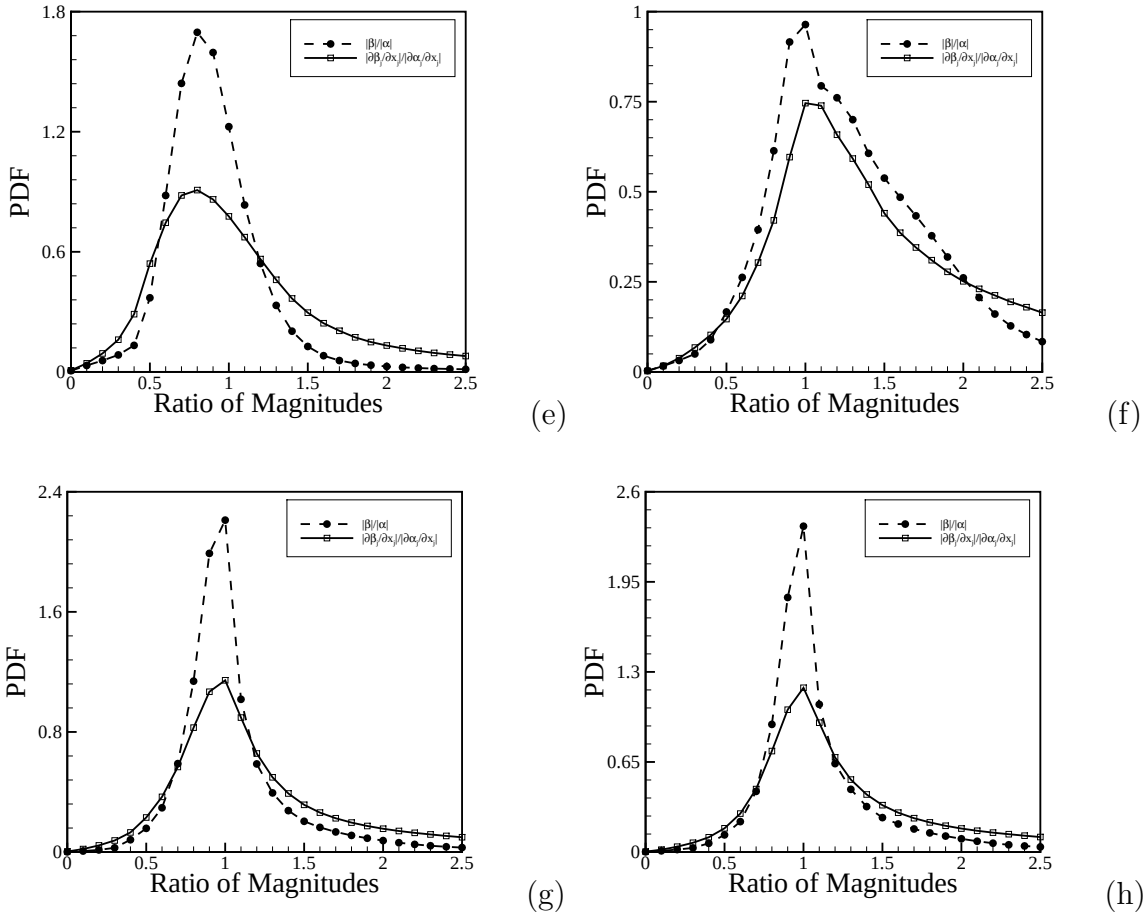

Figure 3.7: PDFs containing the ratios of $|\alpha_j|/|\beta_j|$, where $|\alpha_j| = |\overline{Q_j(\Psi)}|$, $|\beta_j| = |Q_j(\overline{\Psi})|$, and $|\partial\alpha_j/\partial x_j|/|\partial\beta_j/\partial x_j| = |\partial\overline{Q_j(\Psi)}/\partial x_j|/|\partial Q_j(\overline{\Psi})/\partial x_j|$ at Re_F =2500, in regions described by: (a) $0.01 \leq \phi \leq 0.99$, (b) $0.1 \leq \phi \leq 0.2$, (c) $\langle\langle T''^2\rangle\rangle/E(\langle\langle T''^2\rangle\rangle) \geq 2$, (d) $\langle\langle k_{sgs}\rangle\rangle/E(\langle\langle k_{sgs}\rangle\rangle) \geq 2$, (e) $\langle\langle \phi''^2\rangle\rangle/E(\langle\langle \phi''^2\rangle\rangle) \geq 2$, (f) $\overset{\bullet}{\omega}{}^{OH}/E(\overset{\bullet}{\omega}{}^{OH} \geq 2)$, (g) $\overline{\chi^\phi}/E(\overline{\chi^\phi}) \geq 2$ and (h) $T/T_0 \geq 2$.

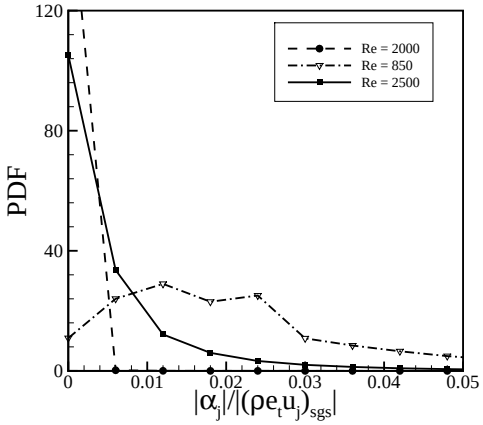
Re = 2000
Re = 850
Re = 2500
PDF
$|\alpha_j|/|(\rho e_t u_j)_{sgs}|$

(a)

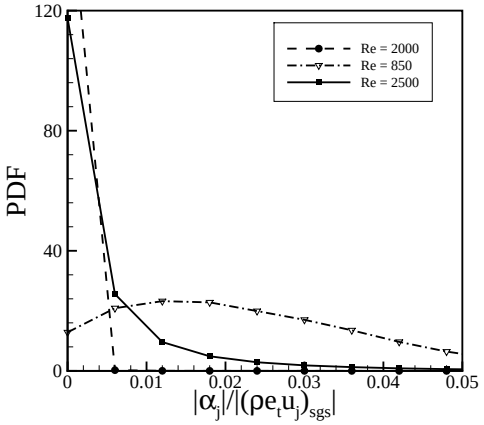
Re = 2000
Re = 850
Re = 2500
PDF
$|\alpha_j|/|(\rho e_t u_j)_{sgs}|$

(b)

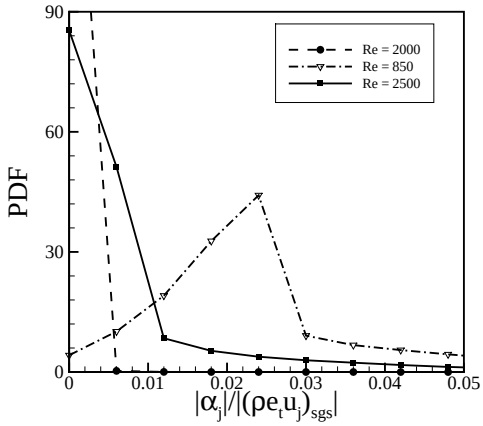
Re = 2000
Re = 850
Re = 2500
PDF
$|\alpha_j|/|(\rho e_t u_j)_{sgs}|$

(c)

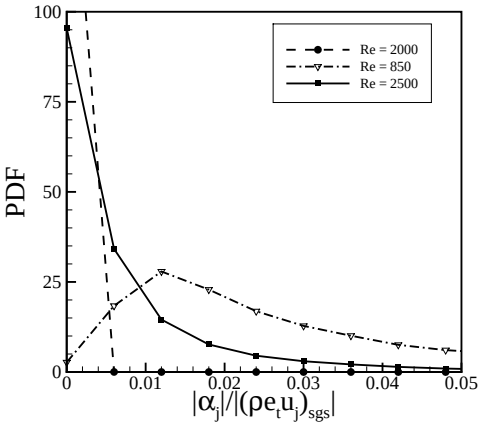
Re = 2000
Re = 850
Re = 2500
PDF
$|\alpha_j|/|(\rho e_t u_j)_{sgs}|$

(d)

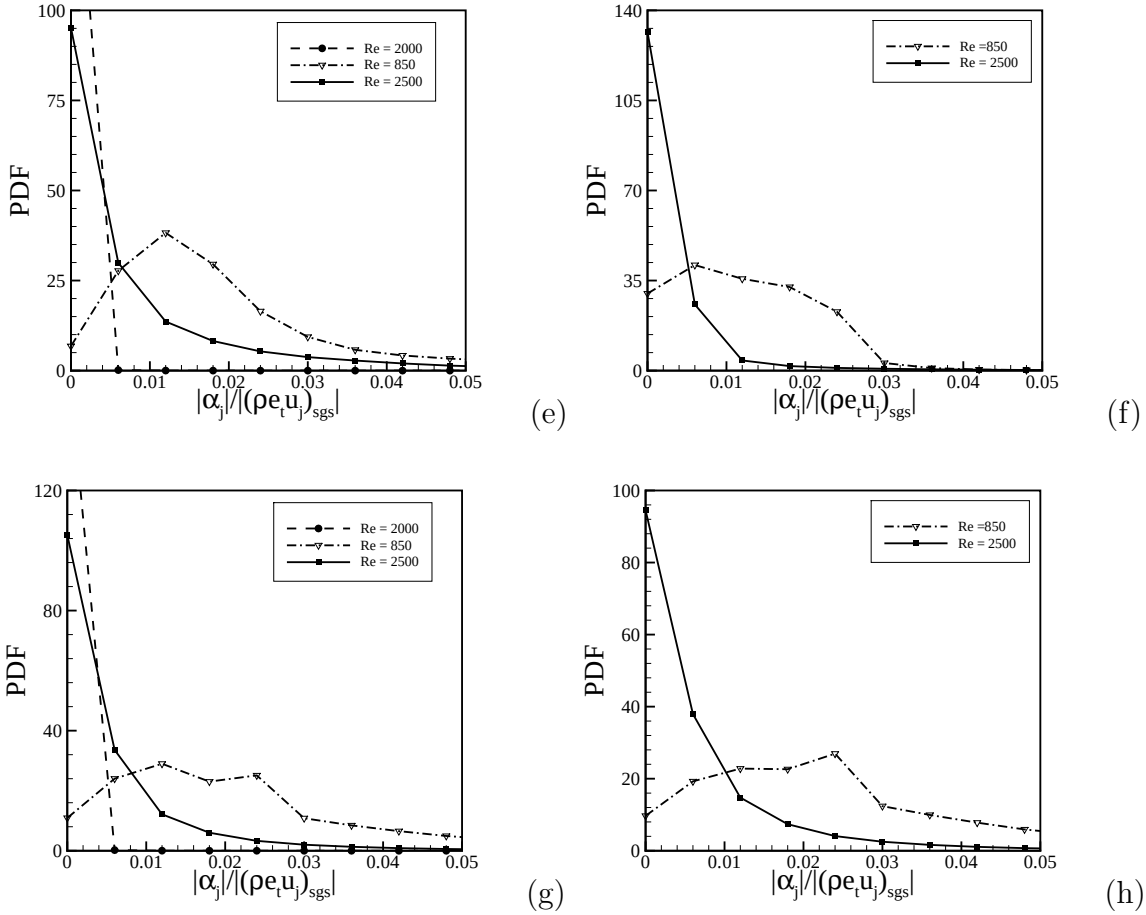

Figure 3.8: PDFs containing the ratios of $|\alpha_j|/|(\rho e_t u_j)_{sgs}|$, where $|\alpha_j| = |\overline{Q_j(\Psi)}|$, in regions described by: (a) $0.01 \leq \phi \leq 0.99$, (b) $0.1 \leq \phi \leq 0.2$, (c) $\langle\langle T''^2\rangle\rangle/E(\langle\langle T''^2\rangle\rangle) \geq 2$, (d) $\langle\langle k_{sgs}\rangle\rangle/E(\langle\langle k_{sgs}\rangle\rangle) \geq 2$, (e) $\langle\langle \phi''^2\rangle\rangle/E(\langle\langle \phi''^2\rangle\rangle) \geq 2$, (f) $\overset{\bullet}{\omega}{}^{OH}/E(\overset{\bullet}{\omega}{}^{OH} \geq 2)$, (g) $\overline{\chi^\phi}/E(\overline{\chi^\phi}) \geq 2$ and (h) $T/T_0 \geq 2$.

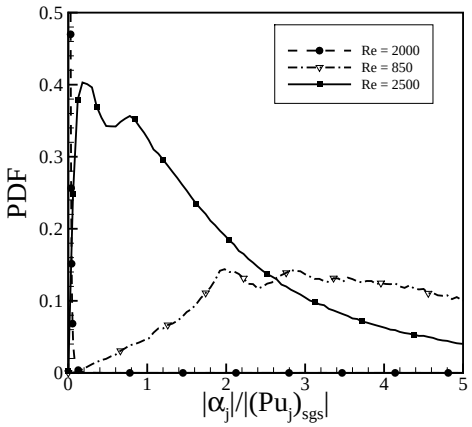
Re = 2000
Re = 850
Re = 2500
PDF
$|\alpha_j|/|(Pu_j)_{sgs}|$

(a)

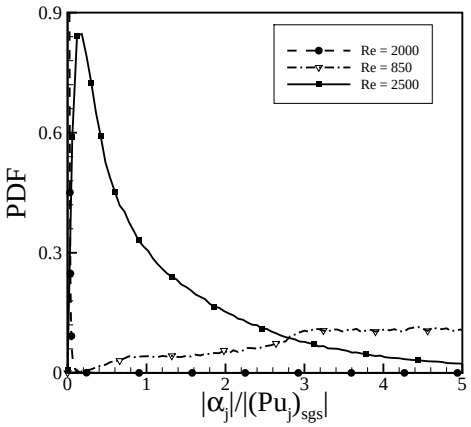
Re = 2000
Re = 850
Re = 2500
PDF
$|\alpha_j|/|(Pu_j)_{sgs}|$

(b)

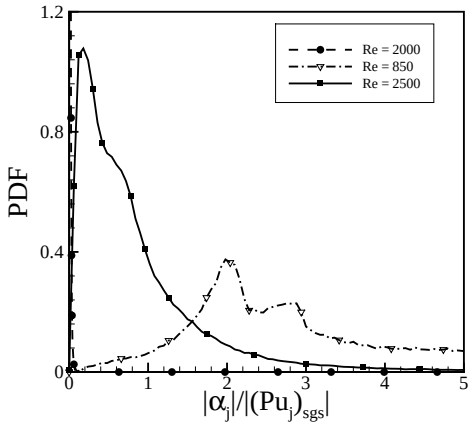
Re = 2000
Re = 850
Re = 2500
PDF
$|\alpha_j|/|(Pu_j)_{sgs}|$

(c)

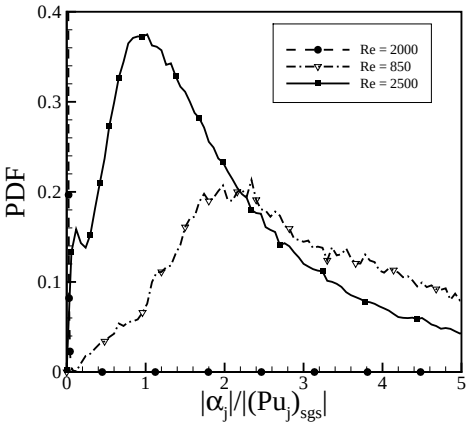
Re = 2000
Re = 850
Re = 2500
PDF
$|\alpha_j|/|(Pu_j)_{sgs}|$

(d)

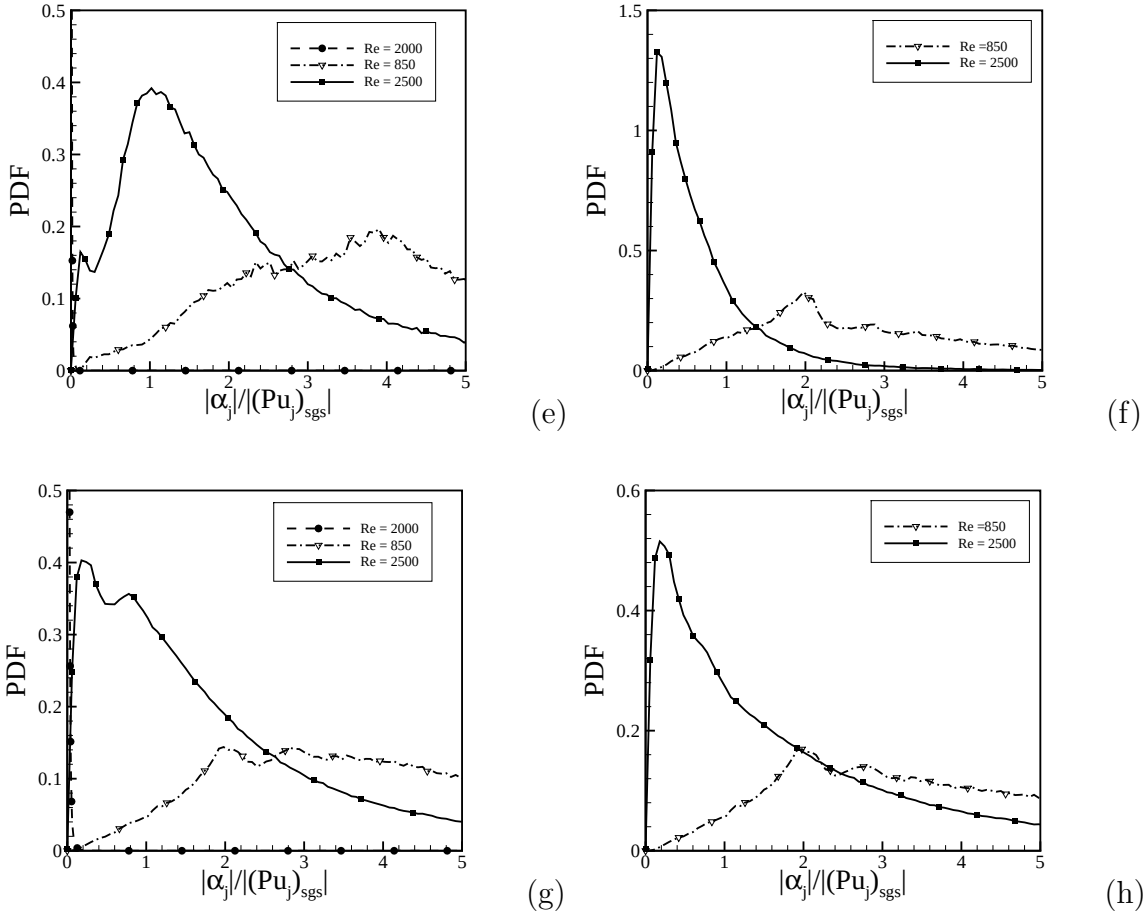

Figure 3.9: PDFs containing the ratios of $|\alpha_j|/|(Pu_j)_{sgs}|$, where $|\alpha_j| = |\overline{Q_j(\Psi)}|$, in regions described by: (a) $0.01 \leq \phi \leq 0.99$, (b) $0.1 \leq \phi \leq 0.2$, (c) $\langle\langle T''^2\rangle\rangle/E(\langle\langle T''^2\rangle\rangle) \geq 2$, (d) $\langle\langle k_{sgs}\rangle\rangle/E(\langle\langle k_{sgs}\rangle\rangle) \geq 2$, (e) $\langle\langle \phi''^2\rangle\rangle/E(\langle\langle \phi''^2\rangle\rangle) \geq 2$, (f) $\overset{\bullet}{\omega}{}^{OH}/E(\overset{\bullet}{\omega}{}^{OH} \geq 2)$, (g) $\overline{\chi^\phi}/E(\overline{\chi^\phi}) \geq 2$ and (h) $T/T_0 \geq 2$.

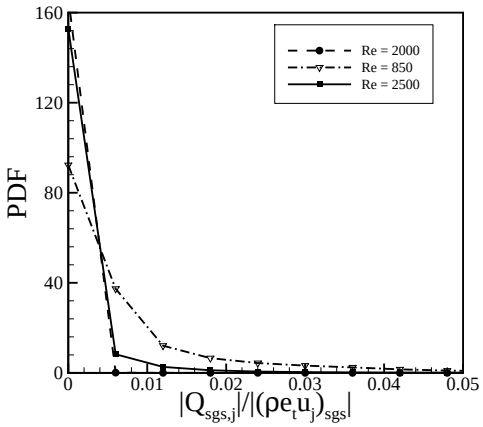
Re = 2000
Re = 850
Re = 2500
PDF
$|Q_{sgs,j}|/|(\rho e_t u_j)_{sgs}|$

(a)

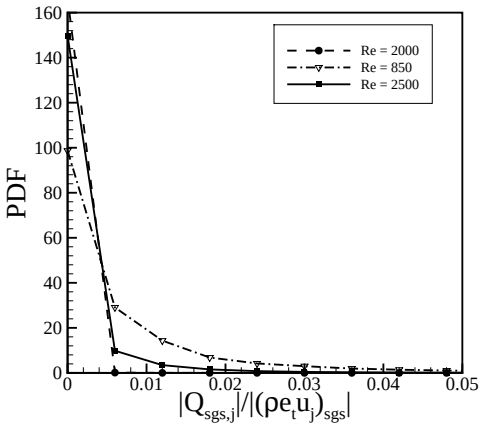
Re = 2000
Re = 850
Re = 2500
PDF
$|Q_{sgs,j}|/|(\rho e_t u_j)_{sgs}|$

(b)

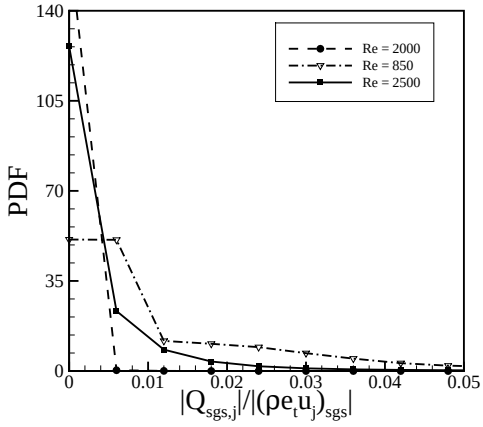
Re = 2000
Re = 850
Re = 2500
PDF
$|Q_{sgs,j}|/|(\rho e_t u_j)_{sgs}|$

(c)

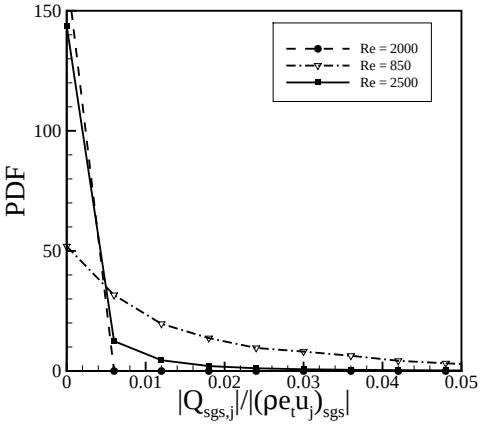
Re = 2000
Re = 850
Re = 2500
PDF
$|Q_{sgs,j}|/|(\rho e_t u_j)_{sgs}|$

(d)

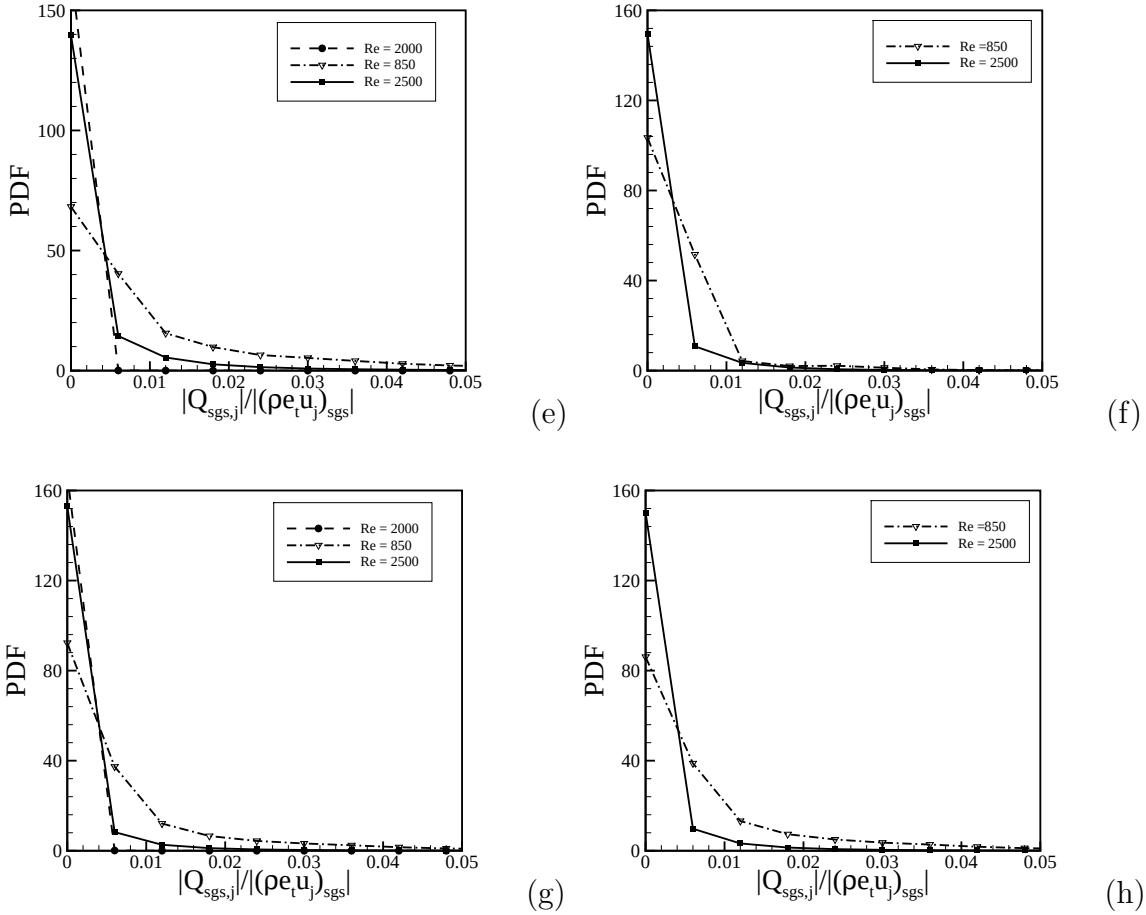

Figure 3.10: PDFs containing the ratios of $|Q_{sgs_{,j}}|/|(\rho e_t u_j)_{sgs}|$, in regions described by: (a) $0.01 \leq \phi \leq 0.99$, (b) $0.1 \leq \phi \leq 0.2$, (c) $\langle\langle T''^2\rangle\rangle / E(\langle\langle T''^2\rangle\rangle) \geq 2$, (d) $\langle\langle k_{sgs}\rangle\rangle / E(\langle\langle k_{sgs}\rangle\rangle) \geq 2$, (e) $\langle\langle \phi''^2\rangle\rangle / E(\langle\langle \phi''^2\rangle\rangle) \geq 2$, (f) $\overset{\bullet}{\omega}{}^{OH} / E(\overset{\bullet}{\omega}{}^{OH} \geq 2)$, (g) $\overline{\chi^\phi} / E(\overline{\chi^\phi}) \geq 2$ and (h) $T/T_0 \geq 2$.

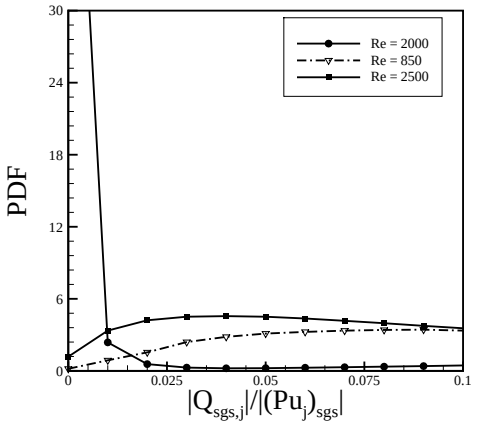
Re = 2000
Re = 850
Re = 2500
PDF
$|Q_{sgs,j}|/|(Pu_j)_{sgs}|$

(a)

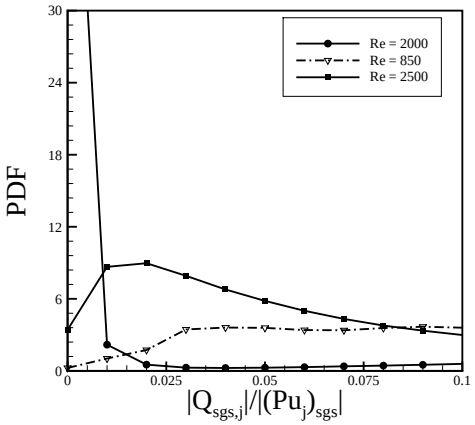
Re = 2000
Re = 850
Re = 2500
PDF
$|Q_{sgs,j}|/|(Pu_j)_{sgs}|$

(b)

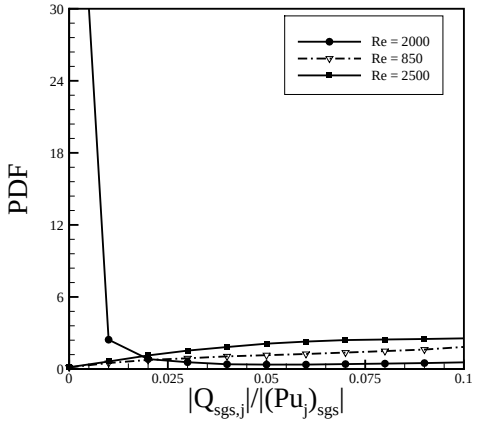
Re = 2000
Re = 850
Re = 2500
PDF
$|Q_{sgs,j}|/|(Pu_j)_{sgs}|$

(c)

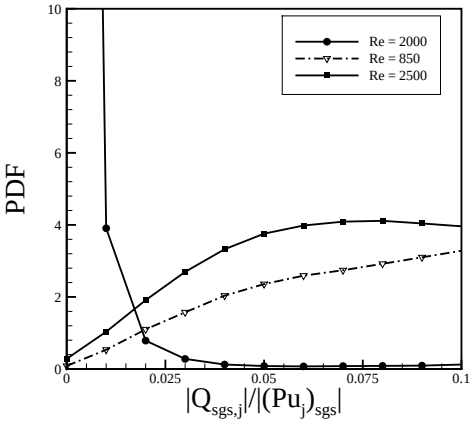
Re = 2000
Re = 850
Re = 2500
PDF
$|Q_{sgs,j}|/|(Pu_j)_{sgs}|$

(d)

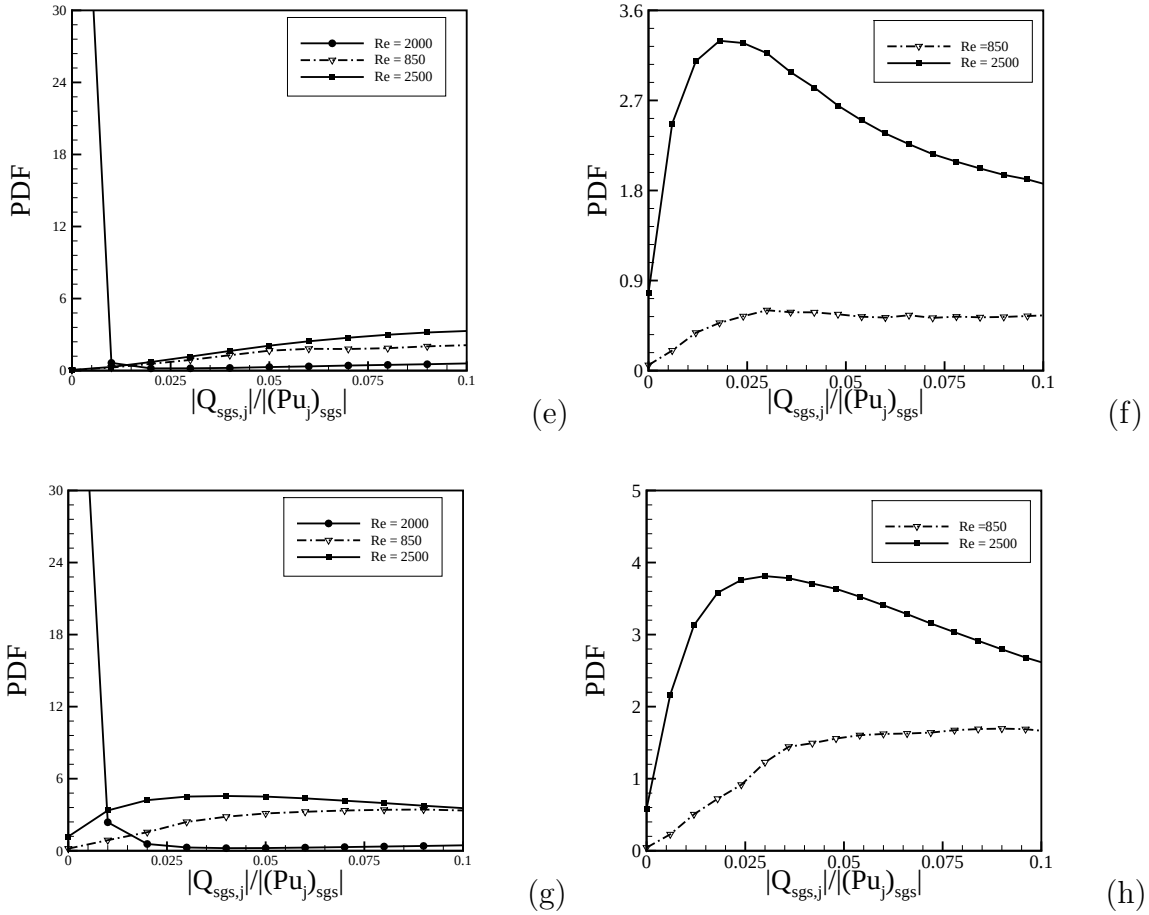

Figure 3.11: PDFs containing the ratios of $|Q_{sgs_{,j}}|/|(Pu_j)_{sgs}|$, in regions described by: (a) $0.01 \leq \phi \leq 0.99$, (b) $0.1 \leq \phi \leq 0.2$, (c) $\langle\langle T''^2\rangle\rangle / E(\langle\langle T''^2\rangle\rangle) \geq 2$, (d) $\langle\langle k_{sgs}\rangle\rangle / E(\langle\langle k_{sgs}\rangle\rangle) \geq 2$, (e) $\langle\langle \phi''^2\rangle\rangle / E(\langle\langle \phi''^2\rangle\rangle) \geq 2$, (f) $\overset{\bullet}{\omega}{}^{OH} / E(\overset{\bullet}{\omega}{}^{OH} \geq 2)$, (g) $\overline{\chi^{\phi}} / E(\overline{\chi^{\phi}}) \geq 2$ and (h) $T/T_0 \geq 2$.

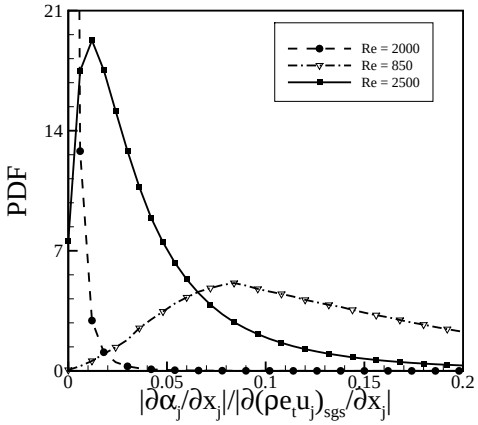
Re = 2000
Re = 850
Re = 2500
PDF
$|\partial\alpha_j/\partial x_j|/|\partial(\rho e_t u_j)_{sgs}/\partial x_j|$

(a)

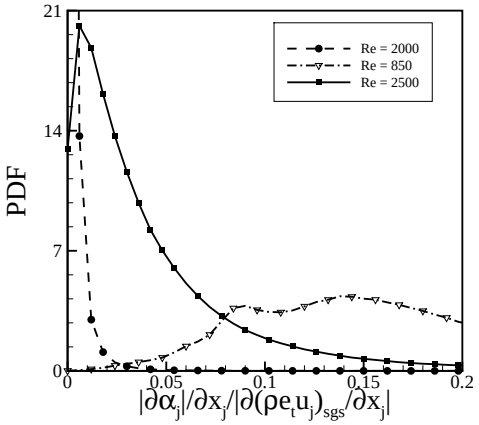
Re = 2000
Re = 850
Re = 2500
PDF
$|\partial\alpha_j/\partial x_j/|\partial(\rho e_t u_j)_{sgs}/\partial x_j|$

(b)

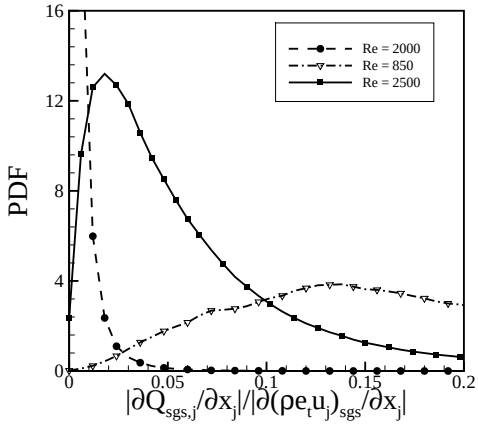
Re = 2000
Re = 850
Re = 2500
PDF
$|\partial Q_{sgs,j}/\partial x_j|/|\partial(\rho e_t u_j)_{sgs}/\partial x_j|$

(c)

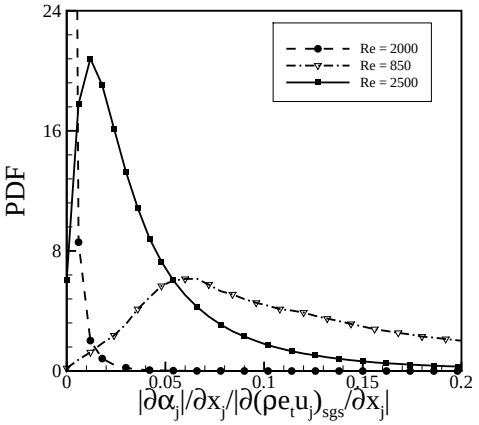
Re = 2000
Re = 850
Re = 2500
PDF
$|\partial\alpha_j|/\partial x_j/|\partial(\rho e_t u_j)_{sgs}/\partial x_j|$

(d)

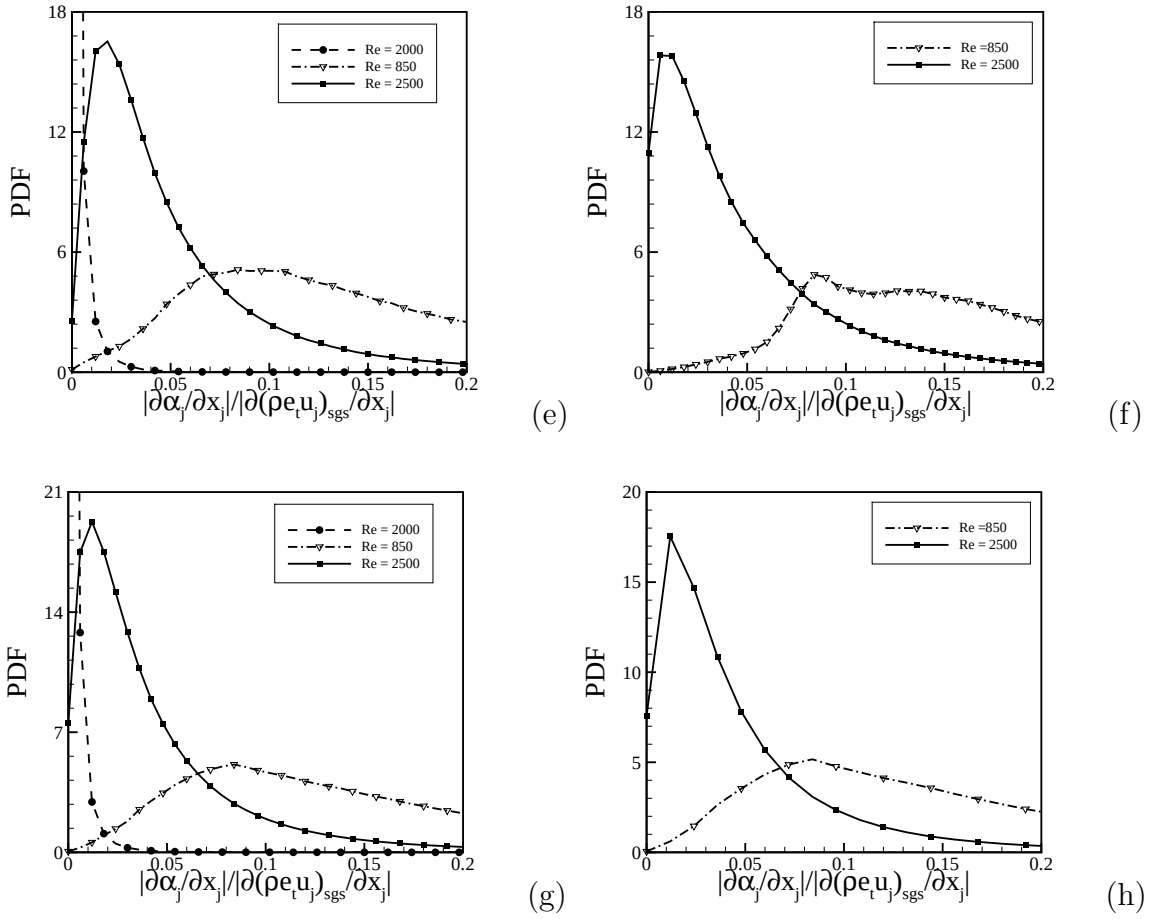

Figure 3.12: PDFs containing the ratios of $|\partial\alpha_j/\partial x_j|/|\partial(\rho e_t u_j)_{sgs}/\partial x_j|$, where $|\alpha_j| = |\overline{Q_j(\Psi)}|$, in regions described by: (a) $0.01 \leq \phi \leq 0.99$, (b) $0.1 \leq \phi \leq 0.2$, (c) $\langle\langle T''^2\rangle\rangle/E(\langle\langle T''^2\rangle\rangle) \geq 2$, (d) $\langle\langle k_{sgs}\rangle\rangle/E(\langle\langle k_{sgs}\rangle\rangle) \geq 2$, (e) $\langle\langle \phi''^2\rangle\rangle/E(\langle\langle \phi''^2\rangle\rangle) \geq 2$, (f) $\overset{\bullet}{\omega}{}^{OH}/E(\overset{\bullet}{\omega}{}^{OH} \geq 2)$, (g) $\overline{\chi^\phi}/E(\overline{\chi^\phi}) \geq 2$ and (h) $T/T_0 \geq 2$.

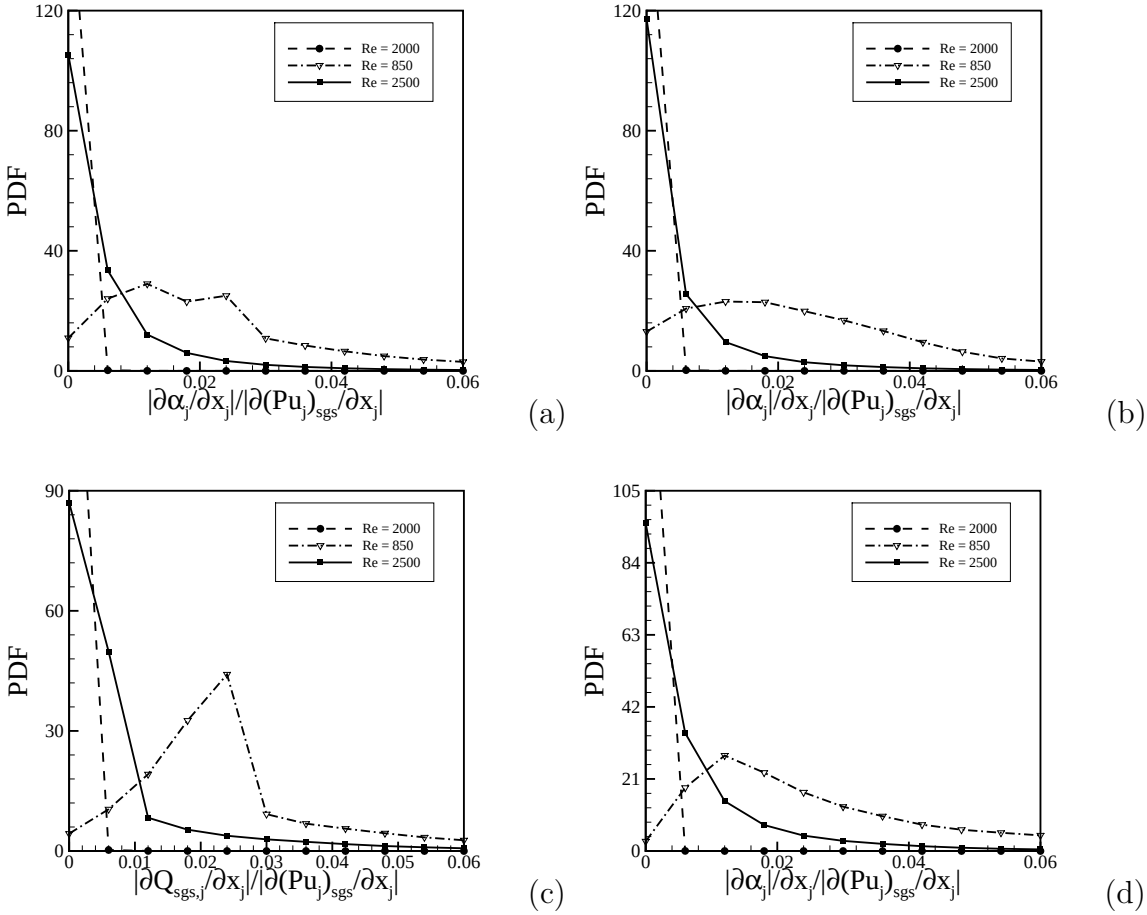
PDF
Re = 2000
Re = 850
Re = 2500
$|\partial\alpha_j/\partial x_j|/|\partial(Pu_j)_{sgs}/\partial x_j|$
(a)
$|\partial\alpha_j|/\partial x_j/|\partial(Pu_j)_{sgs}/\partial x_j|$
(b)
$|\partial Q_{sgs,j}/\partial x_j|/|\partial(Pu_j)_{sgs}/\partial x_j|$
(c)
$|\partial\alpha_j|/\partial x_j/|\partial(Pu_j)_{sgs}/\partial x_j|$
(d)

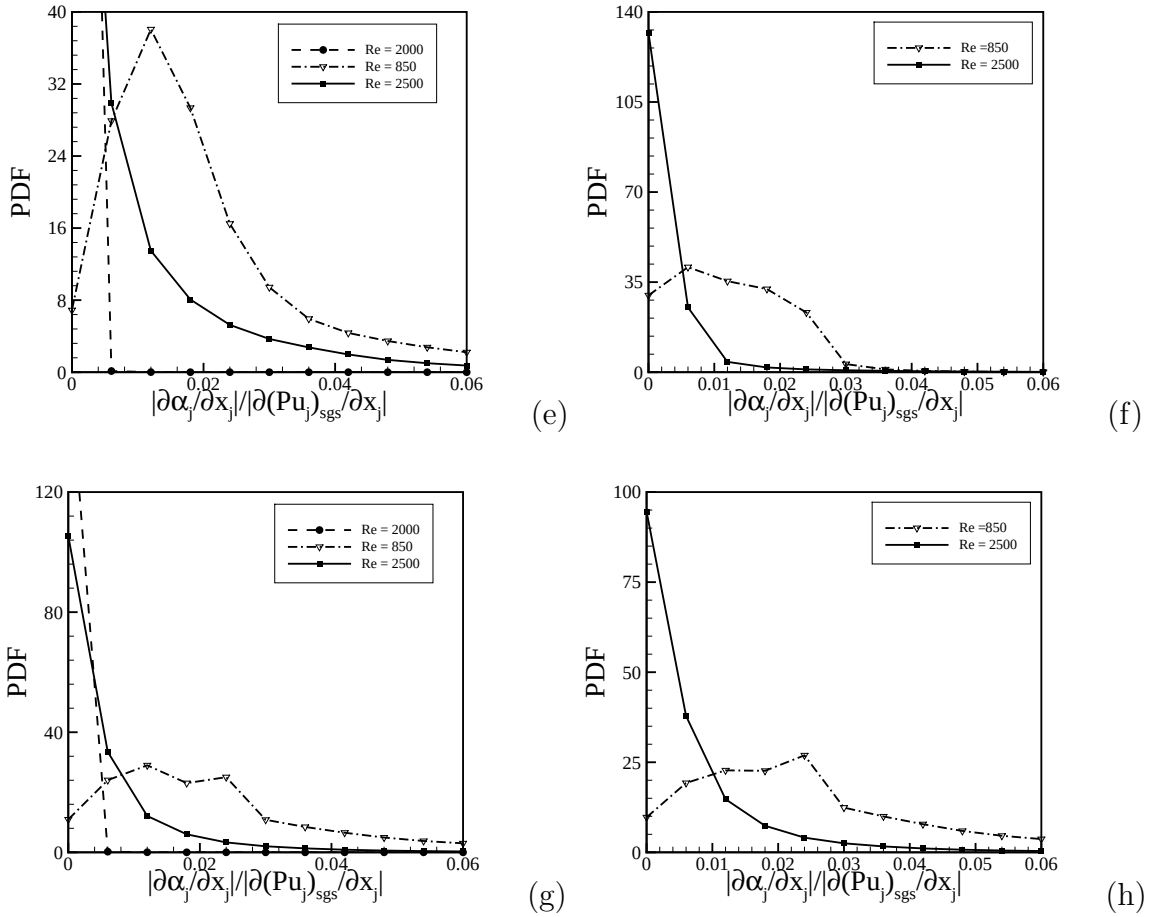

Figure 3.13: PDFs containing the ratios of $|\partial\alpha_j/\partial x_j|/|\partial(Pu_j)_{sgs}/\partial x_j|$, where $|\alpha_j| = |\overline{Q_j(\Psi)}|$, in regions described by: (a) $0.01 \leq \phi \leq 0.99$, (b) $0.1 \leq \phi \leq 0.2$, (c) $\langle\langle T''^2\rangle\rangle/E(\langle\langle T''^2\rangle\rangle) \geq 2$, (d) $\langle\langle k_{sgs}\rangle\rangle/E(\langle\langle k_{sgs}\rangle\rangle) \geq 2$, (e) $\langle\langle \phi''^2\rangle\rangle/E(\langle\langle \phi''^2\rangle\rangle) \geq 2$, (f) $\overset{\bullet}{\omega}{}^{OH}/E(\overset{\bullet}{\omega}{}^{OH} \geq 2)$, (g) $\overline{\chi^\phi}/E(\overline{\chi^\phi}) \geq 2$ and (h) $T/T_0 \geq 2$.

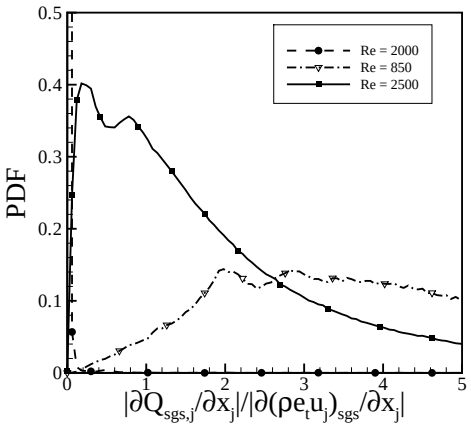
Re = 2000
Re = 850
Re = 2500
PDF
$|\partial Q_{sgs,j}/\partial x_j|/|\partial(\rho e_t u_j)_{sgs}/\partial x_j|$

(a)

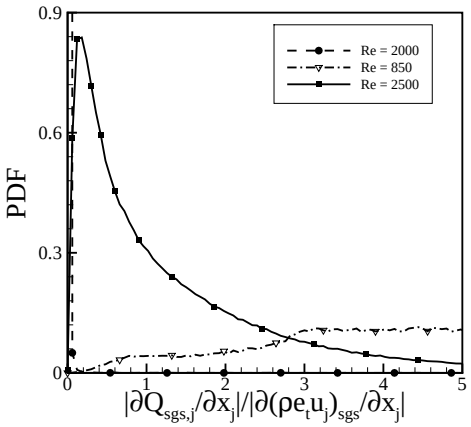
Re = 2000
Re = 850
Re = 2500
PDF
$|\partial Q_{sgs,j}/\partial x_j|/|\partial(\rho e_t u_j)_{sgs}/\partial x_j|$

(b)

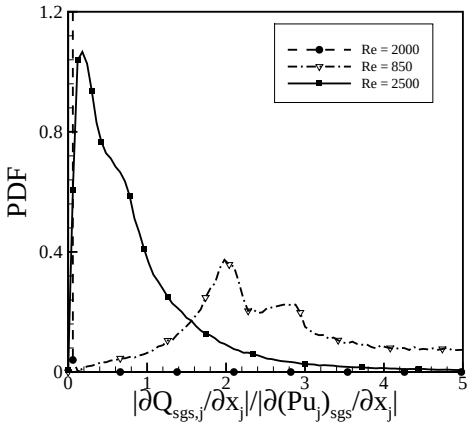
Re = 2000
Re = 850
Re = 2500
PDF
$|\partial Q_{sgs,j}/\partial x_j|/|\partial(Pu_j)_{sgs}/\partial x_j|$

(c)

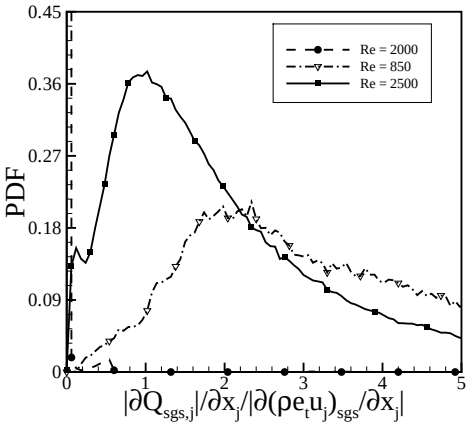
Re = 2000
Re = 850
Re = 2500
PDF
$|\partial Q_{sgs,j}|/\partial x_j/|\partial(\rho e_t u_j)_{sgs}/\partial x_j|$

(d)

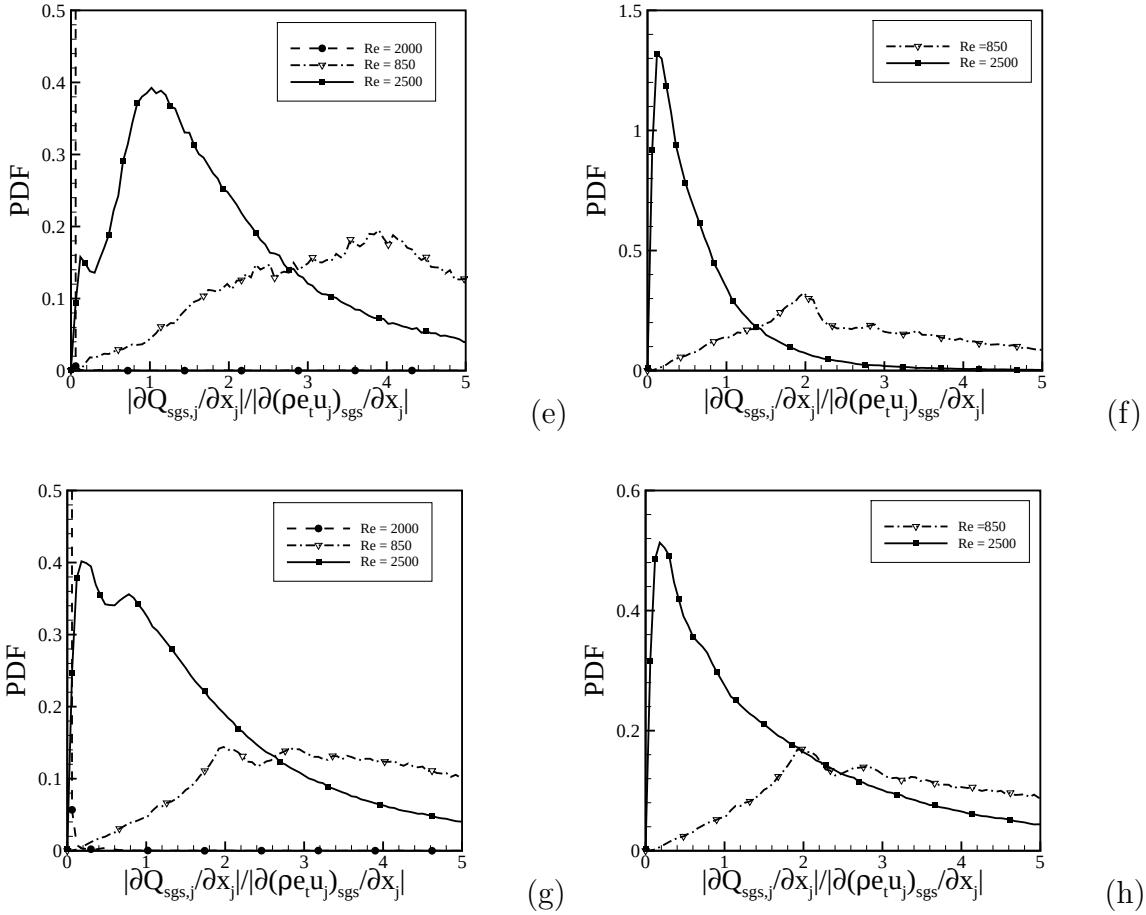

Figure 3.14: PDFs containing the ratios of $|\partial Q_{sgs,j}/\partial x_j|/|\partial(\rho e_t u_j)_{sgs}/\partial x_j|$, in regions described by: (a) $0.01 \leq \phi \leq 0.99$, (b) $0.1 \leq \phi \leq 0.2$, (c) $\langle\langle T''^2\rangle\rangle/E(\langle\langle T''^2\rangle\rangle) \geq 2$, (d) $\langle\langle k_{sgs}\rangle\rangle/E(\langle\langle k_{sgs}\rangle\rangle) \geq 2$, (e) $\langle\langle \phi''^2\rangle\rangle/E(\langle\langle \phi''^2\rangle\rangle) \geq 2$, (f) $\overset{\bullet}{\omega}{}^{OH}/E(\overset{\bullet}{\omega}{}^{OH} \geq 2)$, (g) $\overline{\chi^\phi}/E(\overline{\chi^\phi}) \geq 2$ and (h) $T/T_0 \geq 2$.

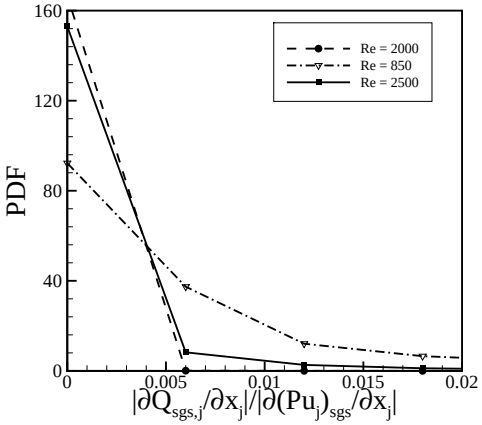
Re = 2000
Re = 850
Re = 2500
PDF
$|\partial Q_{sgs,j}/\partial x_j|/|\partial (Pu_j)_{sgs}/\partial x_j|$

(a)

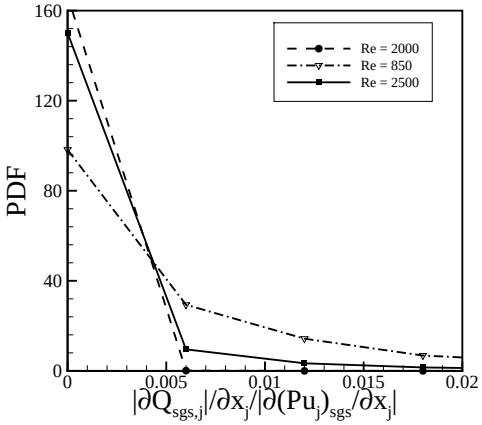
Re = 2000
Re = 850
Re = 2500
PDF
$|\partial Q_{sgs,j}/\partial x_j|/|\partial (Pu_j)_{sgs}/\partial x_j|$

(b)

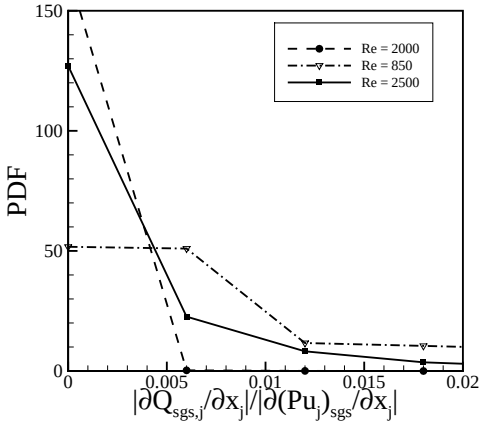
Re = 2000
Re = 850
Re = 2500
PDF
$|\partial Q_{sgs,j}/\partial x_j|/|\partial (Pu_j)_{sgs}/\partial x_j|$

(c)

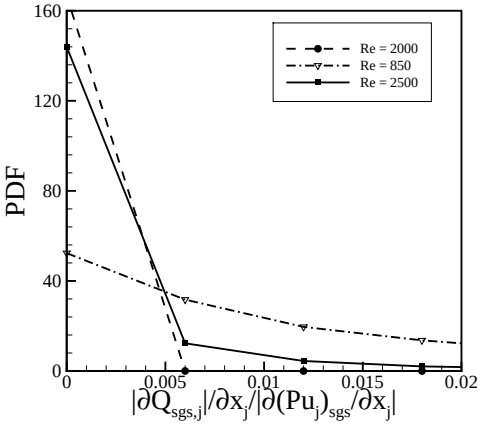
Re = 2000
Re = 850
Re = 2500
PDF
$|\partial Q_{sgs,j}/\partial x_j|/|\partial (Pu_j)_{sgs}/\partial x_j|$

(d)

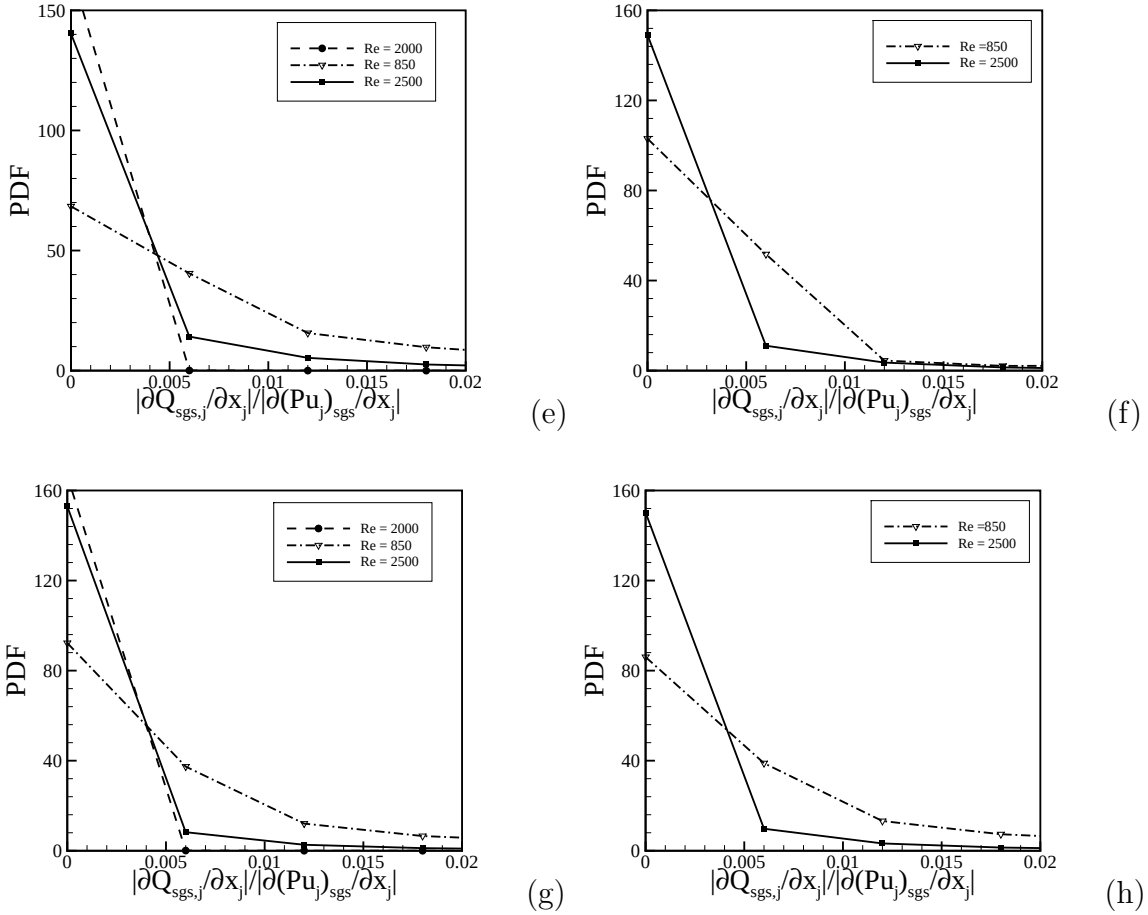

Figure 3.15: PDFs containing the ratios of $|\partial Q_{sgs_{,j}}/\partial x_j|/|\partial (Pu_j)_{sgs}/\partial x_j|$, in regions described by: (a) $0.01 \leq \phi \leq 0.99$, (b) $0.1 \leq \phi \leq 0.2$, (c) $\langle\langle T''^2\rangle\rangle/E(\langle\langle T''^2\rangle\rangle) \geq 2$, (d) $\langle\langle k_{sgs}\rangle\rangle/E(\langle\langle k_{sgs}\rangle\rangle) \geq 2$, (e) $\langle\langle \phi''^2\rangle\rangle/E(\langle\langle \phi''^2\rangle\rangle) \geq 2$, (f) $\overset{\bullet}{\omega}{}^{OH}/E(\overset{\bullet}{\omega}{}^{OH} \geq 2)$, (g) $\overline{\chi^\phi}/E(\overline{\chi^\phi}) \geq 2$ and (h) $T/T_0 \geq 2$.

3.2 Subgrid Heat Flux Vector Modeling

In reacting flows, a substantial heat release occurs where the chemical reaction takes place. Because a large amount of heat production undeniably has substantial effects on turbulent kinetics and flame characteristics, the subgrid heat flux, $Q_{sgs,j}$, may require modeling as concluded in Section 3.1. Modeling the subgrid scale heat flux vector has had little attention in the literature, except for simulations done by Selle *et. al* [39] for supercritical binary mixing layers. Selle *et. al* reported that the gradient of the SGS heat flux vector is significant even for pure mixing, and needs to be modeled. The SGS heat flux vector is the subtraction of the heat flux vector calculated with filtered variables, $Q_j(\overline{\Psi})$, from the actual heat flux vector $\overline{Q_j(\Psi)}$, which is unclosed in an actual LES. LES can only calculate the heat flux vector using filtered primitive variables, $Q_j(\overline{\Psi})$. However, $\overline{Q_j(\Psi)}$ is unknown in LES, but can be calculated exactly in DNS as shown in Section 3.1. In Selle *et. al*'s work only the Irwing-Kirkwood type of heat flux vector was examined. ($Q_{IK_j} = Q_j + \sum_{\alpha=0}^{N} H'_\alpha J'_\alpha$, where J' is the mass flux vector for each species and H' is the molar enthalpy) A model was proposed using multiple Taylor expansion approaches: The authors concluded the work with two statements: 1) the method used may be inappropriate, since poor agreement was found between DNS extracted and model results, and 2) the employed modeling method might be extremely expensive, and a post-priori study should be done. No prior work has examined $Q_{sgs,j}$ directly.

There are two primary approaches to LES modeling. Eddy-viscosity models go all the way back to the poorly correlated Smagorinsky model [40]. The dynamic eddy viscosity model was introduced by Germano *et. al* [9]. The dynamic SGS stress model provides the ability to calculate the eddy viscosity model "constant" locally as a function of position and time. It also has the ability to predict backscatter (i.e.

negative model constant regions). In contrast, the scale similarity model was proposed by Bardina *et. al* [1]. It assumes that the smallest scales of the resolved eddies are statistically similar to the largest scales of the unresolved eddies. The dynamic mixed model is the combination of the two models proposed by Zang *et. al* [51]. The mixed dynamic model retains: 1) the high correlation with the actual SGS stresses of the similarity model, 2) the sufficient diffusivity of the eddy viscosity model needed for numerical stability, and 3) the ability to predict backscatter. However, the model remains computationally intensive.

As a first step in attempting to model the subgrid heat flux vector, this thesis adopts the dynamic/similarity approach. A new model is derived and tested in what follows. The original SGS heat flux is defined as;

$$Q_{j_{,sgs_1}} = \overline{Q_j(\Psi)} - Q_j(\overline{\Psi}). \tag{3.16}$$

A second SGS heat flux is then defined for a larger filter width:

$$Q_{j_{,sgs_2}} = \widetilde{Q_j(\overline{\Psi})} - Q_j(\tilde{\overline{\Psi}}). \tag{3.17}$$

Finally, a third term is defined at even larger width:

$$Q_{j_{,sgs_3}} = \widehat{Q_j(\tilde{\overline{\Psi}})} - Q_j(\hat{\tilde{\overline{\Psi}}}). \tag{3.18}$$

where the over-bar ($\bar{\cdot}$) denotes the original grid level filter, the tilde ($\tilde{\cdot}$) represents the intermediate filter, and finally the carat ($\hat{\cdot}$) stands for the largest filter width. Note that both Q_{j,sgs_2} and Q_{j,sgs_3} can be calculated within an actual LES.

The scale similarity model suggests that all the filtering scales are related to each other by a similarity model constant called C_s, therefore $Q_{j,sgs_2} = C_s Q_{j,sgs_3}$, or:

$$\widetilde{Q_j(\overline{\Psi})} - Q_j(\tilde{\overline{\Psi}}) = C_s[\widehat{Q_j(\tilde{\overline{\Psi}})} - Q_j(\hat{\tilde{\overline{\Psi}}})], \tag{3.19}$$

in which all the terms may be calculated within LES. The model constant, C_s, is considered to be a constant (typically unity) in the original similarity approach. However, when coupled with the dynamic procedure a spatially and temporally varying value is calculated (dynamically) by local flow conditions. No direct model constant is required. As Eq. (3.19) is a vector equation, three values of C_s are possible. Therefore, the single local value of C_s is obtained based on the Least Mean Square Error (LMSE) method. The error, E, is defined as:

$$E = \widetilde{Q_j(\overline{\Psi})} - Q_j(\tilde{\overline{\Psi}}) - C_s[\widehat{Q_j(\tilde{\overline{\Psi}})} - Q_j(\hat{\tilde{\overline{\Psi}}})]. \tag{3.20}$$

The square error is therefore:

$$E^2 = [\widetilde{Q_j(\overline{\Psi})} - Q_j(\tilde{\overline{\Psi}}) - C_s[\widehat{Q_j(\tilde{\overline{\Psi}})} - Q_j(\hat{\tilde{\overline{\Psi}}})]]^2,$$

$$E^2 = (\widetilde{Q_j(\overline{\Psi})} - Q_j(\tilde{\overline{\Psi}}))^2 - 2C_s(\widetilde{Q_j(\overline{\Psi})} - Q_j(\tilde{\overline{\Psi}}))(\widehat{Q_j(\tilde{\overline{\Psi}})} -$$

$$Q_j(\hat{\tilde{\Psi}})) + C_s^2(\widehat{Q_j(\tilde{\Psi})} - Q_j(\hat{\tilde{\Psi}}))^2. \tag{3.21}$$

The LMSE suggests that the square error, E^2, be minimized by nulling its derivative with respect to C_s:

$$\frac{dE^2}{dC_s} = 0,$$

$$-2[\widetilde{Q_j(\Psi)}\widehat{Q_j(\tilde{\Psi})} - \widetilde{Q_j(\Psi)}Q_j(\hat{\tilde{\Psi}}) - Q_j(\tilde{\Psi})\widehat{Q_j(\tilde{\Psi})} + Q_j(\tilde{\Psi})Q_j(\hat{\tilde{\Psi}})]+$$

$$2C_s[\widehat{Q_j(\tilde{\Psi})}^2 - 2\widehat{Q_j(\tilde{\Psi})}Q_j(\hat{\tilde{\Psi}}) + Q_j(\hat{\tilde{\Psi}})]^2 = 0. \tag{3.22}$$

After manipulation the final C_s is:

$$C_s = \frac{[\widehat{Q_j(\tilde{\Psi})}\widetilde{Q_j(\Psi)} - \widehat{Q_j(\tilde{\Psi})}Q_j(\tilde{\Psi}) - Q_j(\hat{\tilde{\Psi}})\widetilde{Q_j(\Psi)} + Q_j(\hat{\tilde{\Psi}})Q_j(\tilde{\Psi})]}{[\widehat{Q_j(\tilde{\Psi})}^2 - 2\widehat{Q_j(\tilde{\Psi})}Q_j(\hat{\tilde{\Psi}}) + Q_j(\hat{\tilde{\Psi}})^2\ ]}, \tag{3.23}$$

where the repeated indices (i.e. j) indicate Einstein summation (reducing C_s to a single constant). Finally the modeled filtered heat flux vector is expressed as:

$$Q_{j_{model}} = Q_j(\Psi) + C_s[\widetilde{Q_j(\Psi)} - Q_j(\widetilde{\Psi})]. \tag{3.24}$$

3.2.1 Model Validation

Figures 3.16 and 3.17 revisit the correlation coefficients for various filter widths and Re_F =850, 2500. Figures 3.16 (a) and (b) present correlation coefficients, $C(|\overline{Q_j(\Psi)}|, |Q_{j,model}|)$, for the reacting case for $Re_F = 850$, for the actual heat flux vector magnitude and the filtered heat flux vector magnitude for various filter widths, $\Delta/\Delta x = 0, 6, 10, 16, 20$. The data are conditioned both globally and on the aforementioned specific flow regions both before modeling and after modeling, respectively. As it is observed in Fig. 3.16 (a) and (b), the dynamic/similarity model enhances the correlation significantly, both globally and locally; especially, for the regions III- $\langle\langle T''^2\rangle\rangle/E(\langle\langle T''^2\rangle\rangle) \geq 2$, IV- $\langle\langle k_{sgs}\rangle\rangle/E(\langle\langle k_{sgs}\rangle\rangle) \geq 2$, V- $\langle\langle \phi''^2\rangle\rangle/E(\langle\langle \phi''^2\rangle\rangle) \geq 2$.

Figures 3.17 (a) and (b) show the corresponding correlation coefficients at $Re_F = 2500$. In Fig. 3.17 (a) the regions, III- $\langle\langle T''^2\rangle\rangle/E(\langle\langle T''^2\rangle\rangle) \geq 2$ and $\dot{\omega}^{OH}/E(\dot{\omega}^{OH} \geq 2)$, which had the poorest correlation before modeling are shown. Figure 3.17 (b) depicts the correlation coefficients after modeling, which are enhanced significantly. The detailed correlation coefficients for different filter widths may be seen in Table 3.6 and 3.9 at Re_F=850 and 2500. Again all of the raw DNS data to calculate the correlation coefficients are shown in the Figs. 3.18 and 3.19.

Table 3.10 provides the correlation coefficients for the divergence of $|\overline{Q_j(\Psi)}|$ and $|Q_j(\overline{\Psi})|$ at Re_F =850 and 2500 for $\Delta/\delta_{\omega 0} \approx 1.92$. The model improves the correlation between the divergence of two terms moderately for $Re_F = 850$, however, there is no such a improvement is observed for higher Re_F flow (i.e. Re_F =2500). The PDFs of the ratios of $|\partial\overline{Q_j(\Psi)}/\partial x_j|$ and $|\partial Q_j(\overline{\Psi})/\partial x_j|$, are depicted by Figs. 3.20 and 3.21.

Again, a tremendous amount of data is continued within the above figures and tables. However, the primary conclusions are that the model does indeed improve

the prediction of the filtered heat flux vector. When considering only the heat flux vector itself (as opposed to its divergence), the model performance increases with increasing Reynolds number but decreases with increasing filter width. Unfortunately, substantial errors remain for all cases; especially when considering the divergence of the heat flux vector. Therefore, future improvements in modeling the SGS heat flux vector are warranted.

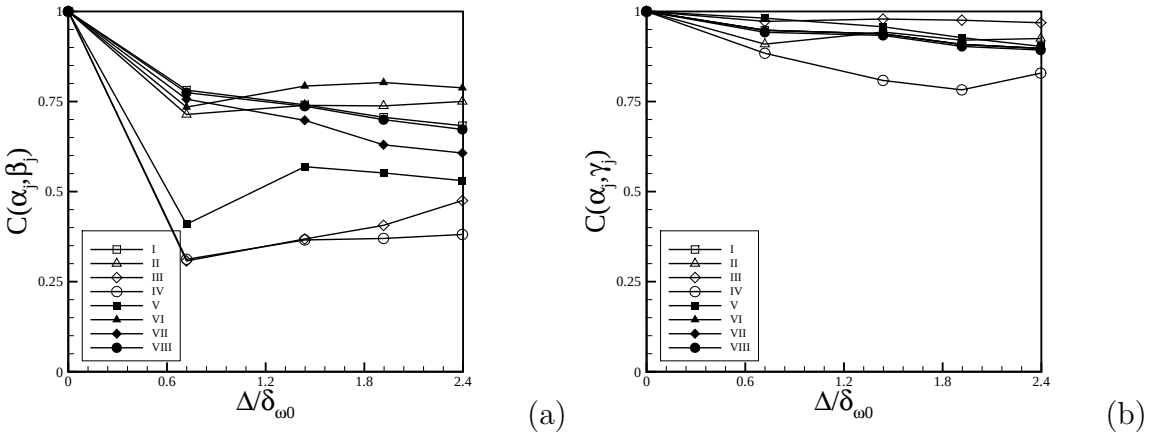

Figure 3.16: Correlation coefficients between the actual heat flux vector magnitude, $|\alpha_j| = |\overline{Q_j(\Psi)}|$, and the heat flux vector magnitude calculated using filtered primitive variables, $|\beta_j| = |Q_j(\overline{\Psi})|$ and the modeled heat flux vector, $|\gamma_j| = |Q_{j_{model}}|$ in regions described by: I- $0.01 \leq \phi \leq 0.99$, II- $0.1 \leq \phi \leq 0.2$, III- $\langle\langle T''^2\rangle\rangle / E(\langle\langle T''^2\rangle\rangle) \geq 2$, IV- $\langle\langle k_{sgs}\rangle\rangle / E(\langle\langle k_{sgs}\rangle\rangle) \geq 2$, V- $\langle\langle \phi''^2\rangle\rangle / E(\langle\langle \phi''^2\rangle\rangle) \geq 2$, VI- $\overset{\bullet}{\omega}^{OH} / E(\overset{\bullet}{\omega}^{OH} \geq 2)$, VII- $\overline{\chi^\phi} / E(\overline{\chi^\phi}) \geq 2$ and VIII- $T/T_0 \geq 2$, (a) No-Model, (b) With Model at $Re_F = 850$.

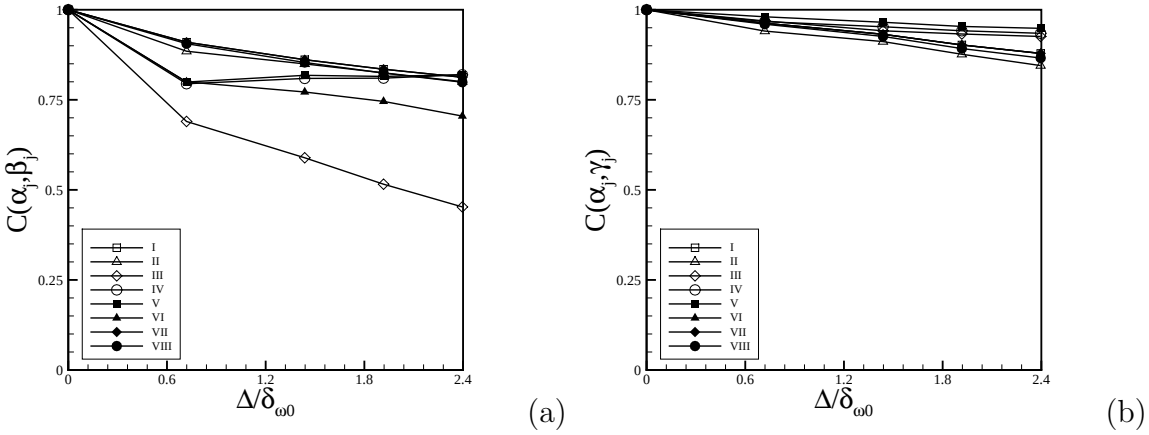

Figure 3.17: Correlation coefficients between the actual heat flux vector magnitude, $|\alpha_j| = |\overline{Q_j(\Psi)}|$, and the heat flux vector magnitude calculated using filtered primitive variables, $|\beta_j| = |Q_j(\overline{\Psi})|$ and the modeled heat flux vector, $|\gamma_j| = |Q_{j_{model}}|$ in regions described by: I- $0.01 \leq \phi \leq 0.99$, II- $0.1 \leq \phi \leq 0.2$, III- $\langle\langle T''^2\rangle\rangle / E(\langle\langle T''^2\rangle\rangle) \geq 2$, IV- $\langle\langle k_{sgs}\rangle\rangle / E(\langle\langle k_{sgs}\rangle\rangle) \geq 2$, V- $\langle\langle \phi''^2\rangle\rangle / E(\langle\langle \phi''^2\rangle\rangle) \geq 2$, VI- $\overset{\bullet}{\omega}^{OH} / E(\overset{\bullet}{\omega}^{OH} \geq 2)$, VII- $\overline{\chi^\phi} / E(\overline{\chi^\phi}) \geq 2$ and VIII- $T/T_0 \geq 2$, (a) No-Model, (b) With Model $Re_F = 2500$.

Regions	Re_F Numbers	
	850	2500
$0.01 \leq \phi \leq 0.99$	0.94	0.96
$0.1 \leq \phi \leq 0.2$	0.90	0.94
$\langle\langle T''^2\rangle\rangle / E(\langle\langle T''^2\rangle\rangle) \geq 2$	0.97	0.97
$\langle\langle k_{sgs}\rangle\rangle / E(\langle\langle k_{sgs}\rangle\rangle) \geq 2$	0.88	0.97
$\langle\langle \phi''^2\rangle\rangle / E(\langle\langle \phi''^2\rangle\rangle) \geq 2$	0.98	0.98
$\overset{\bullet}{\omega}^{OH} / E(\overset{\bullet}{\omega}^{OH} \geq 2)$	0.95	0.96
$\overline{\chi^\phi} / E(\overline{\chi^\phi}) \geq 2$	0.95	0.96
$T/T_0 \geq 2$	0.94	0.96

Table 3.6: Correlation Coefficients after modeling between the actual heat flux vector magnitude $|\overline{Q_j(\Psi)}|$, and the modeled heat flux vector magnitude, $|Q_{j,model}|$ at filter width, $\Delta/\delta_{\omega 0} \approx 0.71$.

Regions	Re_F Numbers	
	850	2500
$0.01 \leq \phi \leq 0.99$	0.94	0.93
$0.1 \leq \phi \leq 0.2$	0.94	0.91
$\langle\langle T''^2\rangle\rangle / E(\langle\langle T''^2\rangle\rangle) \geq 2$	0.98	0.94
$\langle\langle k_{sgs}\rangle\rangle / E(\langle\langle k_{sgs}\rangle\rangle) \geq 2$	0.81	0.95
$\langle\langle \phi''^2\rangle\rangle / E(\langle\langle \phi''^2\rangle\rangle) \geq 2$	0.96	0.96
$\overset{\bullet}{\omega}^{OH} / E(\overset{\bullet}{\omega}^{OH} \geq 2)$	0.94	0.94
$\overline{\chi^{\phi}} / E(\overline{\chi^{\phi}}) \geq 2$	0.94	0.93
$T/T_0 \geq 2$	0.93	0.93

Table 3.7: Correlation Coefficients after modeling between the actual heat flux vector magnitude $|\overline{Q_j(\Psi)}|$, and the modeled heat flux vector magnitude, $|Q_{j,model}|$ at filter width, $\Delta/\delta_{\omega 0} \approx 1.44$.

Regions	Re_F Numbers	
	850	2500
$0.01 \leq \phi \leq 0.99$	0.91	0.90
$0.1 \leq \phi \leq 0.2$	0.92	0.88
$\langle\langle T''^2\rangle\rangle / E(\langle\langle T''^2\rangle\rangle) \geq 2$	0.98	0.93
$\langle\langle k_{sgs}\rangle\rangle / E(\langle\langle k_{sgs}\rangle\rangle) \geq 2$	0.78	0.94
$\langle\langle \phi''^2\rangle\rangle / E(\langle\langle \phi''^2\rangle\rangle) \geq 2$	0.93	0.95
$\overset{\bullet}{\omega}^{OH} / E(\overset{\bullet}{\omega}^{OH} \geq 2)$	0.91	0.90
$\overline{\chi^{\phi}} / E(\overline{\chi^{\phi}}) \geq 2$	0.91	0.90
$T/T_0 \geq 2$	0.90	0.89

Table 3.8: Correlation Coefficients after modeling between the actual heat flux vector magnitude $|\overline{Q_j(\Psi)}|$,and the modeled heat flux vector magnitude, $|Q_{j,model}|$ at filter width, $\Delta/\delta_{\omega 0} \approx 1.92$.

Regions	Re_F Numbers	
	850	2500
$0.01 \leq \phi \leq 0.99$	0.90	0.88
$0.1 \leq \phi \leq 0.2$	0.92	0.85
$\langle\langle T''^2\rangle\rangle / E(\langle\langle T''^2\rangle\rangle) \geq 2$	0.97	0.93
$\langle\langle k_{sgs}\rangle\rangle / E(\langle\langle k_{sgs}\rangle\rangle) \geq 2$	0.83	0.93
$\langle\langle \phi''^2\rangle\rangle / E(\langle\langle \phi''^2\rangle\rangle) \geq 2$	0.90	0.95
$\overset{\bullet}{\omega}^{OH} / E(\overset{\bullet}{\omega}^{OH} \geq 2)$	0.90	0.88
$\overline{\chi^\phi} / E(\overline{\chi^\phi}) \geq 2$	0.90	0.88
$T/T_0 \geq 2$	0.89	0.87

Table 3.9: Correlation Coefficients after modeling between the actual heat flux vector magnitude $|\overline{Q_j(\Psi)}|$, and the modeled heat flux vector magnitude, $|Q_{j,model}|$ at filter width, $\Delta/\delta_{\omega 0} \approx 2.4$.

Regions	Re_F Numbers	
	850	2500
$0.01 \leq \phi \leq 0.99$	0.48	0.47
$0.1 \leq \phi \leq 0.2$	0.45	0.49
$\langle\langle T''^2\rangle\rangle / E(\langle\langle T''^2\rangle\rangle) \geq 2$	0.44	0.55
$\langle\langle k_{sgs}\rangle\rangle / E(\langle\langle k_{sgs}\rangle\rangle) \geq 2$	0.50	0.55
$\langle\langle \phi''^2\rangle\rangle / E(\langle\langle \phi''^2\rangle\rangle) \geq 2$	0.37	0.50
$\overset{\bullet}{\omega}^{OH} / E(\overset{\bullet}{\omega}^{OH} \geq 2)$	0.48	0.40
$\overline{\chi^\phi} / E(\overline{\chi^\phi}) \geq 2$	0.48	0.47
$T/T_0 \geq 2$	0.47	0.45

Table 3.10: Correlation coefficients after modeling between the divergence of modeled heat flux vector magnitude, $|\partial Q_{j,model}/\partial x_j|$, and the divergence of actual heat flux vector magnitude, $|\partial \overline{Q_j(\Psi)}/\partial x_j|$, at filter width, $\Delta/\delta_{\omega 0} \approx 1.92$.

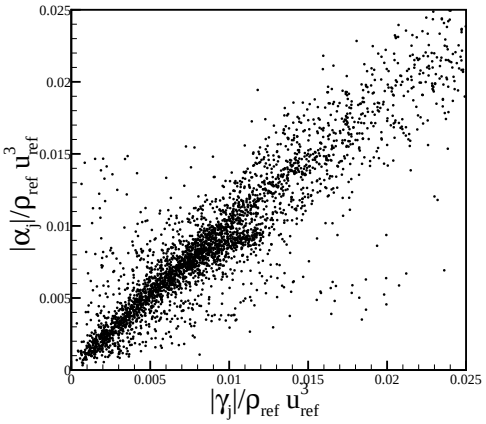
$|\alpha_j|/\rho_{ref}\ u_{ref}^3$
$|\gamma_j|/\rho_{ref}\ u_{ref}^3$
0
0.005
0.01
0.015
0.02
0.025

(a)

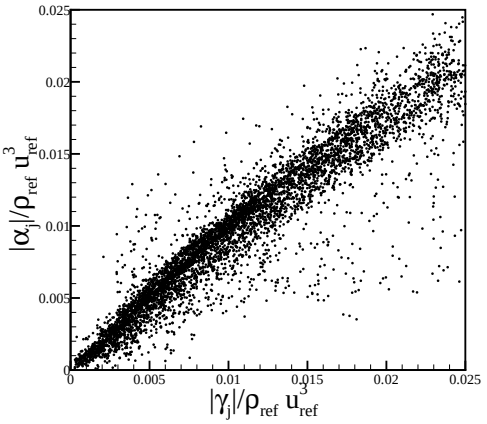
$|\alpha_j|/\rho_{ref}\ u_{ref}^3$
$|\gamma_j|/\rho_{ref}\ u_{ref}^3$
0
0.005
0.01
0.015
0.02
0.025

(b)

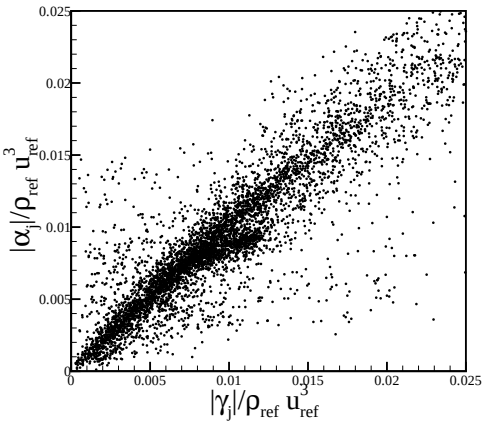
$|\alpha_j|/\rho_{ref}\ u_{ref}^3$
$|\gamma_j|/\rho_{ref}\ u_{ref}^3$
0
0.005
0.01
0.015
0.02
0.025

(c)

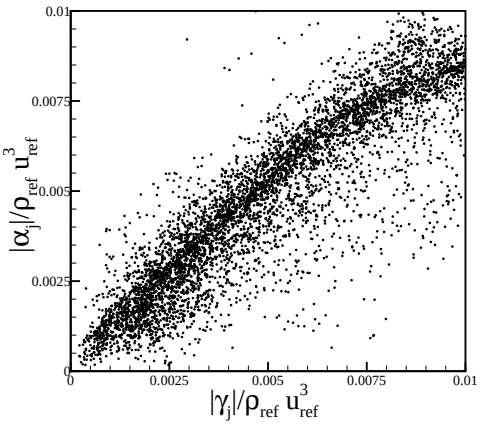
$|\alpha_j|/\rho_{ref}\ u_{ref}^3$
$|\gamma_j|/\rho_{ref}\ u_{ref}^3$
0
0.0025
0.005
0.0075
0.01

(d)

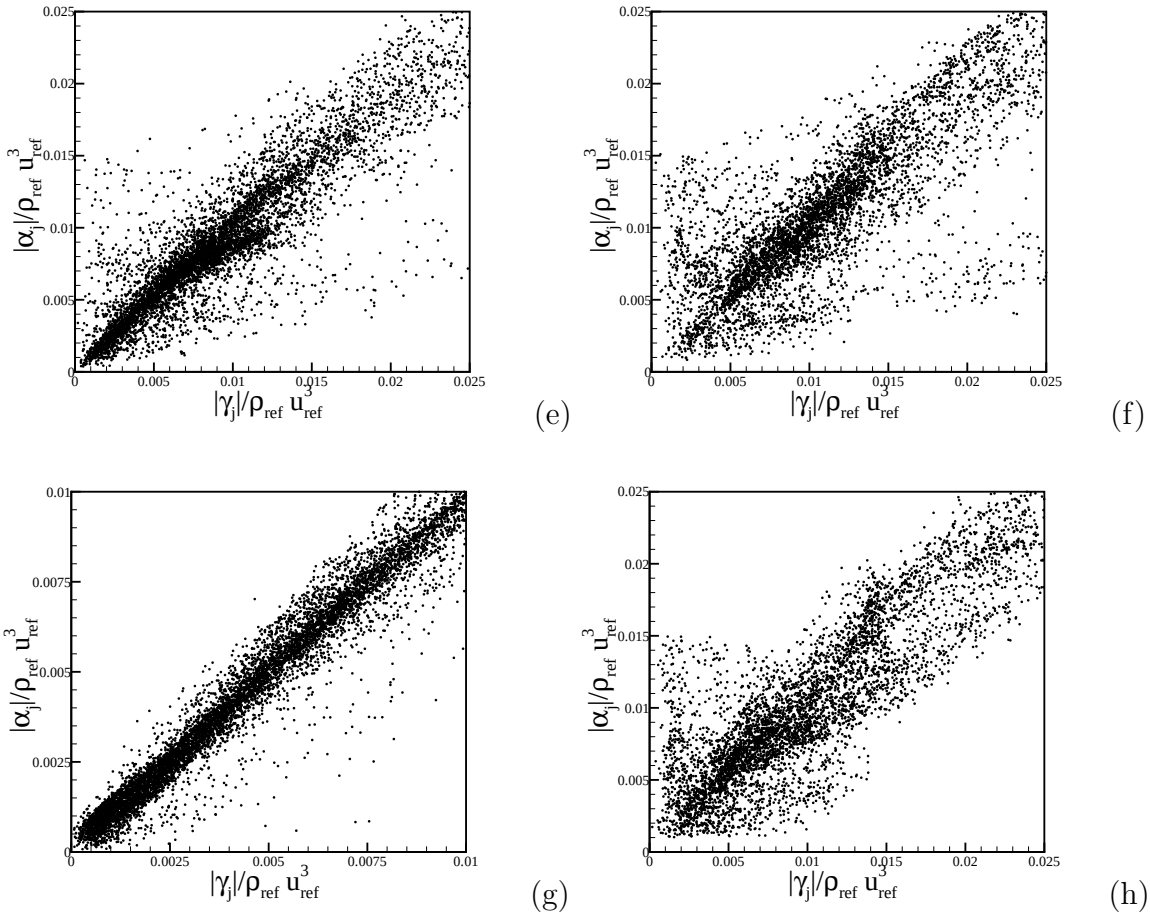

Figure 3.18: Scatter plots of $|\alpha_j|$ vs. $|\gamma_j|$, where $|\alpha_j| = |\overline{Q_j(\Psi)}|$, and $|\gamma_j| = |Q_{j,model}|$, at $Re_F = 850$ in regions described by:(a) $0.01 \leq \phi \leq 0.99$, (b) $0.1 \leq \phi \leq 0.2$, (c) $\langle\langle T''^2\rangle\rangle / E(\langle\langle T''^2\rangle\rangle) \geq 2$, (d) $\langle\langle k_{sgs}\rangle\rangle / E(\langle\langle k_{sgs}\rangle\rangle) \geq 2$ (e) $\langle\langle \phi''^2\rangle\rangle / E(\langle\langle \phi''^2\rangle\rangle) \geq 2$, (f) $\overset{\bullet}{\omega}^{OH} / E(\overset{\bullet}{\omega}^{OH} \geq 2)$, (g) $\overline{\chi^{\phi}} / E(\overline{\chi^{\phi}}) \geq 2$ and (h) $T/T_0 \geq 2$.

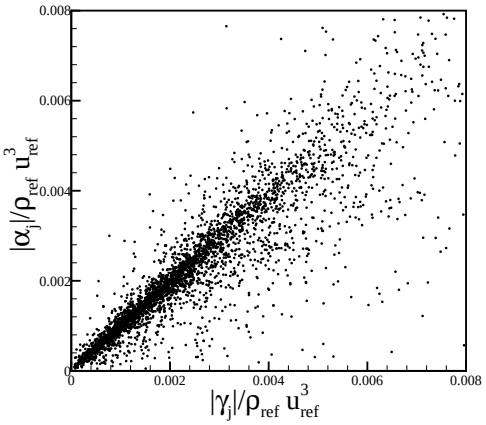
0.008
0.006
0.004
0.002
0
0.002
0.004
0.006
0.008
$|\alpha_j|/\rho_{ref}\, u^3_{ref}$
$|\gamma_j|/\rho_{ref}\, u^3_{ref}$

(a)

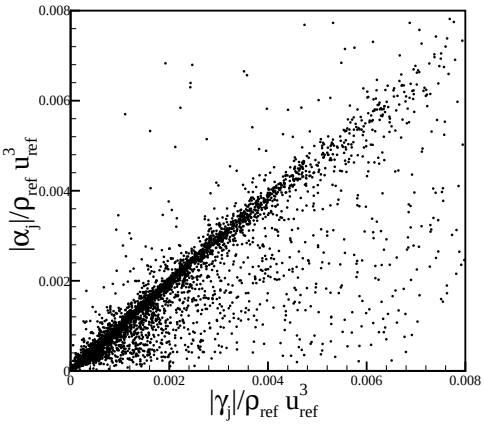
0.008
0.006
0.004
0.002
0
0.002
0.004
0.006
0.008
$|\alpha_j|/\rho_{ref}\, u^3_{ref}$
$|\gamma_j|/\rho_{ref}\, u^3_{ref}$

(b)

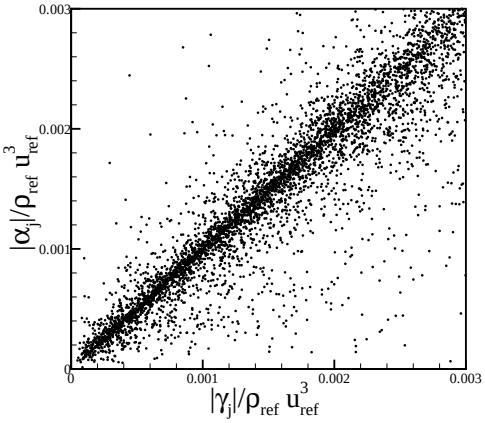
0.003
0.002
0.001
0
0.001
0.002
0.003
$|\alpha_j|/\rho_{ref}\, u^3_{ref}$
$|\gamma_j|/\rho_{ref}\, u^3_{ref}$

(c)

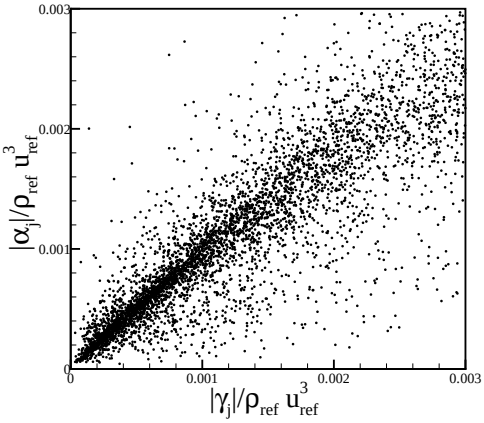
0.003
0.002
0.001
0
0.001
0.002
0.003
$|\alpha_j|/\rho_{ref}\, u^3_{ref}$
$|\gamma_j|/\rho_{ref}\, u^3_{ref}$

(d)

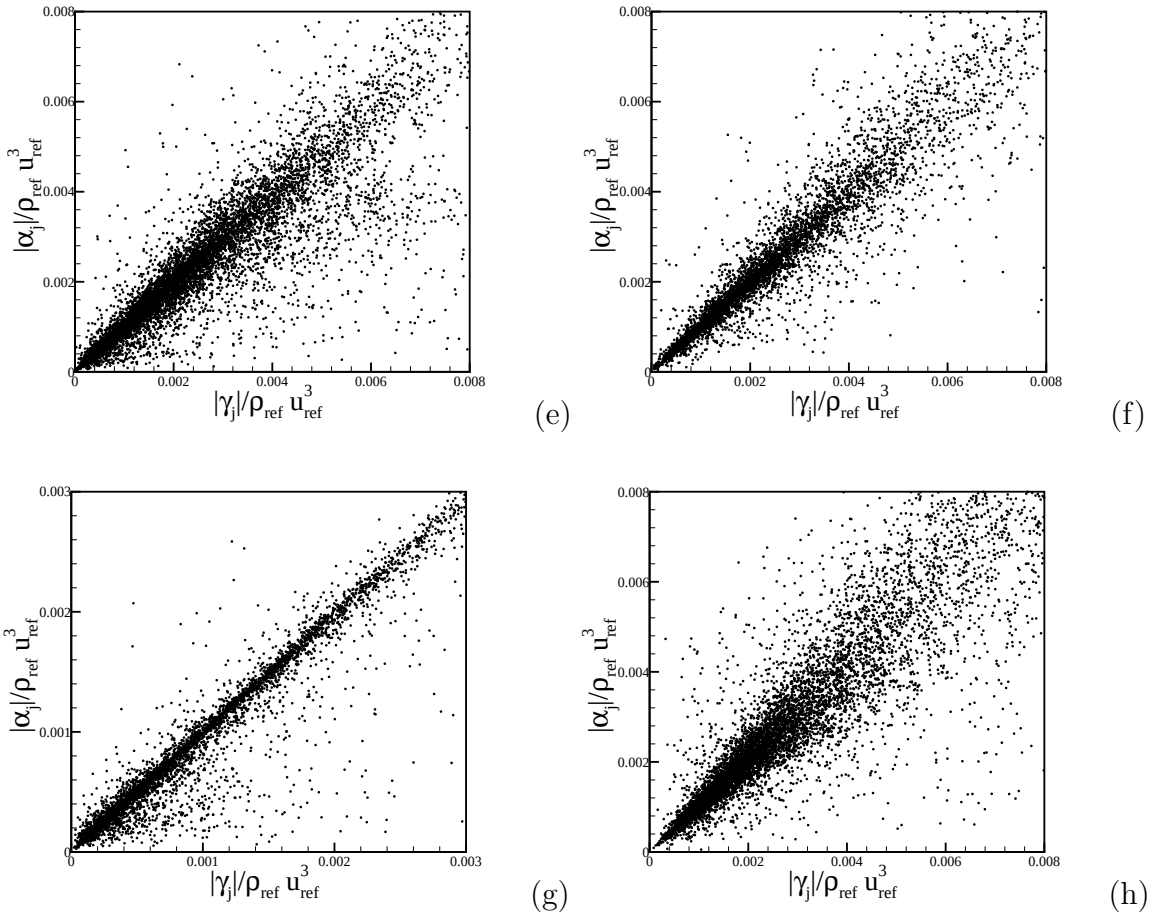

Figure 3.19: Scatter plots of $|\alpha_j|$ vs. $|\gamma_j|$, where $|\alpha_j| = |\overline{Q_j(\Psi)}|$, and $|\gamma_j| = |Q_{j,model}|$, at $Re_F = 2500$ in regions described by: (a) $0.01 \leq \phi \leq 0.99$, (b) $0.1 \leq \phi \leq 0.2$, (c) $\langle\langle T''^2\rangle\rangle / E(\langle\langle T''^2\rangle\rangle) \geq 2$, (d) $\langle\langle k_{sgs}\rangle\rangle / E(\langle\langle k_{sgs}\rangle\rangle) \geq 2$, (e) $\langle\langle \phi''^2\rangle\rangle / E(\langle\langle \phi''^2\rangle\rangle) \geq 2$, (f) $\overset{\bullet}{\omega}{}^{OH} / E(\overset{\bullet}{\omega}{}^{OH} \geq 2)$, (g) $\overline{\chi^\phi} / E(\overline{\chi^\phi}) \geq 2$ and (h) $T/T_0 \geq 2$.

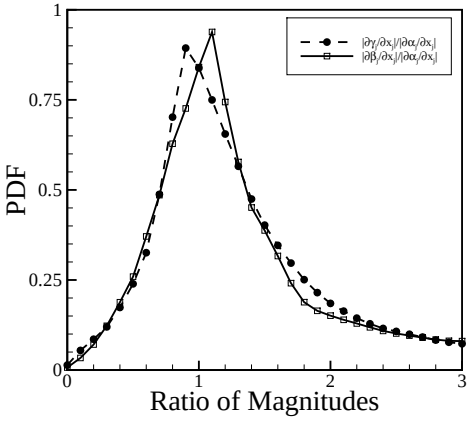
PDF
Ratio of Magnitudes
$|\partial\gamma_j/\partial x_i|/|\partial\alpha_j/\partial x_i|$
$|\partial\beta_j/\partial x_i|/|\partial\alpha_j/\partial x_i|$

(a)

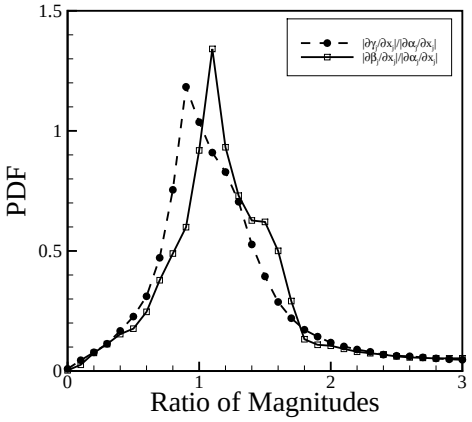
PDF
Ratio of Magnitudes
$|\partial\gamma_j/\partial x_i|/|\partial\alpha_j/\partial x_i|$
$|\partial\beta_j/\partial x_i|/|\partial\alpha_j/\partial x_i|$

(b)

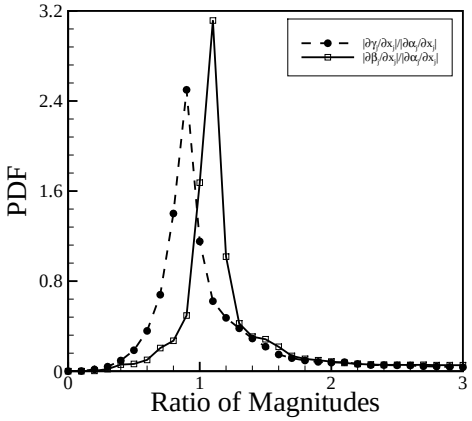
PDF
Ratio of Magnitudes
$|\partial\gamma_j/\partial x_i|/|\partial\alpha_j/\partial x_i|$
$|\partial\beta_j/\partial x_i|/|\partial\alpha_j/\partial x_i|$

(c)

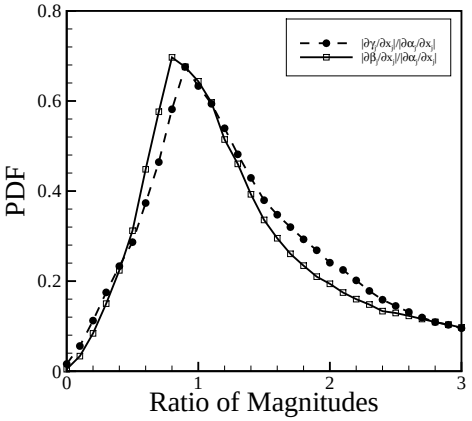
PDF
Ratio of Magnitudes
$|\partial\gamma_j/\partial x_i|/|\partial\alpha_j/\partial x_i|$
$|\partial\beta_j/\partial x_i|/|\partial\alpha_j/\partial x_i|$

(d)

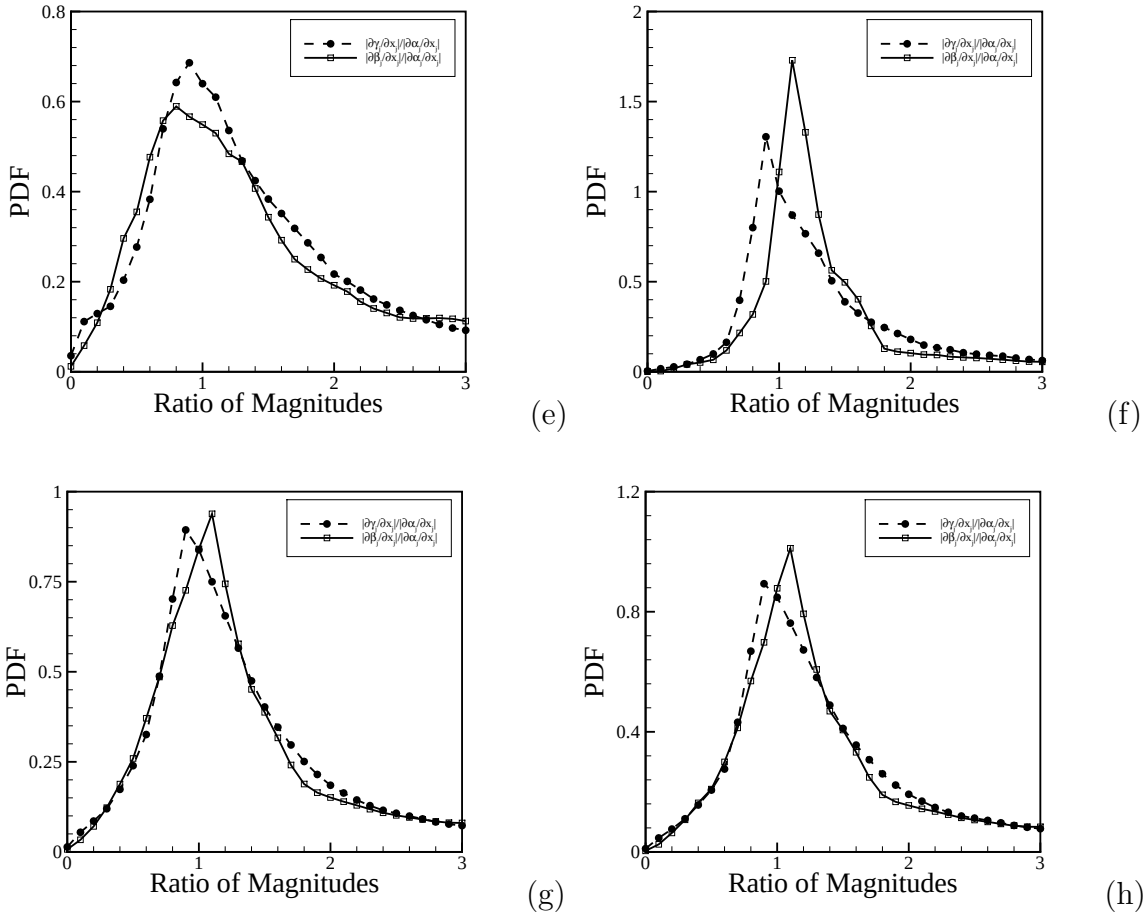

Figure 3.20: PDFs containing the ratios of $|\partial\gamma_j/\partial x_j|/|\partial\alpha_j/\partial x_j|$ and $|\partial\beta_j/\partial x_j|/|\partial\alpha_j/\partial x_j|$= $|\partial Q_j(\overline{\Psi})/\partial x_j|/|\partial\overline{Q_j(\Psi)}/\partial x_j|$, where $|\gamma_j| = |Q_{j,model}|$, $|\beta_j|$= $|Q_j(\overline{\Psi})|$ and $|\alpha_j|$= $|\overline{Q_j(\Psi)}|$ at Re_F =850 in regions described by: (a) $0.01 \leq \phi \leq 0.99$, (b) $0.1 \leq \phi \leq 0.2$, (c) $\langle\langle T''^2\rangle\rangle/E(\langle\langle T''^2\rangle\rangle) \geq 2$, (d) $\langle\langle k_{sgs}\rangle\rangle/E(\langle\langle k_{sgs}\rangle\rangle) \geq 2$, (e) $\langle\langle \phi''^2\rangle\rangle/E(\langle\langle \phi''^2\rangle\rangle) \geq 2$, (f) $\overset{\bullet}{\omega}{}^{OH}/E(\overset{\bullet}{\omega}{}^{OH} \geq 2)$, (g) $\overline{\chi^\phi}/E(\overline{\chi^\phi}) \geq 2$ and (h) $T/T_0 \geq 2$.

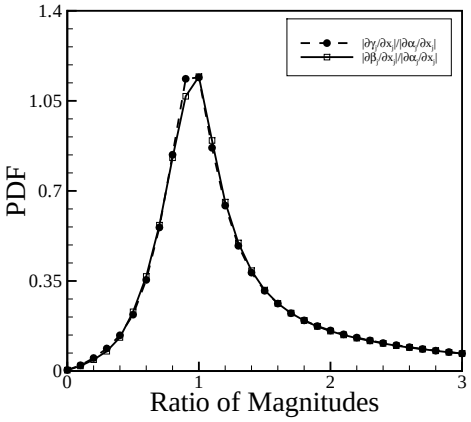
PDF
Ratio of Magnitudes
|∂γ_j/∂x_k|/|∂α_j/∂x_k|
|∂β_j/∂x_k|/|∂α_j/∂x_k|

(a)

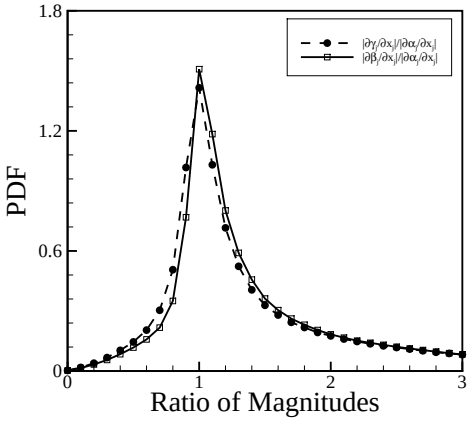
PDF
Ratio of Magnitudes
|∂γ_j/∂x_k|/|∂α_j/∂x_k|
|∂β_j/∂x_k|/|∂α_j/∂x_k|

(b)

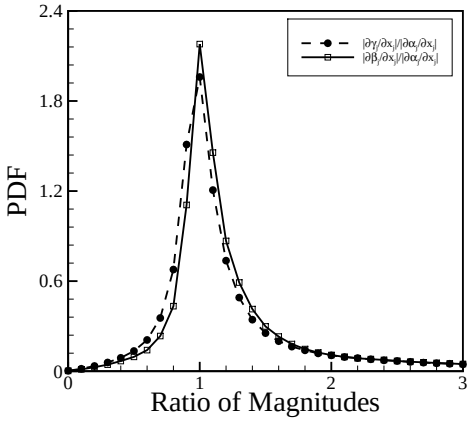
PDF
Ratio of Magnitudes
|∂γ_j/∂x_k|/|∂α_j/∂x_k|
|∂β_j/∂x_k|/|∂α_j/∂x_k|

(c)

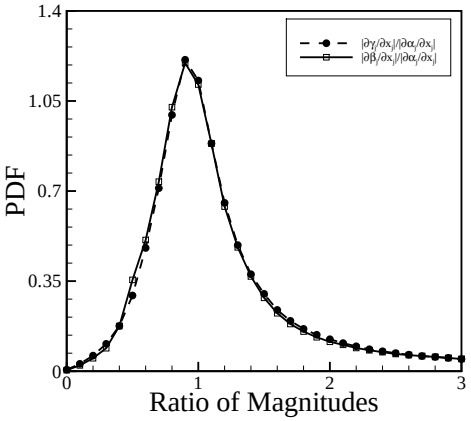
PDF
Ratio of Magnitudes
|∂γ_j/∂x_k|/|∂α_j/∂x_k|
|∂β_j/∂x_k|/|∂α_j/∂x_k|

(d)

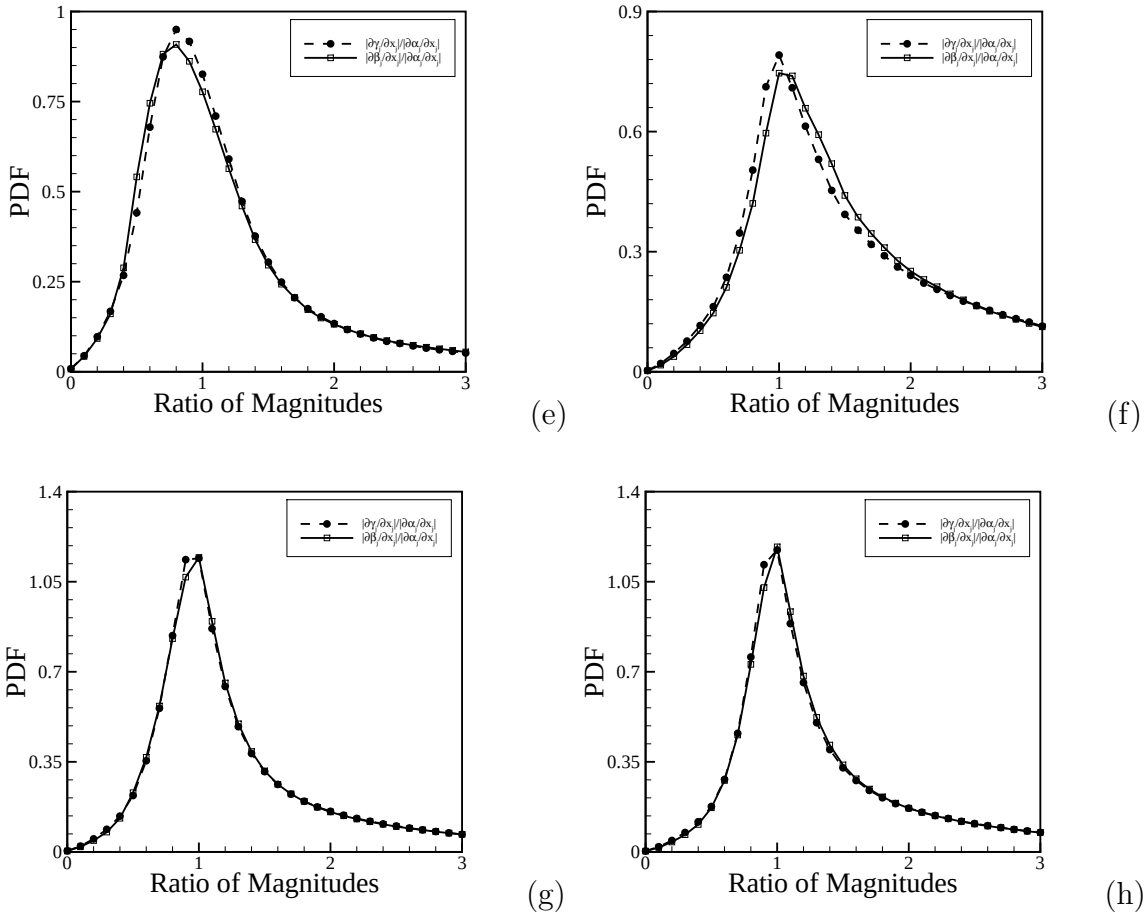

Figure 3.21: PDFs containing the ratios of $|\partial\gamma_j/\partial x_j|/|\partial\alpha_j/\partial x_j|$ and $|\partial\beta_j/\partial x_j|/|\partial\alpha_j/\partial x_j| = |\partial Q_j(\overline{\Psi})/\partial x_j|/|\partial\overline{Q_j(\Psi)}/\partial x_j|$, where $|\gamma_j| = |Q_{j,model}|$, $|\beta_j| = |Q_j(\overline{\Psi})|$ and $|\alpha_j| = |\overline{Q_j(\Psi)}|$ at Re_F =2500, in regions described by: (a) $0.01 \leq \phi \leq 0.99$, (b) $0.1 \leq \phi \leq 0.2$, (c) $\langle\langle T''^2\rangle\rangle/E(\langle\langle T''^2\rangle\rangle) \geq 2$, (d) $\langle\langle k_{sgs}\rangle\rangle/E(\langle\langle k_{sgs}\rangle\rangle) \geq 2$, (e) $\langle\langle \phi''^2\rangle\rangle/E(\langle\langle \phi''^2\rangle\rangle) \geq 2$, (f) $\overset{\bullet}{\omega}{}^{OH}/E(\overset{\bullet}{\omega}{}^{OH} \geq 2)$, (g) $\overline{\chi^\phi}/E(\overline{\chi^\phi}) \geq 2$ and (h) $T/T_0 \geq 2$.

Chapter 4

Conclusions

Direct Numerical Simulations (DNS) of supercritical, H_2/O_2, non-premixed, reacting shear layers containing detailed chemistry, multicomponent, differential, and cross diffusion have been post-processed to analyze the subgrid heat flux vector. The DNS results for the actual heat flux vector magnitude, $|\overline{Q_j(\Psi)}|$, the filtered heat flux vector magnitude, $|Q_j(\overline{\Psi})|$, and the magnitude of the subgrid heat flux vector, $|Q_{j,sgs}|$ have been extensively examined via both correlation coefficients and PDFs of their relative magnitude ratios to other terms in the energy equations. These vectors have also been compared to the subgrid pressure work, $|(Pu_j)_{sgs}|$ and the subgrid convective total energy term, $|(\rho e_t u_j)_{sgs}|$. Divergences of all terms were also analyzed. Both reacting ($Re_F = 850, 2500$) and mixing ($Re_F = 2000$) cases have been considered. The analysis was done both globally and conditioned on specific regions of the flame.

This work reveals the potential necessity of modeling the subgrid heat flux vector in turbulent reacting flows, and derives and tests a model based on the dynamic/similarity method. The subgrid analysis obtained a deep insight into the characteristics of the subgrid heat flux vector. It was shown to be a significant term in

the exact LES energy equation. The derived model was shown to improve the prediction of the SGS heat flux; but still retains excessively large errors. Therefore, future work towards either improving upon the dynamic/similarity approach, or pursuing alternative modeling strategies is warranted.

Bibliography

[1] J. Bardina, J.H. Ferziger, and W.C. Reynolds. Improved subgrid scale models for large eddy simulation. *AIAA Paper 80-1357*, 1980.

[2] D. Carati, S. Ghosal, and P. Moin. On the representation of backscatter in dynamic localization models. *Phys. of Fluids*, 7:606–616, 1995.

[3] T. Cebeci. *Analysis of Turbulent Flows*. Elsevier Science, 2003.

[4] J. Foster. Thermal diffusion coefficient modeling for high pressure combustion simulations. Master's thesis, Clemson University, May 2007.

[5] J. Foster and R.S. Miller. Fundamentals of high pressure combustion. In M Lackner, editor, *High Pressure Processes in Chemical Engineering*, pages 53–75. ProcessEng Engineering GmbH, 2010.

[6] J. Foster and R.S. Miller. A priori analysis of subgrid statistics from direct numerical simulations of high pressure hydrogen-oxygen flames: I subgrid mass flux vector. *7th US National Technical Meeting of the Combustion Institue*, 2011.

[7] J. Frohlich and W. Rodi. Introduction to large eddy simulation of turbulent flows. In B.E. Launder and N.D. Sandham, editors, *Closure Settings for Turbulent and Translational Flows*, pages 267–268. Cambridge University Press, 2000.

[8] E. Garnier, N. Adams, and P. Sagaut. *Large Eddy Simulation for Compressible Flows*. Springer, 2009.

[9] M. Germano, U. Piomelli, P. Moin, and W.H. Cabot. A dynamic subgrid-scale eddy viscosity model. *Phys. of Fluids*, 3:1760–1765, 1991.

[10] S.R. De Groot and P. Mazur. *Non-Equilibrium Thermodynamics*. Dover Publications, New York, New York, 1984.

[11] K. Harstad and J. Bellan. Interactions of fluid oxygen drops in fluid hydrogen at rocket chamber pressures. *Int. J. Heat Mass Transfer*, 41:3551–3558, 1998.

[12] K. Harstad and J. Bellan. Isolated fluid oxygen drop behavior in fluid hydrogen at rocket chamber pressures. *Int. J. Heat Mass Transfer*, 41:3537–3550, 1998.

[13] G.F. Hewitt and J.C. Vassilicos. Intoduction. In G.F. Hewitt and J.C. Vassilicos, editors, *Prediction of Turbulent Flow*, pages 1–5. Cambridge University Press Press, 2005.

[14] K.A. Hoffman and S.T. Chiang. *Computational Fluid Dynamics Volume I.* Engineering Education System, 2004.

[15] F.A. Jaberi and S. James. A dynamic similarity model for large eddy simulation of turbulent combustions. *Phys. Fluids*, 10:1775–1777, 1998.

[16] C.A. Kennedy and M.H. Carpenter. Several new numerical methods for compressible shear-layer simulations. *App. Num. Math*, 14:397–433, 1994.

[17] B. Kosovic. Subgrid-scale modelling for the large-eddy simulation of high-Reynolds-number boundary layers. *J. Fluid Mech.*, 336, 1997.

[18] M. Lesieur and O. Metais. New trends in large-eddy simulations of turbulence. *Annu. Rev. Fluid. Mech*, 28:45–82, 1996.

[19] N. Liu, X. Lu, and L. Zhuang. A dynamic subgrid-scale model for large eddy simulation of stratified flow. *Sci. in China*, 43:391–399, 2000.

[20] Z. Ma. A priori analysis of subgrid-scale pressure in high pressure H_2/O_2. Master's thesis.

[21] Z. Ma, J. Foster, and R.S. Miller. A priori analysis of subgrid statistics from direct numerical simulations of high pressure hydrogen-oxygen flames: III subgrid pressure. *7th US National Technical Meeting of the Combustion Institue*, 2011.

[22] M.P. Martin, U. Piomelli, and G.V. Candler. Subgrid-scale models for compressible large-eddy simulation. *Theo. and Comp. Fluid Dyn.*, 13:361–376, 2000.

[23] C. Meneveau and J. Katz. Scale-invariance and turbulence models for large-eddy simulation. *Annu. Rev. Fluid. Mech*, 32:1–32, 2000.

[24] R.S. Miller, K.G. Harstad, and J. Bellan. Direct numerical simulation of supercritical fluid mixing layers applied to heptane-nitrogen. *J. Fluid Mech.*, 436:1–39, 2001.

[25] K. Mohseni, B. Kosovic, S. Shkoller, and J.E. Marsden. Numerical simulations of the Lagrangian averaged Navier-Stokes equations for homogeneous isotropic turbulence. *Phys. of Fluids*, 15:524–543, 2003.

[26] E.S. Oran and J.P. Boris. *Numerical Simulation of Reactive Flow.* Cambridge University Press, 2001.

[27] S. Palle. *On Real Gas and Molecular Transport Effects in High Pressure Mixing and Combustion.* PhD thesis, Clemson University, 2006.

[28] S. Palle and R.M. Miller. Analysis of high pressure hydrogen, methane, and heptane laminar diffusion flames: Thermal diffusion factor modeling. *J. Appl. Mech.*, 73:5–15, 2006.

[29] S.H. Peng and L. Davidson. On a subgrid-scale heat flux model for large eddy of turbulent thermal flow. *Int. J. of Heat and Mass Trans.*, 45:1393–1405, 2002.

[30] U. Piomelli. Large-eddy and direct simulation of turbulent flows. *Lecture Notes for the 9th Annual Conference of the CFD Society of Canada*, 1997.

[31] U. Piomelli. Large-eddy simulation: Achievements and challenges. *Progress in Aerospace Sciences*, 35:335–362, 1999.

[32] U. Piomelli, H.W. Cabot, P. Moin, and S. Lee. Subgrid-scale backscatter in turbulent and transitional flows. *J. Fluid Mech.*, 3:1766–1771, 1991.

[33] U. Piomelli, P. Moin, and J.H. Ferziger. Model consistency in large eddy simulation of turbulent channel flows. *Phys. of Fluids*, 31:1884–1891, 1988.

[34] H. Pitsch. Large-eddy simulation of turbulent combustion. *Annu. Rev. Fluid Mech.*, 38, 2006.

[35] S.B. Pope. Advances in PDF methods for turbulent reactive flows. *Proceedings of the European Turbulence Conference*, 2004.

[36] S.P. Pope. *Theoretical and Numerical Combustion.* R.T. Edwards Inc., 2001.

[37] R.C. Reid, J.M. Prausnitz, and B.E. Poling. *The Properties of Gases and Liquids.* McGraw Hill, 1987.

[38] P. Sagaut. *Large Eddy Simulation for Incompressible Flows: An Introduction.* Springer, 1998.

[39] L.C. Selle, N.A. Okong'o, J. Bellan, and K.G. Harstad. Modeling of subgrid-scale phenomena in supercritical translational mixing layers: a priori study. *J. Fluid Mech.*, 593:57–91, 2007.

[40] J. Smagorinsky. General circulation experiments with the primitive equation. *Mon. Weather Rev.*

[41] C.H. Sohn and S.H. Chung. Effect of pressure on the extinction, acoustic pressure response, and no formation in diluted hydrogen-air diffusion flames. *Comb. Flame*, 121:288–300, 2000.

[42] R. Vasudevan. Thermal diffusion coefficient modeling for high pressure combustion simulations. Master's thesis, Clemson University, 2007.

[43] R. Vasudevan, J. Foster, and R.S. Miller. Thermal diffusion coefficient modeling at elevated pressure with application to combustion. Combustion and Flame, 2011.

[44] D. Veynante and L. Vervisch. Turbulent combustion modeling. *Prog. Eng. Comb. Sci.*, 28, 2002.

[45] J.F. Vinuesa and F. Porte-Agel. Dynamic models for the subgrid-scale mixing of reactants in atmospheric turbulent reacting flows. *J. of Atm. Sci.*, 65:1692–1699, 2007.

[46] B. Vreman, B. Geurts, and H. Kuerten. Subgrid-modelling in LES of compressible flows. *App. Sci. Research*, 54:191–203, 1995.

[47] B. Vreman, B. Geurts, and H. Kuerten. Large-eddy simulation of the turbulent mixing layer. *J. Fluid Mech.*, 339, 1997.

[48] N.J. Willamson, M.P. Kirkpatrick, S.A. Armfield, and M. Behnia. Sub-filter scale models for scalar transport in large eddy simulations. *16th Australasian Fluid Mec. Conf.*, pages 1427–1431, 2007.

[49] S. Yilmaz. *RANS/PDF and LES/FDF for Prediction of Turbulent Premixed Flames*. PhD thesis, University of Pittsburgh, 2008.

[50] A. Yoshizawa. A statistical theory of thermally-driven turbulent shear flows, with the derivation of a subgrid model. *J. of the Phys. Socie. of Jap*, pages 1194–1205, 1982.

[51] Y. Zang, R.L. Street, and J.R. Koseff. A dynamic mixed subgrid-scale model and its application to turbulent recirculating flows. *Phys. Fluids*, 13:3186–3196, 1993.

[52] W. Zhang and Q. Chen. A new filtered dynamic subgrid-scale model for large eddy simulation of indoor airflow. *Proceeding of the 6th International IBPSA Conference*, pages D–03, 1999.